

UC San Diego

UC San Diego Electronic Theses and Dissertations

Title

Electromagnetic and Multipactor Stresses on RF Windows in Drift Tube Linear Accelerators

Permalink

<https://escholarship.org/uc/item/11s255cz>

Author

Hall, Thomas Wesley

Publication Date

2019

Peer reviewed|Thesis/dissertation

UNIVERSITY OF CALIFORNIA SAN DIEGO

Electromagnetic and Multipactor Stresses on RF Windows in Drift Tube Linear Accelerators

A dissertation submitted in partial satisfaction of the
requirements for the degree

Doctor of Philosophy

in

Engineering Sciences (Engineering Physics)

by

Thomas Wesley Hall

Committee in charge:

Prabhakar Bandaru, Chair
Vitaliy Lomakin
Kevin Quest
Daniel Rees
Kalyanasundaram Seshadri
Daniel Tartakovsky

2019

Copyright

Thomas Wesley Hall, 2019

All rights reserved.

The Dissertation of Thomas Wesley Hall is approved, and it is acceptable in
quality and form for publication on microfilm and electronically:

Chair

University of California San Diego

2019

DEDICATION

To my wife, Kate, and to Rocket, Lorraine, and Simeon

TABLE OF CONTENTS

Signature Page.....	iii
Dedication	iv
Table of Contents	v
List of Abbreviations.....	vii
List of Symbols	viii
List of Figures	x
List of Tables.....	xvi
Acknowledgements	xvii
Vita.....	xviii
Abstract of the Dissertation.....	xix
Chapter 1	Introduction..... 1
1.1	History of particle accelerators 1
1.2	Los Alamos Neutron Science Center 2
1.3	RF windows in DTL power couplers 4
1.3.1	Requirements of RF window 4
1.3.2	History of RF window failures..... 5
1.3.3	Potential failure mechanisms 7
Chapter 2	Electromagnetic Analysis..... 11
2.1	Introduction..... 11
2.2	Power coupler and window without accelerating cavity..... 12
2.2.1	Window stresses..... 13
2.2.2	Window geometry..... 14
2.2.3	Excitation of higher order modes 20
2.3	Effect of accelerating cavity..... 28
2.3.1	Q-factor and simulations..... 28
2.3.2	Quick fill method 30
2.3.3	Analysis of DTL system..... 46
2.3.4	Harmonics and off-resonance conditions..... 55
Chapter 3	Multipactor—Principles and Simulation..... 69
3.1	The multipactor phenomenon..... 69
3.1.1	Emission criterion of multipactor..... 70
3.1.2	Resonance criterion of multipactor 71
3.2	Multipactor in infinite parallel plates 72
3.2.1	Frequency-gap width product..... 73

	3.2.2	Satisfaction of emission criterion.....	74
	3.2.3	Non-ideal factors.....	75
3.3		Multipactor on dielectric surfaces.....	77
3.4		Multipactor in coaxial lines.....	78
	3.4.1	Equations of motion in cylindrical coordinates.....	78
	3.4.2	Normalized gap width and standing waves.....	80
3.5		Simulation of multipactor.....	81
	3.5.1	Solving equations of motion	82
	3.5.2	Initialization of electrons.....	84
	3.5.3	Collision events.....	87
	3.5.4	Analyzing multipactor from trajectories	89
	3.5.5	Non-zero emission velocities	94
3.6		Simulation benchmarks.....	98
	3.6.1	Coaxial lines of varying impedances	98
	3.6.2	Experimental benchmark	101
	3.6.3	Normalized gap width.....	102
	3.6.4	Miscellaneous factors affecting simulations	104
	3.6.5	Signal reflections and standing waves	107
Chapter 4		Multipactor near the RF window	112
	4.1	Outline of RF window multipactor analysis	112
	4.2	Generic RF windows.....	113
	4.2.1	Window collisions as compared against CST	114
	4.2.2	Calculated metrics.....	117
	4.3	DTL RF windows.....	123
	4.3.1	Traveling waves	123
	4.3.2	Standing waves.....	126
	4.3.3	Effect of emission properties.....	134
	4.3.4	Higher order modes and harmonics	139
	4.3.5	Charge accumulation on window.....	142
Chapter 5		Summary and Conclusions.....	151
References		159

LIST OF ABBREVIATIONS

DC	Direct current
DTL	Drift-tube linear accelerator
EM	Electromagnetic
EMP	Electric field maximum multipactor
HOM	Higher order mode
I/O	Input/output
LANSCE	Los Alamos Neutron Science Center
MMP	Magnetic field maximum multipactor
MP	Multipactor
PEC	Perfect electrical conductor
RF	Radio frequency
TE	Transverse electric field modes
TEM	Transverse Electromagnetic
TM	Transverse magnetic field modes
TTF	Tesla Test Facility

LIST OF SYMBOLS

\mathbf{A}	Vector potential
A	Generic sinusoidal amplitude
\mathbf{B}	Magnetic field vector
c_0	Speed of light in free space
\mathbf{E}	Electric field vector
E_0	Baseline electric field amplitude
g	Growth factor of multipactor
G	Green's functions
i	Index for quick fill sections or electron trajectory time steps
\mathbf{J}	Current density vector
j	Imaginary unit equal to $\sqrt{-1}$
J_m	Bessel function of the first kind
k	Wavenumber, sometimes subscripted by component
m_e	Electron mass
P	Power
p	Number of electrons in population
q_e	Electron charge
Q_m	Quality factor of resonating structure for mode m
r_i	Coaxial line inner conductor
r_o	Coaxial line outer conductor
V	Voltage
v, \mathbf{v}	Electron speed or velocity, optionally in vector form
Y_m	Bessel function of the second kind

Z_0	Characteristic impedance
γ	Frequency of particular solution of cavity response, or the Lorentz factor
δ	Secondary electron emission yield, or delta function
ϵ_0	Electric permittivity of free space
ϵ_r	Relative electric permittivity
ζ	Normalized frequency-gap width product
λ	Wave length
μ_0	Magnetic permeability of free space
ξ_m	Magnitude of vector potential for mode m (Cavity response)
χ_e and ν_e	Amplitude and phase of the signal emitted by the accelerator cavity
χ_{eff} and ν_{eff}	Total effective amplitude and phase of either the backward propagating signal or the standing wave signal
χ_r and ν_r	Amplitude and phase of the signal reflected at the transmission line terminus
ψ	Generic sinusoidal phase
ω	Angular frequency

LIST OF FIGURES

Figure 1.1:	Illustration of RF window in coaxial line. The window is clearly secured by the interlocking of conductor and window geometries	4
Figure 2.1:	Window geometries used to investigate the EM fields in the coupler. The inner conductor is on the left side of the image, and the outer conductor is to the right. The top portion has one notch on the air side, and the bottom portion has two air-side notches.	16
Figure 2.2:	Electric (top) and magnetic (bottom) fields for the DTL window as is. The electric field has apparent changes to its axial component near the window.....	17
Figure 2.3:	Voltages resulting from various notch geometries. (a) shows the voltages across the air surface of the window, and (b) shows the voltage across the vacuum surface of the window. The parameter sets used in (a) are in sorted first by $hA1$, then by $hA2$, then by hd	19
Figure 2.4:	Cut-off frequencies of higher order modes in DTL.....	21
Figure 2.5:	Electric field of the radial (E_r) and axial (E_z) components. The fields were calculated in CST and compared to the fields calculated from the superposition of the TM_{01} and TM_{02} amplitudes given in Table 2.1. The fit of all TM_{0n} modes from $0 \leq n \leq 100$	26
Figure 2.6:	Example of the signal used to quickly fill the cavity, reproduced courtesy of The Electromagnetics Academy.....	31
Figure 2.7:	Sample S-parameter calculated by CST. Due to errors in using a finite series, the values surrounding the resonance frequency will be greater than one (zero in dB), so the value $\Delta\omega_m$ is based at the midpoint between the maximum and minimum values immediately surrounding the resonance frequency.....	34
Figure 2.8:	Geometries of the sample cavities used to establish the quick fill method. (a) contains no drift tubes but can have PEC or copper cavity walls, and (b) has four drift tubes added with only PEC used for the cavity, reproduced courtesy of The Electromagnetics Academy.....	36
Figure 2.9:	S-parameters for the truncated cavities made of PEC and copper. Various cavity modes are labeled at their frequency, reproduced courtesy of The Electromagnetics Academy	39
Figure 2.10:	Input and output signals of the truncated PEC cavity. The top part is for the constant amplitude input, and the bottom portion is for the quick fill input, reproduced courtesy of The Electromagnetics Academy.....	39

Figure 2.11:	Locations of the current and voltage monitors in the coupler. The inner and outer conductors are labeled for clarity, reproduced courtesy of The Electromagnetics Academy	40
Figure 2.12:	Voltage and current monitors across the coupler length for all the test cases used to investigate the quick fill method, reproduced courtesy of The Electromagnetics Academy	41
Figure 2.13:	Input and output signals of the truncated copper cavity. The top part is for the constant amplitude input, and the bottom portion is for the quick fill input, reproduced courtesy of The Electromagnetics Academy	42
Figure 2.14:	Input and output signals (top) and field energy (bottom) of the truncated PEC cavity with drift tubes. The time scale is the same for both parts, and the inset in the field energy shows a more detailed view of the energy for the steady state region, reproduced courtesy of The Electromagnetics Academy	45
Figure 2.15:	S-parameters (top) and field energy (bottom) of the DTL M4 tank used for simulations. The field energy is for the resonant frequency of 201.60 MHz applied for 5000 ns before the signal is cut-off complete to allow decay	47
Figure 2.16:	The input and output of the various times used to define the quick fill regions as given in Table 2.4	50
Figure 2.17:	Comparison of the calculated reflection magnitude to the measured power reflected in tank 1 of the DTL. The reflection magnitudes were calculated with the values of χ_e calculated from I/O signals and using a cavity response that was predicted	54
Figure 2.18:	S-parameters for the DTL tank 4 with a mesh fine enough to simulate the harmonics of the 201.25 MHz input frequency. The top portion shows the S-parameter near that input frequency, and the calculated frequency corresponding to the accelerating mode of the cavity is 202.23 MHz	57
Figure 2.19:	Field energy of tank 4 and the power coupler for the quick fill signal with the second and third harmonics added to the quick fill signal. The harmonics only affect the system energy early in the simulation (i.e. before ~2000 ns) when cavity fields are low and fields in the coupler	58
Figure 2.20:	Input and output signals of the quick fill with harmonics added	59
Figure 2.21:	Calculated mode amplitudes during steady state for the quick fill both with and without harmonics. The amplitudes of the baseline frequency and the harmonics are individually displayed	61
Figure 2.22:	Locations of voltage monitors used for simulation with harmonics added to the input signal. The centerline of the coupling foot is marked by a dashed line that is carried back to the voltage monitor at 0° for visualization	62

Figure 2.23:	Voltages across window at various azimuthal locations relative to the coupler foot. The voltage across the air surface of the window (top) and the voltage across the window thickness (bottom) both are measured at a number of angles as measured clockwise.....	63
Figure 2.24:	Response of cavity to a constant input frequency when the cavity shifts in its resonant frequency. The initial resonance frequency was set to be ω_{eff} for 50 ns, before being decreased in a linear manner over time to the resonance frequency calculated for the as is tank in CST	67
Figure 3.1:	Sample trajectories for an electron in a parallel plate geometry emitted with zero velocity both initially and upon each impact. The abscissa denotes the number of RF periods, and the ordinate is the location between plate 1 ($x/d = 0$) and plate 2 ($x/d = 1$).	74
Figure 3.2:	Sample trajectories for non-zero emission velocities. (a) the trajectory over 15 RF periods shows the broad and unpredictable effects that emission velocity can have on multipactor, and (b) a zoomed-in view of the trajectories of $v_0 = 0.02$ and $v_0 = 0.01$	76
Figure 3.3	Illustration of classic single-surface MP on a dielectric. Positive charges accumulated on the dielectric (“+”) generate a DC electric field (“EDC”) that restores electrons emitted at a speed v_0 and an angle of ϕ normal back to the surface. The RF electric field can then impart	78
Figure 3.4:	Emission points used in simulations. The left portion of the figure is the window location, and for the purposes of simulation this is set to be impenetrable. Those emission points set there are used for most simulations in this work as they are suited to investigating window MP	86
Figure 3.5:	Illustration of collision event in simulation. Upon collision at time step i , the position is likely to penetrate some depth into the surface, so the position is adjusted to be on the surface by placing it in the linear path between time step i and the calculated time step $i + 1$	88
Figure 3.6:	Sample emission energy distributions for various collision energies. The collision energies used are the maximum energy of each plot.....	90
Figure 3.7:	Comparison of multipactor using three different simulation techniques. The raw electron population (top), enhanced counter function (middle), and average secondary emission yield (bottom) were calculated for a coaxial line of the dimensions used in the DTL.....	95
Figure 3.8:	Secondary emission yield of DTL coupler using various emission velocities. The constant emission energy of 2 eV (a), emission energies stochastically calculated only for the initial collision of bound electrons or non-bound collisions (b), and stochastically determined emission energies.....	97

Figure 3.9:	Comparison of the secondary emission yields (unitless) of the 25 Ω and 50 Ω lines with the analytic predictions. Dashed line boxes indicate regions of two-surface MP, and solid line boxes are regions of one-surface MP	100
Figure 3.10:	Comparison of the average secondary emission yield with experimental results and simulations by Devanz of the TTF geometry © 2019 IEEE	102
Figure 3.11:	Secondary emission yields for the DTL coupler radii at the segments near the RF window (top), midway between the RF window and the accelerating cavity (middle), and near the accelerating cavity (bottom). The value of ζ for the input frequency of 201.25 MHz	103
Figure 3.12:	Comparison of secondary emission yield for varying numbers of time steps per RF cycle for the DTL geometry near the RF window. (a) $\Delta t = T/10$, (b) $\Delta t = T/100$, and (c) $\Delta t = T/500$	105
Figure 3.13:	Comparison of the percentage of collisions occurring on the RF window for 2D and 3D simulations.....	106
Figure 3.14:	Secondary emission yields for emission points at the electric maximum (parts a, c, and e) and at the magnetic maximum (parts b, d, and f) Reflection magnitudes used are 0.33 (parts a and b), 0.66 (parts c and d), and 0.99 (parts e and f).....	108
Figure 3.15:	Secondary emission yields in the absence of magnetic fields for emission points at the electric maximum (parts a, c, and e) and at the magnetic maximum (parts b, d, and f) Reflection magnitudes used are 0.33 (parts a and b), 0.66 (parts c and d), and 0.99 (parts e and f)	110
Figure 4.1:	The magnetic maxima are normalized to the wavelength so they range between -0.25 and 0.25 , and the RF window is located at zero with negative values indicating that the magnetic maximum is behind the window. Each bold line is the average value © 2019 IEEE	115
Figure 4.2:	Percent of collisions occurring on the window for the reflection phase of $\nu_b = -\pi$ (parts a, c, e and g) and $\nu_b = -0.835\pi$ (parts b, d, f and g). The reflection magnitudes are 0.245 (parts a and b), 0.49 (parts c and d), 0.735 (parts e and f), and 0.98 (parts g and h) © 2019 IEEE	120
Figure 4.3:	Secondary emission yield for the reflection phase of $\nu_b = -\pi$ (parts a, c, e and g) and $\nu_b = -0.835\pi$ (parts b, d, f and g). The reflection magnitudes are 0.245 (parts a and b), 0.49 (parts c and d), 0.735 (parts e and f), and 0.98 (parts g and h). The secondary emission yield maintains similar values © 2019 IEEE	121
Figure 4.4:	Ratio of the time between collisions (standing wave to traveling wave) for (a) magnetic maximum at the window location and (b) the magnetic maximum is behind the window. Many τ_{SW} values are reduced from τ_{TW} for $\chi_b = 0.98$ and $\nu_b = -0.835\pi$ © 2019 IEEE	122

Figure 4.5:	MP metrics for forward and backward propagating traveling waves. The metrics considered are the secondary emission yield (top) and the percentage of collisions occurring on the outer conductor (middle) and RF window (bottom)	125
Figure 4.6:	Secondary electron emission yield over varying power (P) in the abscissa and reflection magnitudes (χ_b) in the ordinate for the DTL geometry at 201.25 MHz. The various parts of the figure correspond to different reflection phases that place the magnetic maximum	127
Figure 4.7:	Percentage of collisions occurring on the RF window for $z_{MM} \leq 0$ for the DTL at a frequency of 201.25 MHz and a range of power levels (P) and reflection magnitudes (χ_b). Magnetic maxima are labeled as a fraction of the wavelength in the figure	128
Figure 4.8:	Percentage of collisions occurring on the RF window for select $z_{MM} > 0$ for the DTL at a frequency of 201.25 MHz and a range of power levels (P) and reflection magnitudes (χ_b). Magnetic maxima are labeled as a fraction of the wavelength in the figure	130
Figure 4.9:	Window collisions for a magnetic maximum located less than $0.125\lambda = 7.33 \text{ in.}$ in front of the window for a variety of reflection magnitudes. The window collisions are expressed as a fraction of the maximum percentage of collisions	131
Figure 4.10:	Growth parameters over varying power (P) in the abscissa and reflection magnitudes (χ_b) in the ordinate for the DTL geometry at 201.25 MHz. The various parts of the figure correspond to different reflection phases that place the magnetic maximum.....	133
Figure 4.11:	Secondary emission properties used for TiN. The secondary electron emission yield as measured by [77] is compared against the values from the Furman model using fitted parameters (top). Emission energy distributions for collision energies of 10 eV, 30 eV, 300 eV, and 1000 eV	136
Figure 4.12:	Comparison of the MP metrics for a backward propagating wave over various window materials. The metrics considered are the secondary emission yield (top) and the percentage of collisions occurring on the outer conductor (middle) and RF window (bottom).....	137
Figure 4.13:	Comparison of the MP metrics for a standing wave of $\chi_b = 0.95$ and $\nu_b = -0.8\pi$ over various window materials. The metrics considered are the secondary emission yield (top) and the percentage of collisions occurring on the outer conductor (middle) and RF window (bottom).....	139
Figure 4.14:	Comparison of the MP metrics for a forward propagating wave considering the inclusion of harmonics and window scattered HOMs. The metrics considered are the secondary emission yield (top) and the percentage of collisions occurring on the outer conductor (middle) and RF window (bottom).....	141

Figure 4.15:	Spatial distribution of electron collisions with the RF window (left) and the corresponding charge density of those collisions (right) for all collisions under the standing wave conditions $\chi_b = 0.95$ and $\nu_b = -0.95\pi$	143
Figure 4.16:	Change in growth parameters (top parts) and window collisions (bottom parts) for the backward propagating traveling wave (left parts) and the standing wave conditions of $\chi_b = 0.95$ and $\nu_b = -0.8\pi$ (right parts) for varying strengths of the DC field on the window	148

LIST OF TABLES

Table 2.1:	Material properties of Rexolite [14] and Alumina [4]	14
Table 2.2:	Amplitudes and phases of the TM_{0n} modes scattered by the RF window for forward power of the current geometry, a window without a vacuum-side notch, and a window of increased thickness, and for backward power incident on the current window design	25
Table 2.3:	Modes in frequency range of 200 MHz to 350 MHz of simple cavity used for investigating quick fill method.....	38
Table 2.4:	Simulation parameters of quick fill test cases	38
Table 2.5:	Q-factors as recalculated for test cases A and B and the change in field energy over steady state when applied to the quick fill method. The resonance frequency f_m changes from Table 2.4 due to changes in the software.....	45
Table 2.6:	Parameters for quick fill signals used to analyze the DTL cavity. The amplitude and phase of the reflected and emitted signals at steady state are also shown	48
Table 2.7:	Magnitude and phases for all harmonics of the output signal for the transient fill from 50 to 500 ns and for the steady state portion of the signal between 6050 and 7950 ns	60
Table 2.8:	Properties relevant to the excited TE_{11} mode in the coupler between the RF window and accelerator cavity	65

ACKNOWLEDGEMENTS

Chapter 2, in part, is a reprint of material as it appears in T.W. Hall, P.R. Bandaru, D.E. Rees, Progress in Electromagnetics Research **44**, 149-160 (2015), courtesy of The Electromagnetics Academy. The dissertation author was the primary investigator and author of the paper.

Chapters 3 and 4, in part, are reprints of material as it appears in T.W. Hall, P.R. Bandaru, D.E. Rees, IEEE Transactions on Plasma Science **47**, 1526-1533 (2019). The dissertation author was the primary investigator and author of the paper.

VITA

2010	B.S. in Nuclear Engineering, Purdue University
2013	M.S. in Nanoengineering, University of California San Diego
2013-2019	Graduate Student Researcher, Los Alamos National Laboratory
2019	Ph.D. in Engineering Sciences (Engineering Physics), University of California San Diego

ABSTRACT OF THE DISSERTATION

Electromagnetic and Multipactor Stresses on RF Windows in Drift Tube Linear Accelerators

by

Thomas Wesley Hall

Doctor of Philosophy in Engineering Sciences (Engineering Physics)

University of California San Diego, 2019

Professor Prabhakar Bandaru, Chair

Radio frequency (RF) particle accelerators are a key component to many scientific and industrial endeavors, so their reliable operation is of great concern. An obstacle to reliable operation has been the performance of the RF windows that act as barriers between the vacuum environment of the accelerating cavities and atmospheric conditions in the transmission line. Failures of these windows have a large impact on accelerator availability, and recovering from a window failure is a multiple day event. In order to mitigate these failures, an analysis of the stresses placed on the window has been performed. This dissertation presents simulations of the stresses placed on the window due to the electromagnetic environment and the multipactor effect with a discussion of how to minimize those stresses.

The electromagnetic environment was first analyzed using the commercially available CST

Microwave Studio software. An analysis of the window geometry in isolation from the accelerating cavity is performed first to minimize the stresses placed on it. Then the analysis of the whole system with the cavity present was performed using an approach that was developed to allow transient simulations of the highly resonant cavity. Simulations show how the signal develops over time, thus allowing adjustments to be made to the driving signal to minimize stresses. Simulations also demonstrate the effect of harmonics and their excitement of higher order modes, and the effect of an off-resonant cavity is briefly discussed.

Multipactor is a parasitic phenomenon whereby large electron populations accumulate and is common to accelerator systems. The principles and simulation techniques of multipactor are first presented, and benchmarks are presented to illustrate the validity of the simulations. The conditions of both traveling and standing waves are examined for the effect on multipactor development and electron collisions with the window. The broad analysis of many standing wave conditions allows for mitigation of multipactor in consideration of the signal analyzed in the electromagnetic simulations. Effects of window material and charge accumulation on the window are discussed, and the consideration of the harmonics and higher order modes analyzed previously are shown to have negligible effect on multipactor.

Chapter 1

Introduction

1.1 History of particle accelerators

The radiofrequency (RF) powered particle accelerators that emerged in the twentieth century have become invaluable tools in both advancing scientific discovery and practical applications. One area where the accelerator operation can go awry is in the delivery of the RF power to the accelerating cavity, and within these complicated systems, one of the most basic components that is particularly susceptible to malfunction is the dielectric RF window [1] [2] [3] [4] [5] [6] [7] [8] [9] [10]. These windows are simply dielectric barriers between the vacuum and atmospheric conditions that exist in the accelerator cavity and RF generation and transmission lines respectively, but should that barrier fail, accelerator operation must halt until the window can be replaced. This has been a problem historically, and with multiple failures having occurred within single run cycles at the Los Alamos Neutron Science Center (LANSCE) [11], the mitigation of window failures has been identified as a key factor in the reliability of its operation, and thus the operation of particle accelerators as a whole.

The first development RF powered accelerators was the drift tube linear accelerator (DTL) proposed by Luis Alvarez. The earliest particle accelerators were simple anode-cathode setups whereby the voltage between them acted to accelerate electrons from the anode to the cathode, and by shaping the electrodes to be tubes through which the electrons could travel, Rolf Widerøe built accelerators that utilized alternating electric fields to accelerate electrons through a series of electrodes, thereby achieving greater speeds. Those drift tubes acted to shield the particle beam from decelerating fields while the beam traversed the tube length, but effective use of drift tubes could not feasibly achieve acceleration that was of interest for the physics research of the time. The solution to this was to utilize the high frequency generators that had been developed for World War II to establish large electromagnetic (EM) fields in the accelerating cavity that housed the drift tubes so that greater

acceleration could be achieved between each drift tube. This system could properly accelerate light particles such as electrons while avoiding the unfeasibly large scales of drift tubes that would have arisen in Widerøe's design. Building tubes of sufficient length will always become impractical for acceleration above certain energies, and as a result there have been other accelerator types developed to reach higher energies than can be achieved with a DTL.

1.2: Los Alamos Neutron Science Center

Originally conceived as the Los Alamos Meson Physics Facility, the DTL was built to produce intense beams of pi-mesons that could be used for studying nuclear structures [11] [12]. The role of the facility has shifted since being built in the 1970's as indicated by the name change to the Los Alamos Neutron Science Center in 1995, and today hosts five different facilities that are open to researchers both within the laboratory and from universities and laboratories around the world. These facilities include the Isotope Production Facility, which supplies isotopes for medicine, research, and industry, the Proton Radiography Facility, which uses the accelerated proton directly to produce dynamic images vital to various materials research; and the three neutron facilities of the Lujan Center, Ultra-cold neutrons, and Weapons Neutron Research. The neutron facilities use a tungsten spallation source and varying levels of neutron moderation to conduct research on areas ranging from the nuclear stockpile to high-precision nuclear measurements. With the high number of experimental capabilities dependent on the linear accelerator, its consistent operation is essential. Furthermore, other facilities worldwide share some of the same issues as this facility, and by examining the issues that arise within the DTL at LANSCE, insights into the operation of similar facilities can also be gained.

There are three parts to the accelerator at LANSCE: the ion source, the DTL, and the side-coupled linear accelerator. Acceleration starts with the production of the H^- and H^+ sources, then the H^- / H^+ particle beam is accelerated through the DTL section. The tank geometry, drift tube sizes and particle energies were concomitantly considered in the design of the DTL section so that it operates at

201.25 MHz, and in order for the acceleration cavity to operate at that mode and to allow for the fields to be properly established, this section consists of four tanks. The particle beam is accelerated up to 100 MeV in this portion of the accelerator, and from there the beam is either directed to the Isotope Production Facility or continues into the side-coupled linear accelerator. Instead of using drift tubes to shield the beam from decelerating fields, the side coupled linear accelerator designs the resonance of the cavity such that polarity alternates between cells in the cavity, and as the beam is accelerated the polarity of those cells is adjusted to allow for constant acceleration. This change is necessary because of the size of drift tubes that would be necessary as the proton reaches 100 MeV from the first stage. The side-coupled linear accelerator operates at 805 MHz and accelerates the beam up to 800 MeV, after which the beam is delivered to the remaining four facilities. The operation of the whole facility requires many supporting system (i.e. the power supply, cooling systems, various probes and monitors, controls, etc.), and the loss of any of these systems can necessitate the accelerator be shut down for repair. This can be a particular problem when the user schedule is full and a failure results in user backlogs, so mitigation of failures is of high concern to accelerator operations.

The operation of the accelerator requires large EM fields to be accumulated within the cavity, so a significant part of the accelerator system is the supply of the RF power that establishes the accelerating fields in the cavity. The RF power is generated in tetrodes then carried to the DTL via coaxial transmission lines and is generated in klystrons the carried to the side-coupled linear accelerator via rectangular waveguides. As previously noted, the accelerating cavity must be maintained at vacuum conditions to provide a path for the beam that minimizes potential collisions, but maintaining a vacuum over the space of the power supply lines is unfeasible. To that end, a vital component of the power supply lines is the RF window that provides a barrier between vacuum and atmospheric conditions in the transmission line. This robustness of the RF window has been an issue historically, and continues to be a problem for continuous power delivery to the accelerator system.

1.3: RF windows in DTL power couplers

The RF window has several design needs and can fail with regularity. As its main function is to provide a barrier between vacuum and atmosphere, it should be capable of maintaining a seal that can withstand the pressure difference imposed on it [1] [2] [3]. In the DTL at LANSCE, this is achieved by locking it into place with geometries of the window and conductors fitting together as shown in Fig 1.1, but some facilities such as the TESLA Test Facility (TTF) use a window that is welded into place [10]. This also means that the material from which the window is made must be strong enough to withstand the pressure difference on its surface, but these mechanical criteria must also be evaluated in terms of the electrical performance of the window.

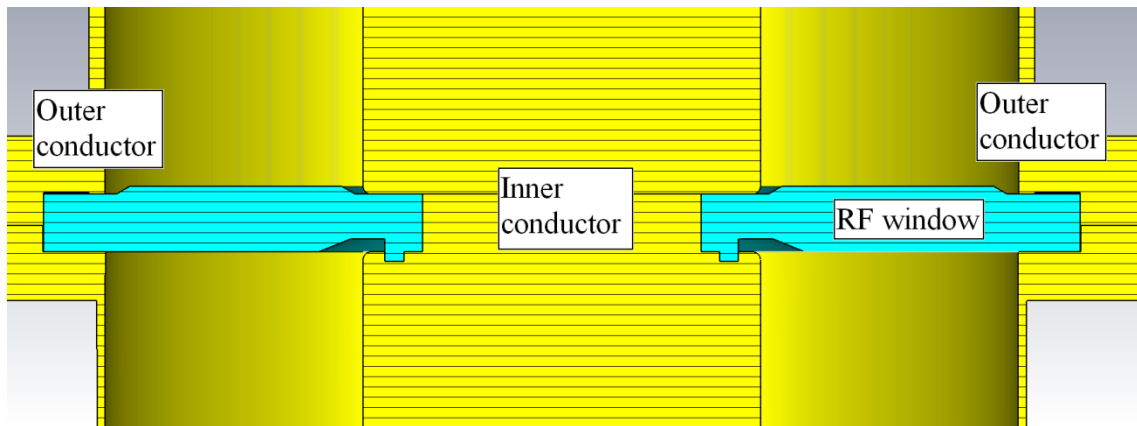


Figure 1.1: Illustration of RF window in coaxial line. The window is secured by the interlocking of conductor and window geometries.

1.3.1: Requirements of RF window

The window should not affect the RF pulse that travels through the transmission line, but since it will not have the same properties of air, it must be designed to avoid interruptions in the transmission of the signal. First, it is apparent that a dielectric material must be used to avoid currents flowing through it that would in essence terminate the transmission line. A common material choice is alumina, and for the DTL this material is Rexolite®, a cross-linked poly-styrene. The relative electric

permittivity of window materials is elevated (i.e. $\epsilon_r = 2.53$ for Rexolite), so the window geometry must be designed to avoid the reflection of the RF signal at the window. For the DTL, this means that the radii of the inner and outer conductors must be modified at the window location such that the characteristic impedance at the window location is $50\ \Omega$ like the rest of the line. This works well with the first requirement, as the inner conductor radius is made smaller and the outer conductor radius made larger, thus allowing the window to be confined by the geometry of the conductors. The conductor radii for the Rexolite window are illustrated in Fig 1.1, but the exact change to radii is dependent on material permittivity. This is an improvement over the solution at TTF, where the window is welded into the line. Since the geometry of the conductors in that line does not change, the width of the window must be set to the half wavelength of the RF signal to effectively remove reflections, and this thick window can lead to significant power dissipation [10] [13].

With the window design making it invisible to the RF signal, there are a few remaining factors to consider. First, the breakdown threshold of the dielectric must be high enough to withstand the electric fields it will be subjected to. This is dependent upon the material, but considering the magnitude of operating power (\sim MW) in a $50\ \Omega$ line, the voltage magnitudes (\sim 1 to 10 kV) will not exceed typical dielectric strengths of the dielectrics (\sim 10 kV/m in transmission line versus \sim 10 MV/m dielectric strength). However, this should be kept in mind during design and operation, as small changes to conditions can lead to unexpected failures or spikes in the fields at the window. Another issue is that of the thermal stress on the window. This can be managed by selecting the window material to provide adequate means of dissipating heat from the bulk while still minimizing the power dissipated in the window from the RF source. Again, a small deviation from the expected conditions could also lead to the other mechanical and electric properties changing so the window is no longer operating as designed, or it could also fail outright.

1.3.2: History of RF window failures

A large number of window failures have occurred at LANSCE over the years. Extensive

records of maintenance work and downtime reports show that issues have necessitated the repair and replacement of many windows that could no longer maintain a vacuum, and at times attempts to persist in using failed windows has led to the damage of components elsewhere in the system due to the complex nature of maintaining a vacuum over such intense EM conditions. These failures then led to many hours of downtime for repair (at least 4 to 5 hours on the low end, with >24 hours being common), and that downtime also required at least that much and often several times more worker hours to correct. Once repaired, vacuum recovery takes an additional day, and conditioning of the system requires an additional one to three days as well, making for several days for the system to come online. These failures are then costly to the operators and consumers of the accelerator beam, and must be mitigated.

One observation in connection to the window failures was the recording of arcing. Arcing occurs as the voltage exceeds the breakdown threshold, allowing a current to move through the vacuum in the cavity or coupler, and the high EM fields used in particle acceleration can readily lead to its occurrence, so arc detectors have been utilized in the accelerator system at LANSCE. These detectors are placed at various locations, most notably in the cavity and in the coupler to detect window arcs. A positive correlation between arcing in the cavity and in the coupler has been qualitatively observed, and increases in window arcing has also been positively correlated with window failure. This arcing has also been observed to occur between RF pulses, meaning that charges must have accumulated on the window to allow for the arcing activity.

The details of window failures at LANSCE have shown the failure of windows to be dependent on the total system operation. For example, the occurrence of window failures is not equal across all accelerator cavities, even though the geometry of the window is the same for all cavities, indicating that there is something in the cavity physics that alters window performance. Additionally, there has since been a major change to the window geometry and mounting structures, which did not solve the issues of window failures. In fact, the failure of windows has often occurred in bursts of several failures in a month, and one of these upticks in failures occurred in late 2012/early 2013 after the window

geometry had been improved by moving it further upstream in the transmission line where there will be less stress due to high cavity fields. Clearly factors not initially designed for have had significant effects. One factor identified, for example, has been simply contamination in air that can lead to dust accumulating on the window surface and subsequent arcing and failures. Or alternatively, the application of a titanium coating to the window proved to make the necessary step of conditioning nearly impossible, rendering the attempt at improvement useless.

The failures since the 2012/2013 cycle have shown a high incidence of worming, a mechanism whereby electrons bore through the bulk of the window. The observation of these failures is beneficial in that they are highly localized, and in particular worming was only observed within $\pm 30^\circ$ of the coupler loop centerline. This provides strong evidence that those failures were the result of the field physics at the coupler loop, again reinforcing the effect of the whole system on window performance. Other damage was observed in 2015 whereby the plastic of the window showed signs of highly localized melting, indicating high temperature increases in small areas. This localized heating was also observed in subsequent measurements but was quickly resolved. The volatility of these failures necessitates extensive investigation to reduce the potential stresses as well as possible since many unknown factors can result in sudden and drastic failures.

1.3.3: Potential failure mechanisms

The failure mechanisms of these windows can largely be deduced from observations of the physical damage. Some damage does not appear to be sufficient to cause the window failure, such as the discoloration on both the air and vacuum surfaces. The air side of the window has an elevated area where there are dendritic tracking marks, indicating an arcing event occurs on this surface, presumably from short periods of the voltage exceeding the breakdown strength at the air-Rexolite interface, and the vacuum side will often have patches of discoloration from irradiation. While the accelerator system will operate at powers that have electric fields well below what would cause arcing throughout the dielectric media found in the line [14], other unavoidable factors such as surface imperfections,

interface phenomena, x-rays, fatigue, etc. can potentially lower the breakdown strength to be below the fields present.. These factors can then initiate some degree of damage, possibly explaining the discoloration that is observed, but they also do not appear to lead to window failure themselves. Mitigation of these phenomena however should be attempted as more serious damage could arise due to the window integrity becoming compromised by them. In addition to the discoloration, some failures have appeared to have been caused by thermal failures, i.e. melting, under specific conditions, but as these are rare and have been observed to occur after maintenance work, they are assumed to be best mitigated by protocol as opposed to engineering.

Another observed form of damage that appears to be more catastrophic is the presence of worming that extends over the volume of the window itself, potentially leading to a loss of vacuum [15] as well as a pathway for further arcing. Furthermore, this damage should not occur considering the EM conditions of coaxial lines as the electric fields normal to the window surface are minimal and well below the dielectric breakdown strength of Rexolite, indicating that the EM fields themselves are not sufficient to explain the conditions. This form of damage could be affected by the former damage types, and even some of the observed discoloration itself could be an indication of some of the unpredicted conditions present near the window that lead to failure.

The underlying mechanisms by which all these discussed failures could occur must therefore be identified. To that end, the electromagnetic conditions of the window must first be analyzed. This is necessary first to understand the fields near the window, as EM stresses must be minimized to avoid processes that could damage the window but are not predicted under standard operation. These are the issues that can lead to the discoloration that was observed and over time can lead to total window failure. Once the field conditions are understood and accounted for throughout the transient signal, the phenomenon of multipactor can be analyzed. This phenomenon is a common issue in accelerator systems and is caused by electrons being accelerated through the vacuum region to collide with surfaces at times and energies that generate more free electrons, thus an avalanche event occurs [16]. Multipactor

has been well studied in this dissertation, particularly in relation to both the worming and observed arcing between RF pulses.

The effect of multipactor on the performance of the window must be examined to minimize failures, as multipactor is known to cause damage similar to the observed worming [7] [17]. The commonplace occurrence of multipactor in accelerator systems is already known to lead to failures of RF windows due to several factors such as heat dissipated by the process, changes to material properties, and increased EM stresses, and the failures that have been observed to occur in the accelerator system have the characteristics of multipactor, making this a likely candidate to explain recent failures. The multipactor process is a complicated phenomenon with many considerations that makes its prediction impossible by analytic means, and as a result, mitigation of this phenomenon requires accurate simulations. The accelerator system operation parameters will be discussed in detail to explain how multipactor might be responsible for window failures and what can be done to avoid them in the future.

In order to examine multipactor in the coupler near the RF window, the simulation of the phenomenon will first be established. The multipactor phenomenon has classically been discussed in terms of its occurrence on either two conductor surfaces or one dielectric surface, but the power coupler transmission line has both of these features, requiring an in depth analysis of multipactor in this particular system. The classic multipactor processes have resulted in useful metrics for determining the occurrence of multipactor in simplified systems, and these metrics can then be used to both simplify what parameters must be studied in the coupler and to benchmark the accuracy of the simulations that are carried out. As such, an in depth discussion of the multipactor must begin with these established processes before moving on to the specific details pertinent to the RF window.

With the simulation and underlying principles established, multipactor near the RF window can be analyzed in terms of the many adjustable parameters required for proper beam acceleration and the subsequent reaction of the cavity to the input signal, and one of the most significant parameters to

be considered is that of the signal reflection. The reflection of the input signal will result in a standing wave, which has been shown to effect the migration of electrons in the axial direction, and this migration has the potential to cause electron collisions with the RF window, leading to damage. Other items of interest will also include the effect of anomalous EM fields that might be shown to be present and the window geometry and material. All of these factors must be considered to provide a sufficient analysis of MP in the presence of the RF window.

Chapter 2

Electromagnetic Analysis

2.1: Introduction

The first issue to be considered in the reliable operation of the RF window is the EM environment in which it is placed. The high electric fields ($\sim\text{kV/m}$) that are present in the power coupler can affect the window performance directly, and the RF signals can also dissipate heat into the window that is potentially damaging. Analysis of the fields in the vicinity of the window requires numerical methods due to the highly complex geometry of the coupler and the accelerator system as a whole, so the commercially available CST Microwave StudioTM is utilized in this work. The EM analysis consists of a preliminary investigation of fields in the vicinity of only the RF window, followed by a more rigorous look at the entire accelerator system.

CST Microwave StudioTM was utilized for this work because of its accuracy and capabilities in simulating complex geometries [9] [18] [19] [20]. This software uses a finite difference method to calculate the fields, and there are multiple solver types with the most pertinent being the time-domain and the frequency domain methods. Using these solvers, not only can the EM fields be directly calculated, but other useful information such as energy stored in the system and S-parameters are also calculated, allowing for a more exhaustive analysis of the RF window and potential modes of failure.

There are multiple solver types available in the CST software, so the choice had to be made about which solver to use. Some, such as the eigenmode solver, could be excluded outright due to their inadequacies in providing the requisite information on EM fields in particular locations and operating conditions, and so the only two candidates are the time-domain and frequency-domain solvers. These solvers are similar in that they both utilize a discrete grid to define the differential components of Maxwell's Equations in terms of the electric and magnetic field values at those defined points (the FD method), and both solvers analyze the response of the device in question to an input

signal. For the closed system consisting of the accelerator coupler and cavity system, the input is simply a “port” that is placed at an arbitrary axial location in the power coupler, and the first step of the CST calculations is to calculate the modes present at the port, which for the coaxial transmission line will be the transverse electromagnetic (TEM) mode [21]. The time and frequency domain solvers differ in that the frequency domain assumes the fields are of a time harmonic nature so that the fields are calculated for specific frequencies, whereas the time domain takes whatever time-dependent input and simulates the system response to it. If any transient property of the RF signal is necessary, as is the case with the RF window, then the time domain solver must be used.

The EM analysis consists of two parts. The first is to consider the coupler itself so that the fields near the window can be analyzed in terms of a simple traveling wave signal. Those results can then be extrapolated to the case of the coupler as it is connected to the accelerator cavity, with some notable exceptions to be discussed later. The second part involves the addition of the accelerator cavity, where transient fields inside the cavity will greatly affect the fields in the coupler via changes to the reflected signal as the cavity field is established within the resonant structure over a span of $\sim 100 \mu\text{s}$. This transient reflection will alter the traveling wave nature of the RF signal to be a standing wave during some portions of the signal and is vital to addressing the window operation.

2.2: Power coupler and window without accelerating cavity

The coupler without the accelerating cavity is first studied to understand the mitigation of the stresses on the window due to the EM fields. The RF window must withstand electromagnetic, mechanical and thermal stresses, so these must be understood in order to ensure continuous window operation. Of these, the mechanical stresses will be of the least concern here because they have not been observed independent of evidence of other failure mechanisms, such as those due to EM stresses. As such, there is no reason to believe that mechanical stresses are responsible for the failures of the window.

2.2.1: Window stresses

The thermal stresses are perhaps more parasitic to window operation but still not likely to be the source of the failures that have been observed at LANSCE. The RF window routinely experiences heating by RF power being dissipated in its volume, although this heating will be low due to the use of pulsed power and the material properties of the window. Additionally, multipactor can contribute significantly to thermal stress, but mitigation of this phenomenon is necessary to avoid other issues such as absorption of RF power by the electron population and window charging, so analysis of its contribution to thermal stresses is secondary to avoiding it altogether.

There are a few ways to mitigate stresses on the window. Thermal stresses are managed by blowing air across the window surface to decrease the temperature gradients that can lead to failures, and another obvious solution is to ensure that the window material has properties sufficient to meet the demands that all the stresses place on the window. In general, this will have already been addressed in the initial accelerator design as the basic need to provide an electrically invisible barrier that maintains the vacuum, but atypical conditions must also be considered in material selection. The other consideration that is often employed is the geometry of the window, including its axial placement in the coupler and its general shape. This can have a significant effect on the stresses placed on the window and as such will be an important factor to consider. Finally, the RF signal itself can be modified to minimize window stress by taking into account the full transient response of the coupler and cavity.

The material used in the window must withstand the mechanical, thermal, and electromagnetic stresses placed on it. The material used should be resistant to cracking under the pressure differential and the stresses caused by heating and subsequent thermal expansion, and given the common use of ceramics and plastics, these should be readily met. Within those commonly used materials, the thermal properties can be selected to minimize stresses. These properties include a low thermal expansion coefficient and a high thermal conduction to minimize mechanical stresses and temperature differentials within the window respectively. The desirable EM properties of the material include a low loss tangent,

a low dielectric constant, and a high dielectric breakdown strength in order to reduce heat accumulation, to better match the window impedance to the rest of the line, and to avoid breakdown respectively. It should be noted that some of these can change after “conditioning,” whereby the window has experienced many cycles of high RF power, but that is outside the scope of this work and generally improves those traits. The material that has been used at LANSCE is Rexolite®, a cross-linked polystyrene plastic designed for high voltage uses. This generally has very good properties as compared to other commonly used materials, such as alumina, see Table 2.1, so there is no further consideration of the material until chapter 4 when multipactor is discussed.

Table 2.1: Material properties of Rexolite [14] and Alumina [4].

Property	Alumina	Rexolite
Density (g/cm ³)	3.75	1.05
Thermal conductivity (W/mK)	20	146.4
Thermal expansion coefficient 25-400 °C ($\times 10^6 / ^\circ\text{C}$)	7.2	0.21
Dielectric constant	9.4	2.53
Dissipation factor, 1MHz	0.0004	0.00012
Dielectric Strength (MV/m)	15	19.7

2.2.2: Window geometry

The design of the window geometry requires the consideration of several factors [8] [9] [10] [22]. First is its axial location. The input signal will experience reflections from the line terminus and the cavity fields leaking back into the coupler, and this results in a standing wave being established in the coupler that allows fields near the window to be altered by moving it in relation to this standing wave. The reflections are dependent upon the transient properties of the cavity, and as such this will be analyzed in the next section. The next consideration is that of the window size. In order to minimize reflections, the radii of the window must be set to match the impedance of the line. Since the ratio of the radii is what determines the impedance of a coaxial line ($Z_0 = \frac{\eta_0 \ln(r_o/r_i)}{2\pi\sqrt{\epsilon_r}}$) [21], there is some leeway

in defining the inner and outer radii (r_i and r_o respectively) to reduce EM stress, but the difference in either radius between the air/vacuum and the window should still be sufficient to allow the window to make a seal and maintain vacuum conditions. The shape of the window itself can also be altered to better mitigate stresses, with two typical alternatives being the cylindrical and conical shapes.

The cylindrical RF window will be considered here for a few reasons. The first is that this is the window presently used in the DTL at LANSCE, so design changes could potentially be employed with minimal changes to the surrounding portions of the coupler, whereas a conical section would require new conductor geometries as well to secure the window and create a seal that maintains vacuum. The other reason is that a conical window requires greater care ensure the RF signal is not reflected by the window as the line impedance will change throughout the axial length of the window. For these reasons, a conical design will not be considered in this dissertation.

This leaves limited options in how the geometry of the window can be modified to improve performance. The current window design has two notches, one that goes into the window volume on the vacuum side and one that extends from the window on the air side as shown in Fig 2.1. This window geometry should help to reduce the voltage across the window on either surface as heuristically increasing the length across the window will decrease the voltage. This is particularly important on the air side, where there were apparent tracking marks visible on many window specimens, and in general the window surfaces present an increased risk to anomalous discharges due to changes from bulk properties at the interface. The changes to the window geometry will only be able to decrease these voltages by so much, but if there is a reduction of a few hundred volts, this could be significant enough to avoid the issues that have been observed. Altering the geometry can potentially do this considering that the voltages are in the kV range.

A rudimentary investigation of the effect of varying the height and number of notches on the window might provide insight on how to reduce the surface potentials so that the possibility of flashover is also reduced. Increasing the height of either the air or vacuum side notch will increase the length

across which the voltage would have to travel and thus decrease the voltage, and adding additional notches could also achieve this. Of course, the height of the air side notch is somewhat limited because the window requires some bulk to maintain its integrity. The notch in the vacuum side goes into the volume of the window, thereby reducing the thickness of the window, so reducing this thickness too much is undesirable and could exacerbate the failures that were observed as branching into the window volume at this location. Since the electric field is stronger near the inner conductor, two heights will be used for the air side notch to investigate whether this could be beneficial. The variable heights are shown in Fig 2.1, along with the path over which the voltage will be measured.

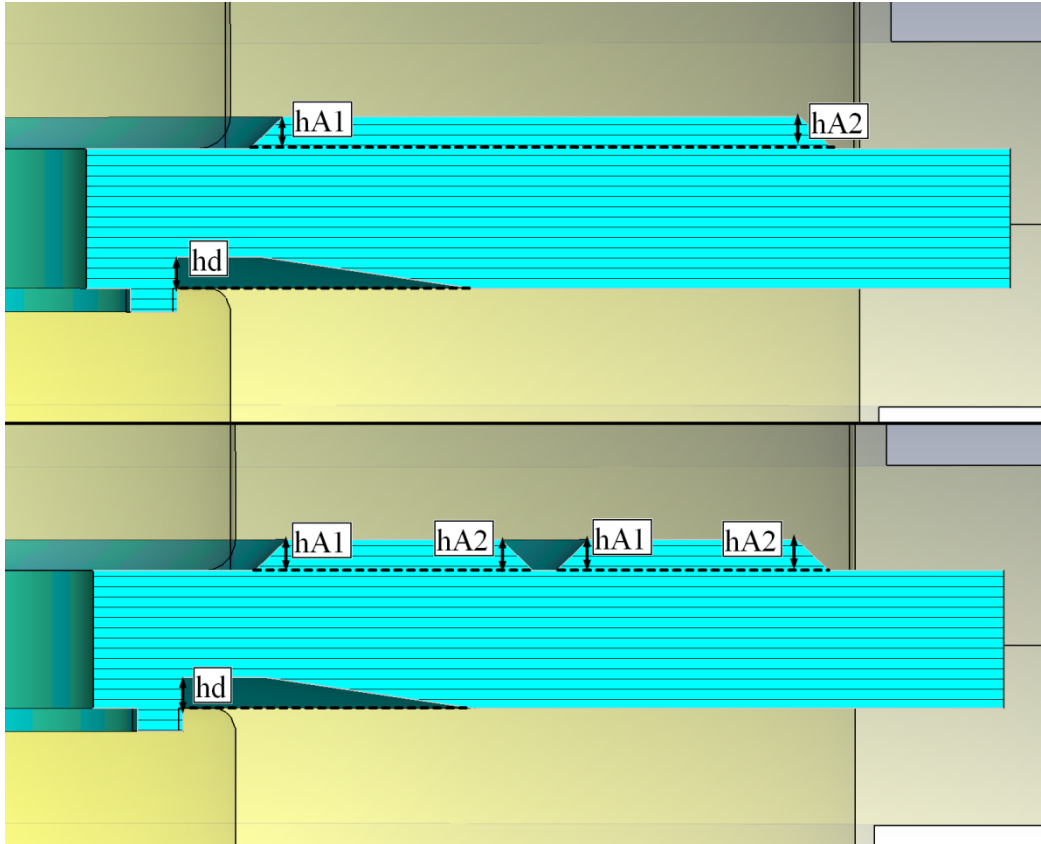


Figure 2.1: Window geometries used to investigate the EM fields in the coupler. The inner conductor is on the left side of the image, and the outer conductor is to the right. The top portion has one notch on the air side, and the bottom portion has two air-side notches. The inner portion of the notches is raised by $hA1$ from the surface, and the outer portion of the notches is raised by $hA2$. The vacuum side notch goes into the window volume by the amount hd .

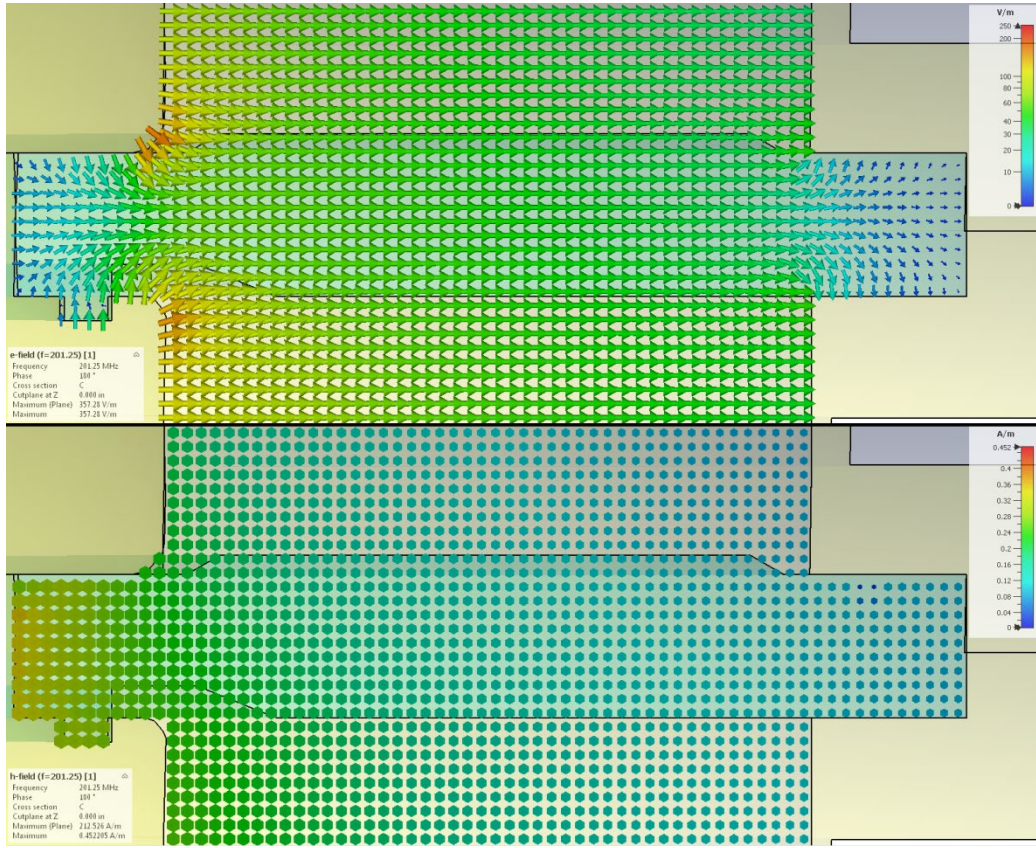


Figure 2.2: Electric (top) and magnetic (bottom) fields for the DTL window as is. The electric field has apparent changes to its axial component near the window.

Simulations were performed over a range of values for each height parameter. The air side notch heights $hA1$ and $hA2$ were varied from 0.04 in. to 0.2 in. by 0.04 in. increments, and the vacuum side height (hd) spanned 0 to 0.2 in. by 0.05 in. increments. These notch heights were selected to be similar to the measurements of the current window design ($hA1 = hA2 = 0.12$ in. and $hd = 0.2$ in.), with the increments allowing the current design to also be measured. The maximum air notch height was selected to match the bevel radius on the corner of the inner conductor as it was assumed this would not significantly affect the line impedance, and the maximum vacuum notch height was selected to be the same as the notch of the current window design. In order to make these calculations, the frequency range within CST was set to be 0 to 402.5 MHz, which minimizes the pulse width of the automatically generated Gaussian pulse used as the excitation signal. The electric and magnetic fields were recorded

for 201.25 MHz (calculated automatically in CST from Fourier transforms of the frequency range), and the results are shown in Fig 2.2. These fields exhibit the TEM mode expected for a coaxial line, but since the axial direction becomes normal to the conductor surfaces at its interface with the window, an axial component is added to the electric field. This can be expressed as an excitation of higher order modes (HOM) in the line, and these HOMs will be discussed in more detail shortly. Currently, it should be noted that this could affect the voltage across the window surface as it could potentially increase the tangential electric field along the portions of the window voltage paths that have an axial component.

In general the addition of length across the window surface does decrease the voltage, as seen in Fig 2.3. The voltage across the vacuum surface in Fig 2.3b is not expected to be as significant as the voltage across the air surface due to the lack of evidence of RF tracking on window samples, but its minimization is still preferred to avoid unforeseen failures. Unsurprisingly, there was not a significant effect of the air side notches on the vacuum side voltages, but varying vacuum notch heights did provide a result of interest. The vacuum voltage sharply increased from a vacuum notch height of zero to 0.05 in., then slowly decreased as the notch height increased. The drop in voltage for a lack of any notch in the vacuum side ($hd = 0$) is due to the lack of any tangential electric field component for a radial value less than the inner conductor radius, as the window surface is in contact with the inner conductor at these points. With a moderate notch in the vacuum side, the component of the electric field tangential to the window surface increases, resulting in the voltage increasing by around 0.2V, but this increase in the vacuum voltage decreases as the window notch increases. The current design does minimize the vacuum surface voltage, although the lack of the vacuum side notch is similar and could provide further benefits to be discussed in the next subsection.

The voltage across the air surface can be significantly reduced by modifying the window geometry. Again, the voltage is decreased by altering the field component tangential to the surface either by changing the air side notch height or spitting it into two notches. For parameter sets where $hA2 > 0.08$ in., the use of two notches had significantly lower voltages than the window with only

one. However, low $hA2$ values will produce shallower changes to surface geometry with higher tangential components in the radial direction, and as such voltages with similar or even higher values for the two-notched window are not unreasonable. There are some differences with changes to the vacuum side notch, but these predictably are not of significant consequence.

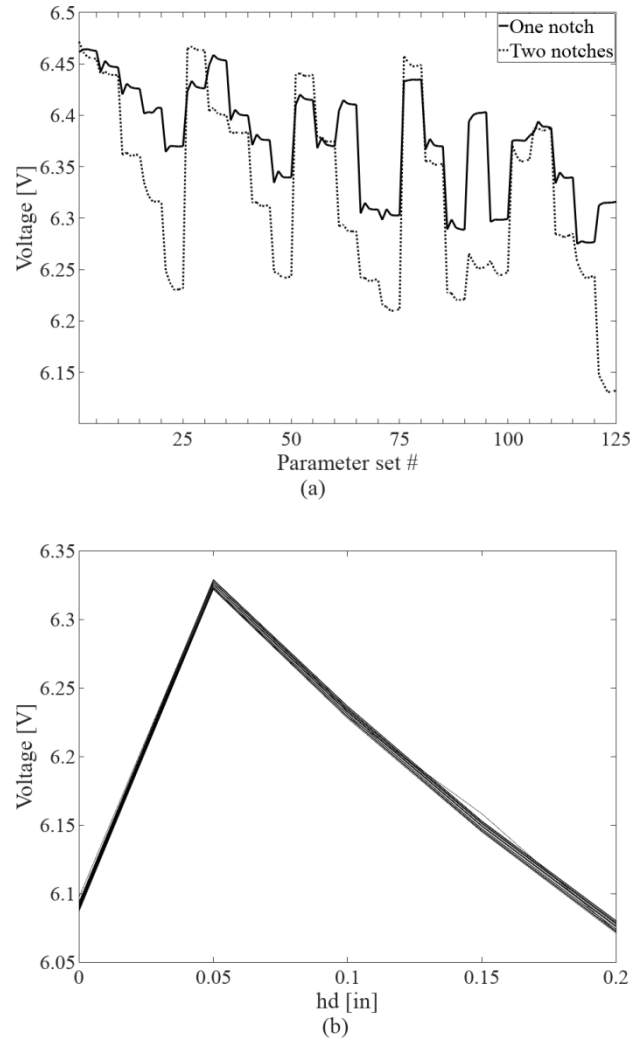


Figure 2.3: Voltages resulting from various notch geometries. (a) shows the voltages across the air surface of the window, and (b) shows the voltage across the vacuum surface of the window. The parameter sets used in (a) are in sorted first by $hA1$, then by $hA2$, then by hd . The two different geometries had observable results on the air side, but not the vacuum side, simplifying the considerations to be made in engineering the window geometry. Voltages shown are for normalized power of 1 W, so DTL operation on the order of 1 MW will increase values by a factor of 1000.

One interesting note about these voltages for the one-notch geometry is that there is a spike in its value when $hA1 = hA2$. Looking at the first 25 parameter sets (where $hd = 0$, $hA1 = 0.04 \text{ in.}$, and $0.04 \text{ in.} \leq hA2 \leq 0.2 \text{ in.}$), the voltages decrease with $hA2$ as expected, and this trend generally continues for other values of $hA1$ with the exception of those combinations where $hA1 = hA2$. With that combination of parameters, there is a large segment of the RF window parallel to the radial direction, so the component of the electric field tangential to the window surface is the dominant radial component of the electric field. This is in opposition to the parameter sets with $hA1 \neq hA2$ that reduce the tangential component by transferring the radially oriented electric field to being no longer parallel to the window surface. This effect is important to the current design of the window as the notch has measurements of $hA1 = hA2 = 0.12 \text{ in.}$ corresponding to parameter set 65 in Fig 2.3b.

The current design has one of the highest voltages of any of those shown in Fig 2.3a, so reducing the EM stress on the window can be accomplished by changing just the geometry alone. It should be noted that the voltages shown in Fig 2.3 are for a power input of only 1 W, and so when the input power is increased to the range of MW, the order of voltage differences goes from $\sim 100 \text{ mV}$ to $\sim 100 \text{ V}$. This difference in voltages might be significant enough to prevent some of the surface tracking that was observed on the air side of the window, although the extent of this difference is not known. This change could be made with negligible difference to cost, but it is also unclear how significant the potential reduction in surface tracking would be to the overall window performance. This particular form of discharge doesn't lead to failure in and of itself, although its prevention could be useful in maintaining the material properties. It is also possible that changes to window geometry could affect its performance in unpredictable ways, such as new failures at the reduced window thickness between the newly formed two-notches or some issues with sharper corners when there is a large difference between $hA1$ and $hA2$. To that end, the current design will be utilized throughout the rest of the EM simulations, but it is still possible that the modification of the window could prove useful.

2.2.3: Excitation of higher order modes

Another issue that must be discussed in the design of the window geometry is the excitation of higher order modes (HOMs) from the interruption in line geometry at the window. Aberrations in geometries are bound to excite some HOMs, and there is a good heuristic reason to expect TM_{0n} modes to be excited from the window geometry. When the electric fields are considered to be the result of charges on the conductor surfaces, it is easy to conceptualize that charges will then introduce an axial component of the electric field (thus TM modes) at the window where the vector normal to the conductor surface is in the axial direction. This can be seen in Fig 2.2. Additionally, since there is no variation in the geometry in the azimuthal direction, those scattered fields should have no variations in the azimuthal direction (indicated by the “0” subscript in TM_{0n}).

The excitation of HOM in the coupler can also be investigated in CST by placing a port near the RF window with a high number of modes to be considered in its calculations. CST is capable of calculating the port mode type and cut-off frequency, and those cut-off frequencies calculated by CST are shown in Fig 2.4. CST calculates the modes in order of ascending frequency, leading to only two TM_{0n} modes within the first 51 modes calculated. This means that many more modes are required to be set in the port in CST to get more TM_{0n} modes, and the implications of this are discussed shortly.

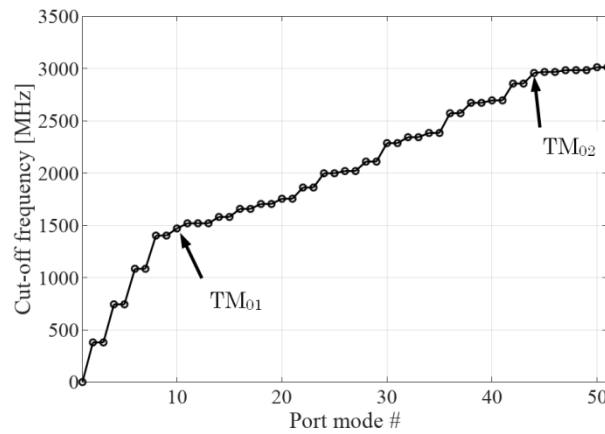


Figure 2.4: Cut-off frequencies of higher order modes in DTL.

The cut-off frequency is simply the frequency corresponding to the transverse wavenumber k_t , which for the coaxial line includes the radial and azimuthal components, and this wavenumber can be found by combining Faraday's law and Maxwell-Ampère's law and solving for cylindrical coordinates such that [21]

$$\det \begin{pmatrix} J_m(k_t r_i) & Y_m(k_t r_i) \\ J_m(k_t r_o) & Y_m(k_t r_o) \end{pmatrix} = 0 \quad (2.1)$$

where J_m and Y_m are the Bessel functions of the first and second kind respectively for transverse magnetic (TM) modes and the first derivative in the radial direction of the Bessel functions for the transverse electric (TE) modes, and r_i and r_o are the radii of the inner and outer conductors respectively. The transverse wavenumber (k_t) is related to the axial wavenumber (k_z) (the propagating direction) and the wavenumber of the RF signal (k) by $k^2 = k_t^2 + k_z^2$, and it is apparent from this that if $k < k_t$ the value of k_z will be imaginary, physically resulting in the signal decaying as it propagates. This is why the port must be placed near the window, as the input frequency of 201.25 MHz is well below even the lowest frequency of the higher order modes at 379.53 MHz (see Fig 2.4), and so by extension is also below the cutoff frequencies of the relevant TM₀₁ (1.47 GHz) and the TM₀₂ (3.20 GHz) modes (labeled in Fig 2.4). The power leaving the port is calculated for each mode in CST, and this can then be calculated at the window by accounting for the decay the signal experiences as it moves from the window. To account for this decay, the cut-off frequencies calculated in CST will be used as this should factor in the various sources of error that will affect the decay of the signal at those modes.

Another issue that arises in calculating the excitation of HOMs is the proper interpretation of CST signals. To calculate the HOM excitations, a sinusoidal signal with frequency of 201.25 MHz was used. It should be noted that the units used in CST are $W^{1/2}$, and this is because the signals are interpreted as the square root of the power. For the TEM mode, such as was used in the simulation of

surface voltages, this has the straightforward relationship between the CST input/output (IO), the voltage (V), and characteristic impedance (Z_0)

$$IO = \sqrt{P} = V/\sqrt{Z_0} \quad (2.2)$$

This relationship should result in IO signals with an amplitude of unity having a voltage amplitude of approximately $\sqrt{1 \text{ W} \times 50 \Omega} = 7.07 \text{ V}$, which is comparable to the voltages observed in Fig 2.3. For the HOM signals however, the relationship to the power is much more complicated.

The TM_{0n} modes are the only modes expected to be excited, so these can be used as an example of how the output signal in CST corresponds to the EM fields of a particular mode. TM modes can be described in terms of the axial component, i.e. E_z , and the subscript of “0” indicates that there is no variation in fields in the azimuthal direction so that the fields can be described as

$$\begin{aligned} \mathbf{E} &= -\frac{jk_z}{k_t^2} \frac{\partial E_z}{\partial r} \hat{r} + E_z \hat{z} \\ \mathbf{H} &= -\frac{j\omega\epsilon}{k_t^2} \frac{\partial E_z}{\partial r} \hat{\phi} \end{aligned} \quad (2.3)$$

where $j = \sqrt{-1}$ and ω is the angular frequency of the signal. The power propagating in the line moves in the axial direction (i.e. \hat{z}), so the power in the line can be found to be

$$\begin{aligned} P &= \oint_S (\mathbf{E} \times \mathbf{H}^*) \cdot \hat{z} dS = \int_{r_i}^{r_o} \int_0^{2\pi} \left(-\frac{jk_z}{k_t^2} \frac{\partial E_z}{\partial r} \right) \left(\frac{j\omega\epsilon}{k_t^2} \frac{\partial E_z^*}{\partial r} \right) r d\phi dr = \\ &= \int_{r_i}^{r_o} \int_0^{2\pi} \frac{k_z \omega \epsilon}{k_t^4} \frac{\partial E_z}{\partial r} \frac{\partial E_z^*}{\partial r} r d\phi dr \end{aligned} \quad (2.4)$$

The axial wavenumber can be expressed as $k_z = \sqrt{k^2 - k_t^2} = j\sqrt{k_t^2 - k^2}$ since the input frequency is below the cut-off, and considering the axial component of the electric field $E_z = E_0(a_n J_m(k_t r) + b_n Y_m(k_t r)) \exp(j(\omega t + k_z z_{port}))$ at the port location z_{port} , the output signal can be described as

$$P = \int_{r_i}^{r_o} \int_0^{2\pi} \frac{k_z \omega \epsilon}{k_t^4} E_0^2 (a_n J'_m(k_t r) + b_n Y'_m(k_t r))^2 \exp(2k_z z_{port}) r d\phi dr \quad (2.5)$$

Finally, considering only the phasor of Eq 2.5, the coefficient E_0 can be solved for a particular but arbitrary set of values of a_n and b_n such that the amplitude of IO is A :

$$E_0 = \frac{Ak_t \exp\left(z_{port} \sqrt{k_t^2 - k^2}\right)}{\sqrt{2\pi\omega\epsilon \sqrt{k_t^2 - k^2} \int_{r_i}^{r_o} \left(a_n J'_m(k_t r) + b_n Y'_m(k_t r)\right)^2 r dr}} \quad (2.6)$$

The application of Eq 2.6 can allow the calculation of the fields due to HOM from the CST output signals. The only remaining factor in establishing the strength of scattered HOM fields is to find the output amplitude A of each mode. A sinusoidal signal is utilized for this purpose as a signal with an amplitude A and phase shift ψ has the valuable property that

$$A \sin(\omega t + \psi) = A \cos(\psi) \sin(\omega t) + A \sin(\psi) \cos(\omega t) \quad (2.7)$$

Since the value of ω is known, a least squares fit can be applied to Eq 2.7 such that it fits [23]

$$O_{mode} = c_{mode}x_1 + d_{mode}x_2, \quad \begin{matrix} c_{mode} = A_{mode} \cos \psi_{mode} & x_1 = \sin(\omega t) \\ d_{mode} = A_{mode} \sin \psi_{mode} & x_2 = \cos(\omega t) \end{matrix} \quad (2.8)$$

where O_{mode} is the output signal of the modes as recorded by CST. The amplitude is then found to be

$$A_{mode} = \sqrt{c_{mode}^2 + d_{mode}^2} \quad (2.9)$$

This applies to all modes, and so it was applied to the all of the signals of the HOMs, and the decay was taken into account so that the power of each scattered mode at the window is calculated. As expected, only the TM_{0n} modes had any significant amplitude, but even this amplitude is very small. The scattering of HOMs is quite small and negligible for most applications, but this does add to the EM stress on the window as has already been discussed in the previous subsection. This could also factor into the multipactor phenomenon discussed in the following chapters, so its role should be considered there as well. The values for scattered power in the TM_{01} and TM_{02} modes, as well as the signal phase relative to the TEM mode, are shown in Table 2.2.

The scattering was considered for both forward propagating, i.e. from the air to vacuum conditions, and for backward propagating waves with no difference in the scattering from either direction. The window was also modified to be thicker to see how this affects HOM scattering, with the thickness of the window (i.e. in the axial direction) was changed from 0.885 in. to 1.205 in for one

Table 2.2: Amplitudes and phases of the TM_{0n} modes scattered by the RF window for forward power of the current geometry, a window without a vacuum-side notch, and a window of increased thickness, and for backward power incident on the current window design.

Case	$A_{TM_{01}} (\times 10^{-5})$	$\psi_{TM_{01}} - \psi_{TEM} (^{\circ})$	$A_{TM_{02}} (\times 10^{-4})$	$\psi_{TM_{02}} - \psi_{TEM} (^{\circ})$
Forward power excitation	5.1996	174.3	1.9328	-3.261
Backward power excitation	4.9768	-51.88	1.8587	125.6
No vacuum notch	1.8102	165.8	1.1776	-6.217
Thick window	8.6389	175.6	3.4887	-0.2985

modification, and the notch in the air side eliminated for the other. There is not a significant difference between the strength of the scattered HOM fields from the forward and backward traveling signals, but the window modifications do have an appreciable effect. The removal of the notch in the vacuum side reduced the electric field strength in the region of the window within the inner conductor, and thus the strength of the scattered HOMs was also reduced. The region where the conductor radii are modified to match the impedance at the window with the rest of the line essentially acts as a resonator with a small quality factor (discussed in detail for the highly resonant cavity in the next section), and so by increasing the window thickness, the resonant frequencies will be brought lower and the strength of the scattered HOMs increases. This is a heuristic explanation of that increase shown in Fig 2.4, but it is apparent that there are more factors that go into the scattering of HOM than this alone.

The ability of the HOM amplitudes to describe the EM fields should also be verified. To that end, the electric field was monitored and its radial and axial components were found along a curve ranging between the conductors at the axial location of the window vacuum surface at a time near the peak of the input TEM mode. These measurements are then compared with the fields predicted by adding the TM_{01} and TM_{02} modes as tabulated from Table 2.2 to the TEM mode, and this is shown in Fig 2.5. The disagreement between the recorded and the predicted fields is quite significant. A similar comparison was made to the HOM fields at the port as calculated by CST to validate the interpretation of CST results and the calculation of the fields, and that comparison showed that the calculations were

sound. The disagreement observed in Fig 2.5 can be better explained by the use of only two HOMs.

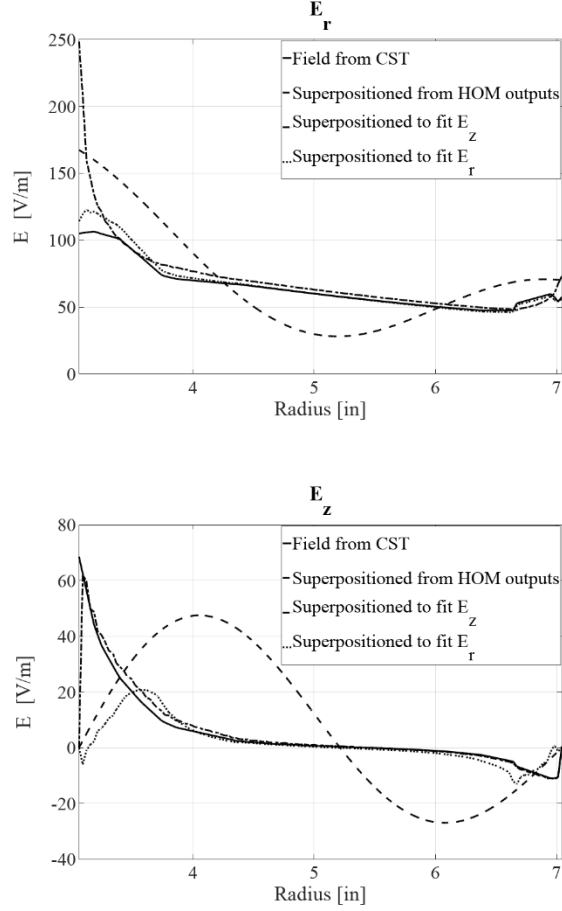


Figure 2.5: Electric field of the radial (E_r) and axial (E_z) components. The fields were calculated in CST and compared to the fields calculated from the superposition of the TM_{01} and TM_{02} amplitudes given in Table 2.1. The fit of all TM_{0n} modes from $0 \leq n \leq 100$ to both the radial and axial components is also shown in both parts of the figure.

More HOMs can be considered and then fitted directly to the field values to better understand how HOMs are scattered from the window. To do this, the axial and radial components were calculated for the first 100 TM_{0n} modes with the recognition that a superposition of these modes can be fitted to the values calculated by CST. The magnitude of the original modes is somewhat arbitrary, so the values of a_n and b_n were set such that the maximum value of the axial component of each mode was one.

Then the coefficients by which each mode could be multiplied to best fit the calculated values in CST (c_n) were found by using a least squares method such that

$$\sum_{m=1}^{100} (E_{z,CST}(r_m) - c_n E_{z,n}(r_m)) E_{z,n} = 0, 1 \leq n \leq 100 \quad (2.10)$$

where $E_{z,CST}$ is the axial field value calculated in CST, and $E_{z,n}$ is the axial field value of a particular mode. The coefficients c_n can be solved to satisfy Eq 2.10 for both the axial fields and the radial fields, although the radial fields must also take into account the TEM mode. In order to ensure that the consideration of the decay of the HOMs is accurate, the fields were also recorded for a curve placed at 0.25 and 0.5 in from the window surface, and the least squares fit was applied to each individual curve as well as all the curves together, with all resulting in similar values for the coefficients. The results for fitting the fields over all considered axial positions are also shown in Fig 2.5.

The fitting of the curves to the fields is more accurate than the use of only the two HOM modes found from the port calculations. The fitting of the HOMs to either the radial fields or the axial fields were not highly consistent with the other, indicating that the attempt to describe modes solely in terms of scattered HOMs will be incomplete as there are many factors that can influence results. Further, the amplitudes of the HOMs indicates that TM_{0n} modes are the only modes that need be considered to be excited by the window. Any consideration of the HOMs in regards to the EM stress should be done by recording fields and voltages directly from the results, as calculated results have been shown to be inaccurate. However, the use of HOMs to describe fields might be sufficient in multipactor (MP) analysis as discussed in chapter four.

Overall, the HOMs are unlikely to be a source of failures themselves, but they are worth considering due to the complex and inexplicable nature of window failures. While the strength of the excited HOMs will not be sufficient to cause the window to fail directly, they can change the stress that is placed on the window, and given other factors they could contribute to window failure. This might make it seem as though HOMs should only be minimized, but their presence could also help to inhibit the multipactor phenomenon. The effect of HOMs on multipactor will be examined in chapter

4, and this aspect of HOM scattering will be discussed in conjunction with the EM stresses caused by them in the conclusions.

2.3: Effect of accelerating cavity

The addition of the accelerating cavity to the coupler greatly complicates the fields near the RF window, both in the real world and the simulation of the system. While the fields in only a small portion of the cavity will be able to affect the fields in the coupler, small abnormalities in the cavity can drastically alter the cavity fields, and thus coupler fields, making the above analysis incomplete. The accuracy of the EM analysis therefore requires simulation of the whole system of the coupler and the accelerator cavity, but the physics of establishing cavity fields can make those simulations tedious and untenably long. Therefore an approach to analyzing the whole coupler and cavity accelerator system needs to be established before a more detailed analysis of the EM environment of the window can be made.

2.3.1: Q-factor and simulations

The problem in simulating the accelerator system arises from both the establishment of fields in a high quality factor (Q-factor) structure and the limitations of numerical methods [16] [24] [25]. High-Q structures ($Q > \sim 10000$) require a long time to establish the steady state environment [21], so the simulation will require millions of time steps to reach steady state [24]. While this of itself is not excessive, the system is also electrically large with dimensions on the order of multiple wavelengths, thereby generating millions of mesh cells, and the complexity that is added by the detailed geometry also requires more computational power. All these factors result in a need to change how the accelerator system is simulated from the coupler alone.

The Q-factor is a representation of how well a resonator stores energy, and consequentially, how long it takes a system to establish steady state. There are two definitions of the Q-factor, with the first being that it is a ratio of the energy stored in the system to the energy lost per cycle, or

$$Q = 2\pi \frac{U_{system}}{U_{loss/cycle}} = 2\pi f \frac{U_{system}}{P_{loss}} \quad (2.11)$$

where U denotes energy, P denotes power, and f denotes frequency. The power losses that are associated with the accelerator system in these simulations are due to the finite conductivity of the copper surfaces and the emission of fields from the cavity back into the coupler via the coupling aperture. The latter of these is the dominant factor when the fields are being established, so during that time very little energy is deposited into the cavity with each cycle. This results in a number of cycles that is on the same order as the Q -factor to establish the steady state cavity fields.

The number of cycles required in the simulation is compounded by the constraints of the numerical methods. The grid spacing used in the finite difference time domain (FDTD) method is required to be at most $\lambda/10$, but will need to be closer to $\lambda/20$ for the simulation to be accurate [26]. This alone would place the number of grid points at only $\sim 10^5$, but the geometry of the system requires this number to be much higher as the curves and features such as drift tubes will require smaller cells than what is required for the numerical approximations. In addition to the size of the mesh cells, the time step used will also limit the ability to simulate the accelerator system, and in order for a stable solution to be reached, the time step must follow

$$\Delta t \leq \frac{1}{c} \left[\left(\frac{1}{\Delta x} \right)^2 + \left(\frac{1}{\Delta y} \right)^2 + \left(\frac{1}{\Delta z} \right)^2 \right]^{-1/2} \quad (2.12)$$

where Δx , Δy , and Δz are the minimum grid spacings in the simulation, c_0 is the speed of light, and Δt is the time step [24]. As discussed, the minimum grid spacing will also be well below the minimum of $\lambda/20$ required for stability due to the curvilinear surfaces of the accelerator cavity and coupler, and thus the time step will also be greatly reduced. This in combination with the long times required to reach steady state for a high- Q structure results in simulation times that are too long to use in this analysis.

Given all of these factors, a straightforward simulation of the accelerator system is impractical. The actual fill time for the accelerator tanks at LANSCE is approximately 200 μs whereas the time step

that is used by CST is on the order of 1 to 10 ps, and the number of mesh cells is around 2 to 3 million. Attempts at these computations were made, but the time to get to steady state required weeks to run, with no ability to pause simulations. This resulted in some runs being interrupted, so they had to be restarted. Additionally, any investigation into the effects of changing the geometry or other factors that affect the simulations would require running the simulations again. The frequency domain solver could potentially avoid these issues, but much of the interest in the interaction between the coupler and the cavity is to know how the transient fields in the cavity affect window performance, and that would be lost in the frequency domain. Given these factors, a new method had to be utilized within the framework of the CST.

2.3.2: Quick fill method

A simple solution was found in the linear relationship between the input power and the stored energy in the cavity. To fill the cavity in the $\sim 200 \mu\text{s}$ of simulation time that is necessary without alterations, a signal with a constant, nominal amplitude would be used, so this signal will be referred to as the “long fill.” The amplitude that will be used for much of this work will be $1 \text{ W}^{1/2}$, with the unit of $\text{W}^{1/2}$ coming from the interpretation of the input signal by CST as discussed in the previous section. But since the energy stored in the cavity is directly proportional to the amplitude of the input signal, a larger signal could be used at the beginning of the fill signal to more quickly reach steady state. A simple way to do this is to have a signal with three regions: 1) A constant amplitude of P_0 from time 0 to time t_1 , 2) a linearly decreasing amplitude from P_0 to the amplitude of the long fill, i.e. $1 \text{ W}^{1/2}$ from time t_1 to time t_2 , and 3) a constant amplitude signal equivalent to the long fill amplitude from time t_2 until the end of the simulation time. Additionally, a fourth region of the input signal can also be used where the input is cut-off and the emissions from the cavity alone are continued. An illustrative example is shown in Fig 2.6 for context.

This “quick fill” signal should allow us to examine both the transient and steady state properties of the EM fields. The selection of the times t_1 and t_2 will be somewhat arbitrary, but can be orders of

magnitude less than the fill time of $\sim 200 \mu\text{s}$. The only requirement will be that they should have a sufficiently high number of RF periods as discussed later. If the steady state is reached, then all of the fields near the window can be found. Additionally, the transient signal is still present, so minimal work is needed to reconstruct the effects of the transient fill on the window.

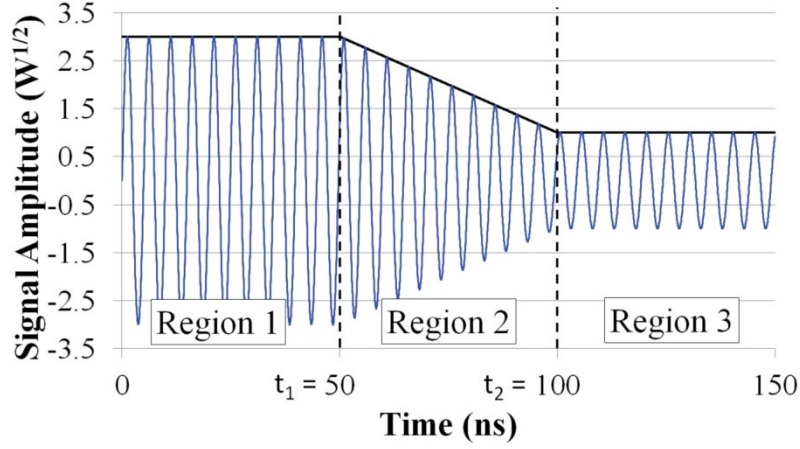


Figure 2.6: Example of the signal used to quickly fill the cavity, reproduced courtesy of The Electromagnetics Academy.

In order to implement this method, the establishment of cavity fields in response to the input signal must be discussed. The cavity fields will be discussed in terms of the vector potential $\mathbf{A}(\mathbf{r}, t)$ in keeping with the approach of Wangler [16], but the use of either the electric or magnetic field will yield the same results. Faraday's Law, Maxwell-Ampere's Law, and the definition of the vector potential can then be combined to get

$$\nabla^2 \mathbf{A}(\mathbf{r}, t) - \frac{1}{c_0^2} \frac{\partial^2 \mathbf{A}(\mathbf{r}, t)}{\partial t^2} = -\mu_0 \mathbf{J}(\mathbf{r}, t) \quad (2.13)$$

where $\mathbf{J}(\mathbf{r}, t)$ is the current density that the driving signal generates within the coupling aperture, and μ_0 is the magnetic permeability of free space. The cavity fields consist of number of independent modes that are dependent only on the geometry of the cavity, so the time and spatial components of each mode can be separated. This leaves the definition of the vector potential to be

$$\mathbf{A}(\mathbf{r}, t) = \sum \xi_m(t) \mathbf{A}_m(\mathbf{r}) \quad (2.14)$$

where ξ_m is the time-dependent portion of a particular mode acting as the magnitude of the spatially-dependent portion \mathbf{A}_m .

The current density \mathbf{J} in Eq. 3 must also be addressed in terms of both physical meaning and the relationship to the interpretation of input signals in CST. Similar to the vector potential, \mathbf{J} can also be separated into time and space components so that $\mathbf{J}(\mathbf{r}, t) = f(t) \mathbf{J}_{ca}(\mathbf{r})$, where the subscript “ca” indicates that the spatial component is due to the coupling aperture. The time component is related to the input signal in CST. Because of this, the time component of the current density can be directly proportional to the input signal P_{in} such that $\mathbf{J}(\mathbf{r}, t) = P_{in} \mathbf{J}_{ca}(\mathbf{r})$, where the term \mathbf{J}_{ca} has absorbed any arbitrary multipliers that make the relationship between P_{in} and \mathbf{J} exact.

The properties of the vector potential and the Q-factor can now be applied to Eq. 2.3 to get the resonance equation that will allow for the development of the quick fill signal. Each individual mode that contributes to the vector potential has the properties that it 1) satisfies the Helmholtz equation, and 2) is therefore orthogonal to all other modes (i.e. $\int \mathbf{A}_m \cdot \mathbf{A}_n dV = 0$ unless $m = n$). The satisfaction of the Helmholtz equation allows Eq 2.3 to be written as

$$\sum_n \left(-\frac{\omega_m^2}{c_0^2} \xi_m \mathbf{A}_m - \frac{1}{c_0^2} \ddot{\xi}_m \mathbf{A}_m \right) = -\mu_0 P_{in} \mathbf{J}_{ca}(\mathbf{r}) \quad (2.15)$$

assuming a harmonic response of the mode at an angular frequency of ω_m . An additional term should also be added to Eq. 2.5 to account for field energy lost due to both the ohmic losses in the cavity walls and the emission of fields back through the coupler aperture. The Q-factor accounts for both of these losses, so it can be incorporated into a damping term proportional to $\dot{\xi}_m$. The overall result can be multiplied by \mathbf{A}_m and integrated over the volume to take advantage of the orthogonality and get

$$\ddot{\xi}_m + \frac{\omega_m}{Q_m} \dot{\xi}_m + \omega_m^2 \xi_m = P_{in} \frac{\int \mathbf{J}_{ca}(\mathbf{r}) \cdot \mathbf{A}_m(\mathbf{r}) dV}{\epsilon_0 \int \mathbf{A}_m^2(\mathbf{r}) dV} = P_{in} K \quad (2.16)$$

The above resonance equation is tantamount to being able to develop a quick fill signal, and thus analyze the EM fields near the window. The expression ξ_m is a direct predictor of the amount of

energy in the accelerator cavity and, given a constant amplitude sinusoidal input, will approach a constant amplitude as steady state is reached. The exact value of ξ_m is not important as long as the amplitude is nearly constant at steady state. The right hand side of Eq. 2.6 represents the driving component whereby fields are established in the cavity by the input signal. The constant K will not affect the behavior of ξ_m and so will be ignored, but it is a representation of the effectiveness of the coupling between the transmission line and the cavity.

The parameters ω_m and Q_m in Eq 2.6 are unique to each mode and can be found using the S-parameter that is readily calculated in CST. The S-parameter is a measure of the scattering of input signals across, typically, multiple ports. But the accelerator system being simulated has only one port, so the S-parameter (S_{11} in this case) is simply a ratio between the reflected and input signals [21]. Many modes can be simultaneously excited by using a Gaussian pulse containing a range of frequencies, and this excitation will inhibit the reflection of the signal at the specific frequencies of each mode, thus resulting in dips in the S-parameter. The spread of these dips can then be used to get the Q-factor using a second definition where

$$Q = \frac{\omega_m}{\Delta\omega_m} \quad (2.17)$$

with $\Delta\omega$ being the full-width, half-max of the S-parameter dip [21]. The use of the S-parameter to find these values is demonstrated in Fig 2.7. The calculation of the S-parameter over the range of frequencies is performed automatically by CST using Fourier transforms.

Once the mode parameters are known, the parameters for use in the quick fill signal can be defined and calculated. The input power has a generic form of $P_{in} = (m_r t + p_r)\sin(\omega t)$ resulting in the general solution of Eq 2.6 being

$$\begin{aligned} \xi_{m,i}(t) = & (a_i \cos(\gamma t) + b_i \sin(\gamma t)) \exp\left(-\frac{\omega_m}{2Q_m} t\right) + (c_{1,i} t + c_{2,i}) \cos(\omega t) + (c_{3,i} t + \\ & c_{4,i}) \sin(\omega t), \gamma_m = \omega_m \sqrt{\frac{2Q_m-1}{2Q_m}} \end{aligned} \quad (2.18)$$

where a , b , and c are constants, t is time, γ_m is a deviation from the resonant frequency to satisfy Eq.

2.16, and i denotes the region of the input signal as discussed above. There are two parts to the solution of ξ_m , the homogeneous solution $(a_i \cos(\gamma t) + b_i \sin(\gamma t)) \exp\left(-\frac{\omega_m}{2Q_m} t\right)$, which when applied to the left hand side of Eq 2.6 yields zero, and the particular solution $(c_{1,i}t + c_{2,i}) \cos(\omega t) + (c_{3,i}t + c_{4,i}) \sin(\omega t)$, which is equivalent to P_{in} when applied to Eq 2.6. The coefficients of the particular solution can then be found by solving the equation

$$\begin{bmatrix} \omega_m^2 - \omega^2 & 0 & \omega_m \omega / Q_m & 0 \\ \omega_m / Q_m & \omega_m^2 - \omega^2 & 2\omega & \omega_m \omega / Q_m \\ -\omega_m \omega / Q_m & 0 & \omega_m^2 - \omega^2 & 0 \\ -2\omega & -\omega_m \omega / Q_m & \omega_m / Q_m & \omega_m^2 - \omega^2 \end{bmatrix} \begin{pmatrix} c_{1,i} \\ c_{2,i} \\ c_{3,i} \\ c_{4,i} \end{pmatrix} = \begin{pmatrix} 0 \\ 0 \\ m_i \\ p_{r,i} \end{pmatrix} \quad (2.19)$$

The coefficients m_i and $p_{r,i}$ correspond to the values of the input signal such that

$$m = \begin{cases} 0 \\ \frac{1-P_0}{t_2-t_1} \\ 0 \end{cases}, p_r = \begin{cases} P_0 \\ \frac{t_2 P_0 - t_1}{t_2 - t_1} \\ 1 \end{cases} \text{ for } \begin{cases} t < t_1 \\ t_1 \leq t < t_2 \\ t \geq t_2 \end{cases} \quad (2.20)$$

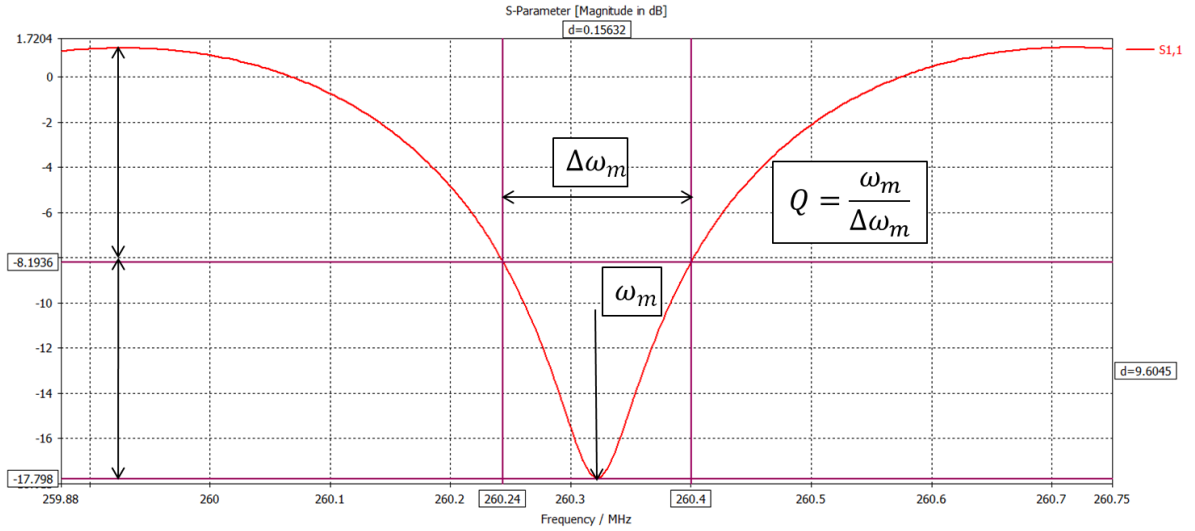


Figure 2.7: Sample S-parameter calculated by CST. Due to errors in using a finite series, the values surrounding the resonance frequency will be greater than one (zero in dB), so the value $\Delta\omega_m$ is based at the midpoint between the maximum and minimum values immediately surrounding the resonance frequency.

Once the coefficients of the particular solution are found, the homogeneous coefficients can

also be determined. While the solution to the particular coefficients only depends on the driving signal, the homogeneous coefficients require initial conditions for their solution. Initially, there are no fields present in the cavity and no signal working to establish fields in the cavity, so $\xi_m(0) = 0$ and $\xi'_m(0) = 0$. For subsequent regions, the initial conditions will be the previous regions so that the homogeneous coefficients are found by solving

$$\begin{aligned} & \begin{bmatrix} \cos(\gamma t) & \sin(\gamma t) \\ -\frac{\omega_m}{2Q_m} \cos(\gamma t) - \gamma \sin(\gamma t) & \gamma \cos(\gamma t) - \frac{\omega_m}{2Q_m} \sin(\gamma t) \end{bmatrix} \begin{pmatrix} a_i \\ b_i \end{pmatrix} \exp\left(-\frac{\omega_m}{Q_m} t\right) = \begin{pmatrix} \xi_{m,i} \\ \xi'_{m,i} \end{pmatrix} - \\ & \begin{pmatrix} (c_{1,i}t + c_{2,i}) \cos(\omega t) + (c_{3,i}t + c_{4,i}) \sin(\omega t) \\ (c_{3,i}\omega t + c_{1,i} + c_{4,i}\omega) \cos(\omega t) - (c_{1,i}\omega t + c_{2,i}\omega - c_{3,i}) \sin(\omega t) \end{pmatrix} \end{aligned} \quad (2.21)$$

The nominal long fill signal has a constant amplitude so that $m = 0$ and $P_{in} = 1$. By solving for the coefficients in Eq 2.9 and 2.11, the response to the long fill is found to be

$$\xi_m(t) = \frac{1}{2\omega} \left(\frac{2Q_m}{\omega_m} \cos(\gamma t) + \frac{1}{\gamma} \sin(\gamma t) \right) \exp\left(-\frac{\omega_m}{2Q_m} t\right) - \frac{Q_m}{\omega_m \omega} \cos(\omega t) \quad (2.22)$$

At steady state, the homogeneous solution becomes negligible, and the amplitude of ξ_m becomes $Q_m/\omega_m \omega$.

The amplitude of the input signal in region one (P_0) can then be found using the secant method [27] to adjust the cavity response in the region three where steady state is supposed to be achieved. Since the goal of this approach is to reduce the simulation time, the times t_1 and t_2 should be selected to be much less than the fill time of the long fill signal ($\sim 200 \mu s$). However, the selection of times must also allow for the fields to travel throughout the cavity so as to avoid spurious results due to reflections that have not been fully resolved (more on this later). Once the times are set, the change in the amplitude during the steady state region is used to calculate the value of P_0 .

First the peaks in the steady state region have to be found. Since $m_i = 0$ during steady state, the only particular coefficient that will be non-zero according to Eq 2.9 is c_2 . If steady state is reached in region three (Fig 2.6), the times where the cavity response ξ_m is equal to the amplitude can be found analytically, but since the value of P_0 required to reach steady state is unknown, a large number of

points is instead scanned to find the peaks. Once this occurs, the least squares method is applied to find the linear approximation of the response amplitude over time because the slope of the amplitude ($\overline{d\xi}$) will indicate how the value of P_0 should be adjusted.

The slope of the response amplitude can then be applied to the secant method to quickly calculate the correct value of P_0 to reach steady state. The secant method is an iterative process for calculating the zeros of a complex functions, which in this case are the values of P_0 and the slope of the response amplitude. This method assumes a linear relationship between any two iterations, so that the value of the independent variable that results in the zero of the function is calculated from the linear relationship of the two most recent iterations. Steady state has been reached if the net change in the amplitude ($\overline{d\xi}$) is zero across region 3, so this is the function of the independent variable of initial power P_0 . The iterative relationship between these variables is then expressed as

$$P_0^i = P_0^{i-1} - \overline{d\xi}^{i-1} \frac{P_0^{i-1} - P_0^{i-2}}{\overline{d\xi}^{i-1} - \overline{d\xi}^{i-2}} \quad (2.23)$$

with i being the number of the iterations. This method requires two initial guesses for the values of P_0 , which can also affect how quickly their values will converge, but this is not a significant issue in this application.

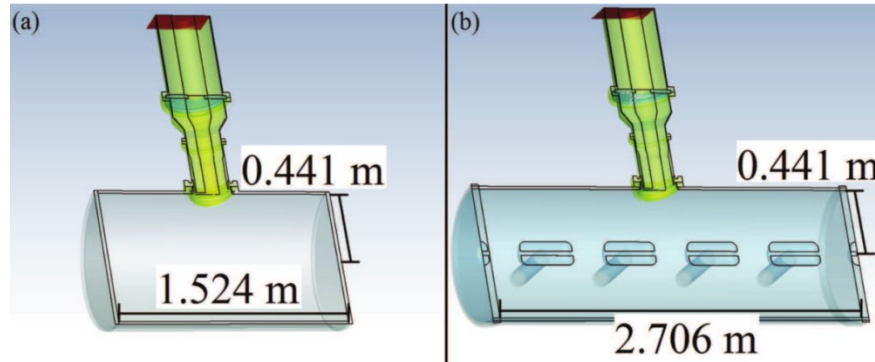


Figure 2.8: Geometries of the sample cavities used to establish the quick fill method. (a) contains no drift tubes but can have PEC or copper cavity walls, and (b) has four drift tubes added with only PEC used for the cavity, reproduced courtesy of The Electromagnetics Academy.

Before applying this to the simulation of the DTL, three test cases were used to ensure the accuracy of applying the quick fill signal to simulate the transient response of a coupler-cavity system. For these cases, the exact measurements of the coupler and window geometries of the DTL at LANSCE were used while the cavity geometry was changed to be both smaller and of a lower Q-factor. The first test case (A) is a cavity with no drift tubes and made of a perfect electric conductor (PEC). This case allows for the modes of the cavity to be found analytically for comparison to the CST results, and the use of the PEC material means that the only losses are due to the emission of energy from the cavity. Test case B uses the same geometry as (A), but the material is replaced with copper to introduce the effects of ohmic losses. Test case C is an axial truncation of the DTL cavity with drift tubes, but the cavity material is changed to PEC. The schematics of these test cases is seen in Fig 2.8. The radii of all cavities were kept to be the same radius as the DTL, and the length of the empty cavities (Cases A and B) were made to be on the order of one wavelength at DTL's operating frequency of 201.25 MHz. The length of Case C was set to fit four drift tubes (2.706 m), with two on either side of the coupler aperture.

The cavity parameters ω_m and Q_m must first be found for Case A. While the coupler aperture will affect the resonance frequency slightly, calculating them analytically provides a useful benchmark to tell not only how accurate the results from the S-parameter are, but also what modes the S-parameter peaks represent. The resonance frequencies can be found from the relationship to the wavenumbers of the radial and axial components, k_ρ and k_z respectively: [21]

$$k_m^2 = \left(\frac{\omega_m}{c_0}\right)^2 = k_\rho^2 + k_z^2 \quad (2.24)$$

The wavenumbers are found by solving the Helmholtz Equation in cylindrical coordinates for the axial component of either the electric field (resulting in TM modes) or the magnetic field (TE modes). For the TM modes, E_z must be zero on the cylindrical walls and a derivative of $\frac{\partial E_z}{\partial z} = 0$ at the end walls, and for the TE modes, B_z is zero on the end walls with a derivative of $\frac{\partial B_z}{\partial r} = 0$ at the cylindrical walls.

The wavenumbers can then be found to be

$$k_z = \frac{p\pi}{h}, J_m(k_\rho r_c) = 0, TM \text{ modes} \quad (2.25)$$

$$J'_m(k_\rho r_c) = 0, TE \text{ modes}$$

with J_m being the Bessel function of the first kind with an order of $m = 0, 1, 2, \dots$ and n zeros of J_m or J'_m between the centerline and outer radius. The variable p is a positive integer value, with the TM mode allowing $p = 0$, and h and r_c are the cavity length and radius respectively. Solving these parameters for the geometry of test case A results in the values shown in Table 2.3.

Table 2.3: Modes in frequency range of 200 MHz to 350 MHz of simple cavity used for investigating quick fill method.

Type	m	n	p	$\frac{k_\rho}{r}$	f (MHz)
TM	0	1	0	2.404826	260.30
TM	0	1	1	2.404826	278.26
TE	1	1	1	1.841184	222.24
TM	0	1	2	2.404826	326.27
TE	2	1	1	3.054237	344.91
TE	1	1	2	1.841184	280.02

Table 2.4: Simulation parameters of quick fill test cases.

Case	f_m (MHz)	Q_m	P_0 (W ^{-1/2})	t_1 (ns)	t_2 (ns)
A(i)	260.322	16650	2.44	50	1950
A(ii)	260.322	16650	4.55	250	750
A(iii)	260.322	16650	2.54	500	1500
B(i)	260.322	16450	5.86	500	1500
B(ii)	222.855	45700	7.00	500	1500
C(i)	215.489	30220	9.41	2500	7500
C(ii)	215.489	66370	20.14	2500	7500

The S-parameters of cases A and B can be seen in Fig 2.9. The frequencies of the peaks for case A match closely with the predicted results of Table 2.1, with small variations that would be predicted by perturbation theory. The TM₀₁₀ mode is analogous to the mode that the DTL operates at, so the corresponding frequency of 260.32 MHz was selected for analysis, and the values of ω_m , Q_m , P_0 , and t_1 and t_2 for all the cases can be found in Table 2.4. The time t_2 was selected to be an order of magnitude less than the fill time ($\sim 2Q_m/\omega_m$) to both greatly decrease simulation time and also allow

time for any transient artifacts to be cleared from the results.

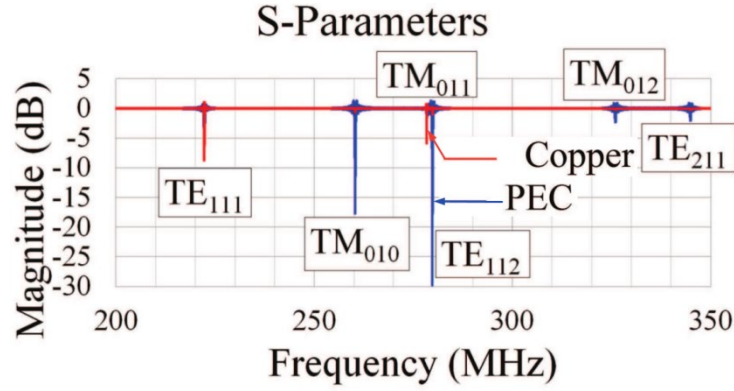


Figure 2.9: S-parameters for the truncated cavities made of PEC and copper. Various cavity modes are labeled at their frequency, reproduced courtesy of The Electromagnetics Academy.

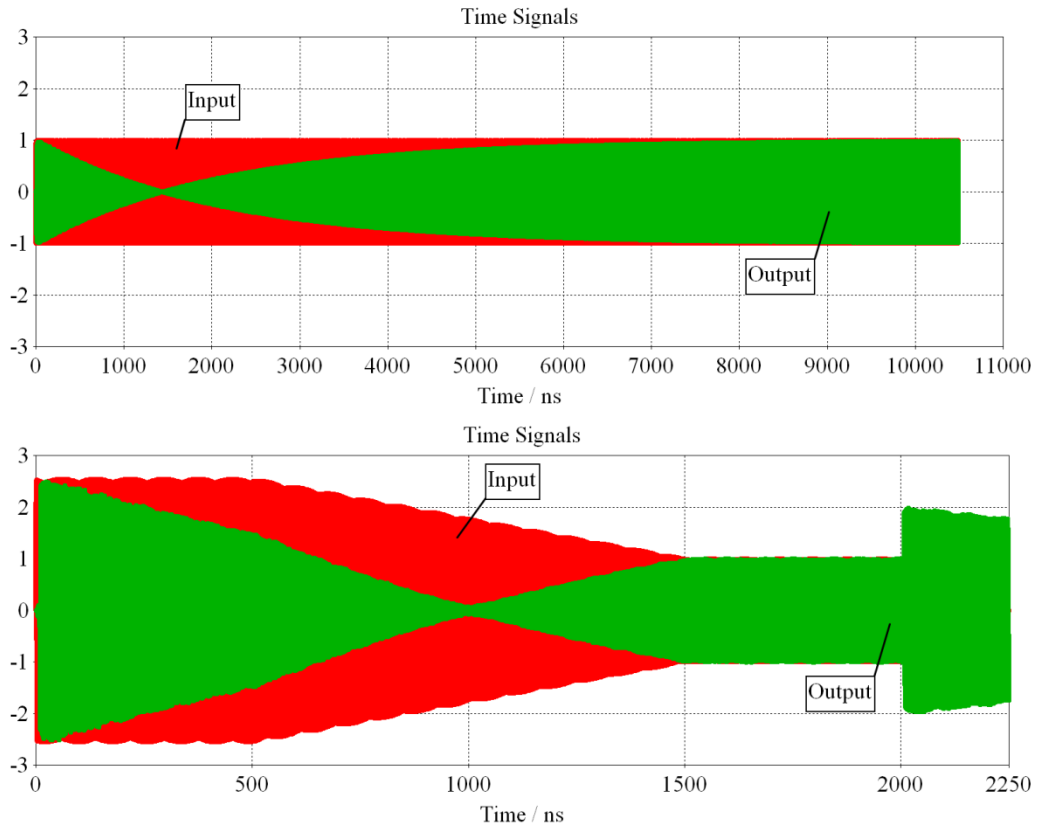


Figure 2.10: Input and output signals of the truncated PEC cavity. The top part is for the constant amplitude input, and the bottom portion is for the quick fill input, reproduced courtesy of The Electromagnetics Academy.

Case A was first run with the long fill signal to illustrate how the cavity is filled under standard conditions and provide a benchmark for the quick fill signal. First, the magnitude of the output signal should be equal to the magnitude of the input at steady state since the lack of ohmic losses means that emissions through the aperture are the only means by which the cavity loses energy. This is evidently the case seen in the input/output (I/O) signals shown in Fig 2.10. The energy in the system as calculated by CST also shows steady state to have been reached since there is only a loss of 0.2% of the maximum energy across the time steady state was analyzed.

While the I/O signals in Fig 2.10 show when steady state is reached in the two methods, it is also important that the fields in the coupler during steady state are consistent between the quick fill and long fill methods. Voltage and current monitors were created in CST to benchmark the consistency of the electric and magnetic fields respectively between various fill signals. The placement of these monitors is shown in Fig 2.11, and it should be noted that this is not a precise analysis of the fields, but rather a general indicator of consistency. These monitors were selected because they reduce the number of data points that need to be compared between signals used, and a more in depth discussion of the full field analysis will be made when the actual DTL is analyzed. The agreement between all the signals used in Case A indicate that the use of quick fill signals does give consistent results with the long fill case, as seen in Fig 2.12, where the minimum and maximum of the voltage monitors across the steady state regions are shown.

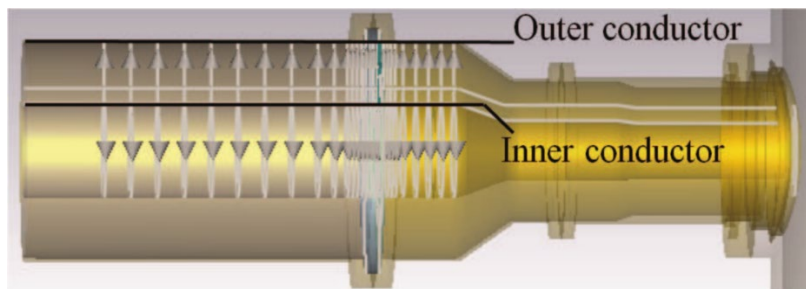


Figure 2.11: Locations of the current and voltage monitors in the coupler. The inner and outer conductors are labeled for clarity, reproduced courtesy of The Electromagnetics Academy.

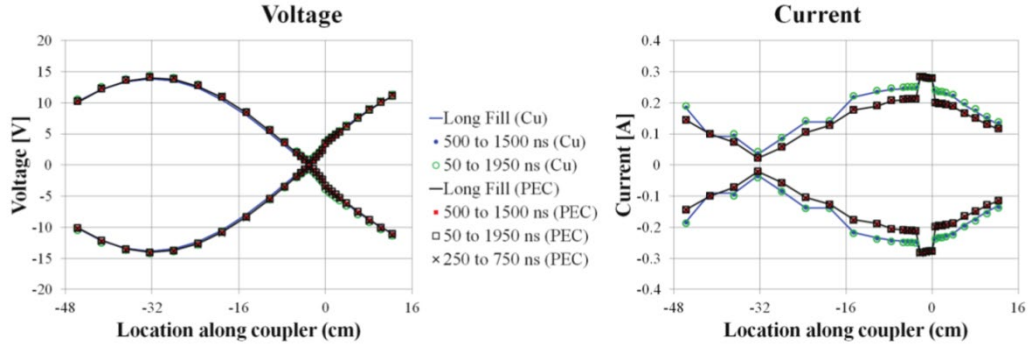


Figure 2.12: Voltage and current monitors across the coupler length for all the test cases used to investigate the quick fill method, reproduced courtesy of The Electromagnetics Academy.

Since Case A showed the quick fill method to be a legitimate way to decrease simulation times, the effect of ohmic losses should be discussed by considering Case B. The S-parameters shown in Fig 2.9 give similar resonance frequencies for Case B as Case A, but the intensity of the S-parameter peaks are very different between the two cases. This is not unexpected as the Q-factor will change non-uniformly across modes with the introduction of ohmic losses, but the TM_{010} mode has considerably less intense peak in the S-parameter than it did in Case A, so the intense TE_{111} peak was also analyzed.

The analysis of the TE_{111} mode showed the quick fill method to be accurate. The I/O signals are shown in Fig. 2.13, and the output signal strength of both the long fill and quick fill signals had a magnitude of $\approx 0.96 W^{1/2}$. This indicates that the steady state has been reached because the magnitudes are the same for both the long and quick fills. This can also be indicated by the energy loss of the system throughout steady state, with only about 0.917% of the maximum energy lost over this time.

Similarly, the TM_{010} mode was consistent between long and quick fill signals. The voltage and current monitors for this case is shown alongside those of Case A in Fig 2.12. There is no discernable difference between the voltage monitors, but the current monitors are increased from the PEC case due to the introduction of resistance in the power-current-voltage relationship. It should also be noted that there is an abrupt change in both the current and voltage profiles near 0 cm. This is the location of the

RF window, so the dielectric constant of Rexolite ($\epsilon_r = 2.53$) affected these values.

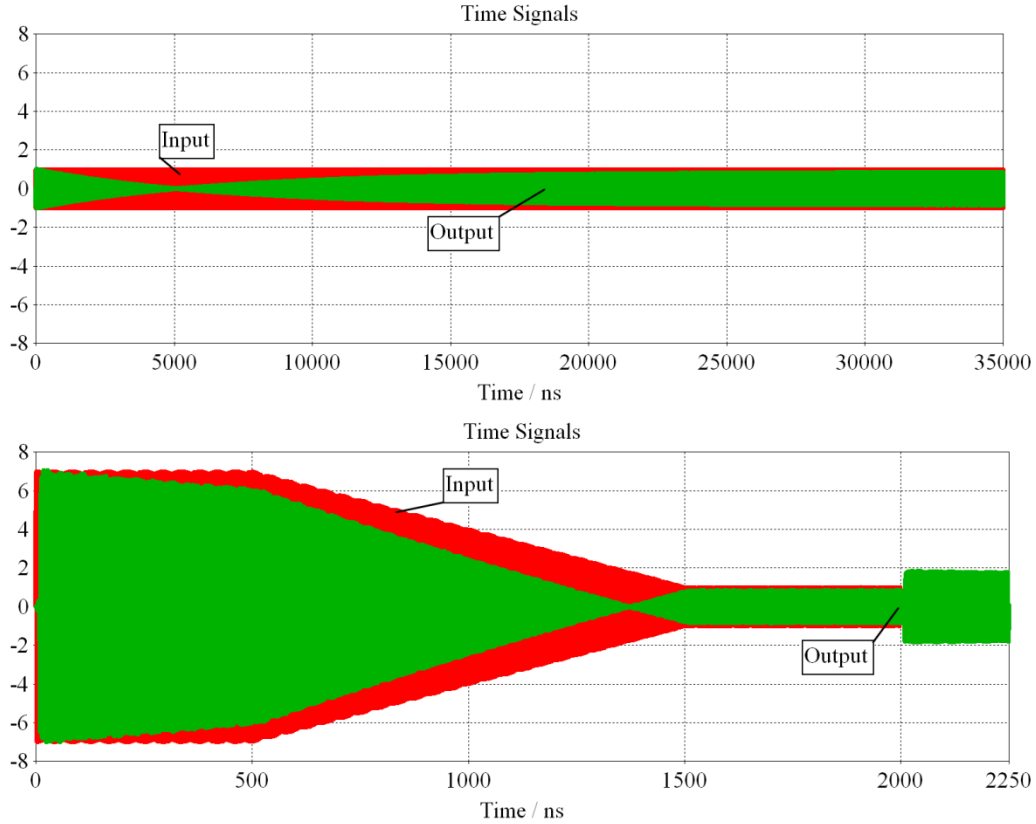


Figure 2.13: Input and output signals of the truncated copper cavity. The top part is for the constant amplitude input, and the bottom portion is for the quick fill input, reproduced courtesy of The Electromagnetics Academy.

The geometry of Tank 4 at LANSCE was truncated for use as test case C. The exact length of the cavity was decided on by placing the end caps at the location of the third drift tube on either side of the coupler. Evidence of this can be seen in Fig 2.8b as outlines of the drift tubes in the end caps, but this will not affect results. Because the TM_{010} peak was much weaker for the copper walls in the previous case, PEC was selected to be the material for Case C, allowing for a more intense S-parameter peak from which the Q-factor can be calculated. The use of PEC also means that the only losses are emissive, so the output signal should be equal to the input at steady state and can be used to ensure

steady state was reached without performing the long fill, which was predicted to take $\sim 400 \mu\text{s}$.

When the quick fill was applied to this case (see row C(i) in Table 2.4), however, steady state was not reached. Instead of being equal, the amplitude of the output signal was only 10% that of the input, indicating that the Q-factor must have been underestimated. A concern with using the S-parameter to estimate the Q-factor is that the S-parameter can be affected by the length of the simulation because accurate S-parameter calculation requires that the resonant modes excited by the input signal have sufficiently decayed. If the Q-factor for case C is much higher than what was calculated, as the results suggested, then it would be expected that the S-parameter simulation would need to be run much longer than it was ($50 \mu\text{s}$) for accurate results to be obtained. The previous test cases worked because they had Q-factors of 16650 and 16450 (cases A and B respectively, see Table 2.4), which are considerably less—and thus require less time for accurate S-parameter calculation—than the Q-factor 30220 that was calculated for test case C, which itself was too low. The S-parameter calculations must be carried out even when the resonant frequency of a system is known, such as with the DTL, because the simulation model can deviate from that frequency slightly, but the use of these simulations to calculate the Q-factor requires the simulations to be unfeasibly long. Considering this, an alternative method to calculating the Q-factor was used.

The new method to calculate the Q-factor is found by using its original definition in Eq 2.1 and rearranging it to the differential equation $Q_m = -\frac{\omega_m U}{2U'}$ where the negative sign arises to denote the loss of power, and the factor of 2 arises from the fact that the power loss in Eq 2.1 is averaged. The solution to this equation is the simple exponential relation

$$U = C \exp\left(-\frac{\omega_m}{2Q_m} t\right) \quad (2.26)$$

This equation can then be utilized to calculate Q_m by filling the cavity for a short time (t_{fill}) then cutting off the input signal and recording the change in energy. This is the most direct way to measure the Q-factor since there is only the energy being emitted from the cavity to measure and not

the forward power. The fill time for this calculation should be long enough that the energy that is accumulated in the cavity will be significantly higher than the energy in the coupler. The selection of t_{fill} can be difficult since knowing the amount of time that the system will need to partially fill the cavity is related to the Q-factor, but since the S-parameters need to be calculated for every case to know the resonance frequency, the Q-factor calculated from the S-parameter should give some guidance. Additionally, only the energy of the system a few nanoseconds after the input signal is cutoff should be used to find Q_m to ensure all energy from the input signal is out of the system. Using this time window, a least squares fit can be applied to Eq 2.16 to find Q_m (C can also be found but is unnecessary).

This approach was first applied to cases A and B, and the resulting Q-factor was applied to find a new quick fill signal. The fill time used to calculate Q was 200 ns, and the times defining the quick fill regions were $t_1 = 500ns$ and $t_2 = 1500ns$. These did require a re-calculation of the S-parameters however, due to an update in the CST software that altered the resonance frequencies by 0.1 MHz and 0.6 MHz for cases A and B respectively. Applying the Q-factors and frequencies from Table 2.4 to Equation 2.17, the full-width half-max ($\Delta\omega$) values are found to be 15.5 KHz and 4.8 kHz for case A and B respectively, which places the newly calculated frequencies at $8\Delta\omega$ and $100\Delta\omega$ away from the calculated resonance, and as such using the old resonance frequencies in the updated software will not excite the desired modes. So while the updates do not change the resonance frequencies by an amount that would call into question the accuracy of the results, the changes are significant to resonance.

The summary of the Q-factors calculated by the two different methods and of the change in energy of steady state of the quick fill signal using each Q-factor can be seen in Table 2.5. The values of the Q-factors themselves did not significantly differ from those calculated directly from the S-parameter, and both the I/O signals and the energy of the recalculated test cases show that calculating the Q-factor from the cavity energy is better than the value calculated from the S-parameter as there was less change in system energy over steady state. Furthermore, the results for case B with the TM_{010}

mode were performed with the Q-factor calculated from the energy decay of the system.

Table 2.5: Q-factors as recalculated for test cases A and B and the change in field energy over steady state when applied to the quick fill method. The resonance frequency f_m changes from Table 2.4 due to changes in the software.

Test Case	f_m (MHz)	Calculation Method	Q	Change in energy over steady state (dB)
A	260.2	S-parameter	16,740	-0.0201
A	260.2	Decay energy	16,860	-0.0195
B	222.3	S-parameter	45,590	-0.0319
B	222.3	Decay energy	46,740	-0.0214

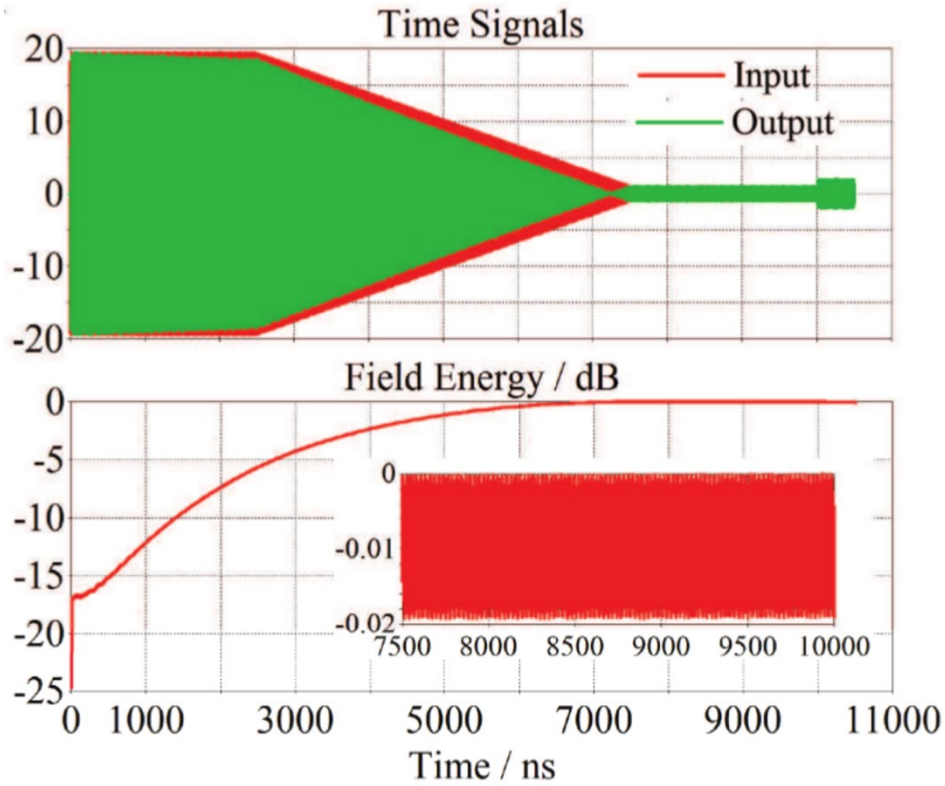


Figure 2.14: Input and output signals (top) and field energy (bottom) of the truncated PEC cavity with drift tubes. The time scale is the same for both parts, and the inset in the field energy shows a more detailed view of the energy for the steady state region. The unit for field energy is recorded in decibels as a magnitude of the maximum energy throughout the simulation, reproduced courtesy of The Electromagnetics Academy.

This method for calculating the Q-factor was then applied to test case C with times t_1 and t_2

as shown in Table 2.4 (row C(ii)) to get the input/output (I/O) signals and the energy (in decibels as a magnitude of the maximum energy throughout the simulation) shown in Fig 2.14. Both of these results confirm that the quick fill works even with the added complexity of drift tubes, and the time to reach steady state was reduced from 525 μs to 7.5 μs . The Q-factor for this case was found to be 66370, which is significantly higher 30220 calculated with the S-parameter, as was predicted by the attempt at a quick-fill signal for $Q = 30220$. This demonstrates the effectiveness of the quick fill method for the highly resonant accelerating cavity.

2.3.3: Analysis of DTL system

With the efficacy of the method confirmed, the EM conditions can be simulated for the DTL coupler. The model will have the dimensions and materials of the DTL, and the method for a quick-fill signal established in the previous subsection will be applied. Then the fields near the RF window can be analyzed, and in particular the placement of the window in relation to the changing electric field strength along the coupler will be considered. Parameters that will be in the simulations can then be compared to measurements taken in the DTL, and the impact of the simulations can then be extrapolated to further issues that could arise in the DTL operation. Finally, some other issues such as off-resonance signals or harmonics in the input signal will be discussed.

First, the model that will be used must be established. The test cases had a distinction in the cavity size, presence of drift tubes, and materials, but the actual DTL cavity also has post-couplers and tuning stubs that help further refine the fields in the cavity. The presence of more structures will lead to rapidly increasing numbers of grid points since the presence of surfaces, and in particular round surfaces like those of the DTL, necessitates the hexahedral meshing to be small to sufficiently approximate them. This means that the benefits of adding the various structures need to be considered against the added computational rigor of smaller discretization of the spatial grid and thus smaller time steps (see Eq. 2.12). The presence of the drift tubes in the test cases acted to shift the frequency of the target TM_{010} -like mode significantly, so the exclusion of the drift tubes would likely lead to inaccurate

frequency calculations, and as such they should be included. The post couplers help to more evenly distribute the fields in the cavity along the direction of the beamline so that the fields are uniform between all drift tube gaps, but this is not of particular interest to the EM fields in the coupler, and as such they do not need to be included. The tuning stubs maintain the frequency of the cavity at 201.25 MHz when there is thermal expansion or contraction that would otherwise shift the resonance frequency from this value, and so their largest influence is on the resonant frequency of the system. If this frequency is off a small amount, the results will not be significantly affected, and so they can also be excluded from the simulation. The other factors that were considered in the test case are now not optional, and so the true tank size and material (i.e. copper) are used. The exact metrics of the drift tubes will be those of tank 4 at the LANSCE facility.

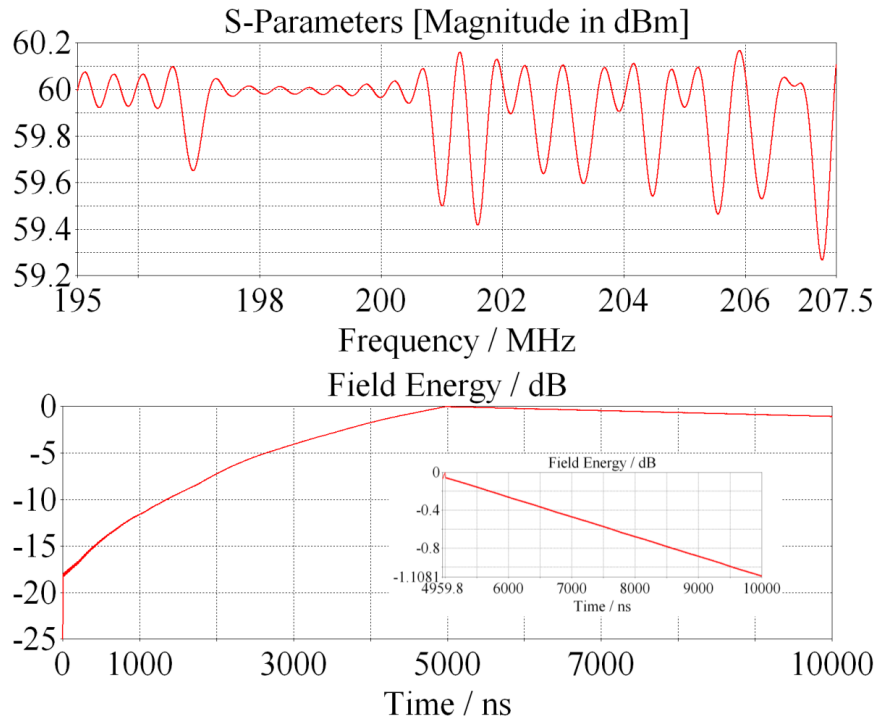


Figure 2.15: S-parameters (top) and field energy (bottom) of the DTL tank 4 used for simulations. The field energy is for the resonant frequency of 201.60 MHz applied for 5000 ns before the signal is cut-off to allow decay.

The resonance and field energy of the system are shown in Fig 2.15. The resonance calculation was run for 2427.3 μ s before being cut-off, resulting in the S-parameter peaks not being as well defined as those of the test cases. Still, the values of the S-parameter were observed throughout the simulation, and the resonance frequencies, especially near the target of 201.25 MHz, were not changing significantly as the simulation continued to run, so these results are sufficient to find the resonance frequency. The resonance frequency that corresponds to the accelerating mode in the cavity is 201.5955 MHz, so this was then used to calculate the Q-factor ($Q = 26,320$) from the decay of the energy signal shown in Fig 2.15. The decaying energy is zoomed into in the inset, and the apparent linear relationship confirms the signal is adhering to the expected behavior at resonance.

With the resonance frequency and Q-factor established, the quick fill signal can be applied to analyze the DTL coupler. It has been established that the times used for the quick fill signal must be carefully selected, and three sets of times t_1 , t_2 , and t_{total} were used, and those values, as well as the initial amplitude, are shown in Table 2.6. While the time needed to perform all of these simulations adds up, the total simulation time is still a fraction of that needed to do a long fill signal. The establishment of cavity fields requires that the input signal spreads throughout the cavity from the coupler aperture, and so the fields of the fully filled cavity are the result of many reflections that require time to reach stasis. The use of quick fill signals will affect how these reflections combine to reach steady state, resulting in noise in the signal that is emitted from the cavity. This in turn affects the output signal, so the use of several quick fill signals also demonstrates how significant noise in the results can be.

Table 2.6: Parameters for quick fill signals used to analyze the DTL cavity. The amplitude and phase of the reflected and emitted signals at steady state are also shown.

t_1	t_2	t_{total}	P_0	χ_r	ϕ_r	χ_e	ϕ_e
5000	7500	10000	7.155009	0.9994	150.5	1.134	-28.8
5000	12500	20000	5.236615	0.9995	150.4	1.140	-28.4
5000	17500	20000	4.166109	0.9993	150.4	1.140	-28.3

The results of these cases are shown in Fig 2.16. First, the I/O signals show the behavior that is expected, with the output reaching zero at some point before steady state, then a fraction of the input at steady state. This changing output signal is the result of the signal that is emitted from the cavity changing with time, and this emitted signal combines with the reflected signal to result in the output signals shown in Fig 2.16. The amplitude and phase of the total output signal (χ_{eff} and ν_{eff} respectively) are then the result of the summation of the constituent reflection ($P_{in}(t)\chi_r \sin(\omega t + kz + \nu_r)$) and cavity emission signal ($\xi(t)\chi_e \sin(\omega t + kz + \nu_e)$) so that

$$\chi_{eff} \sin(\omega t + kz + \nu_{eff}) = P_{in}(t)\chi_r \sin(\omega t + kz + \nu_r) + \xi(t)\chi_e \sin(\omega t + kz + \nu_e) \quad (2.27)$$

where $P_{in}(t)$ is the input amplitude, $\xi(t)$ is the cavity response from Eq 2.22, χ_r and ν_r are respectively the amplitude and phase of the reflection, and χ_e and ν_e are those of the emitted signal. This can be rearranged using trigonometric identities to eliminate the term $\omega t + kz$ to get

$$\begin{aligned} \chi_{eff} \sin(\nu_{eff}) &= P_{in}(t)\chi_r \sin(\nu_r) + \xi(t)\chi_e \sin(\nu_e) \\ \chi_{eff} \cos(\nu_{eff}) &= P_{in}(t)\chi_r \cos(\nu_r) + \xi(t)\chi_e \cos(\nu_e) \end{aligned} \quad (2.28)$$

This too can then be subsequently solved to get

$$\begin{aligned} \chi_{eff} &= \sqrt{(P_{in}(t)\chi_r \sin(\nu_r) + \xi(t)\chi_e \sin(\nu_r))^2 + (P_{in}(t)\chi_r \cos(\nu_r) + \xi(t)\chi_e \cos(\nu_r))^2} \\ \nu_{eff} &= \tan^{-1} \frac{P_{in}(t)\chi_r \sin(\nu_r) + \xi(t)\chi_e \sin(\nu_r)}{P_{in}(t)\chi_r \cos(\nu_r) + \xi(t)\chi_e \cos(\nu_r)} \end{aligned} \quad (2.29)$$

This knowledge of the output phase and amplitude is useful for two interdependent reasons. First, it might be possible to modify the input signal to reduce the EM stress (and as will be discussed later, the MP stresses) on the window. Secondly, the validity of the results can be tested by using them to make analytic predictions that can be compared against signals measured in the cavity at LANSCE.

In order to utilize Eq 2.29, however, the values of the reflection and emission phases and amplitudes must be known. Similar to the calculation of the phase and magnitude of excited HOMs in the previous section, the values of the output signal $y(t)$ can be utilized in conjunction with the reflected and emitted signals to get a least squares fit of the reflection and emission phase and magnitudes. This

is done by setting the left hand side of Eq 2.27 to $y(t)$, while the right hand side can be rearranged to get an equation with four parameters using the property illustrated by Eq 2.7 so that

$$y(t) = c_1 P_{in}(t) \sin(\omega t) + c_2 P_{in}(t) \cos(\omega t) + c_3 \xi(t) \sin(\omega t) + c_4 \xi(t) \cos(\omega t) = c_1 f_1(t) + c_2 f_2(t) + c_3 f_3(t) + c_4 f_4(t) \quad (2.30)$$

where kz was set to zero resulting the coefficients being defined as

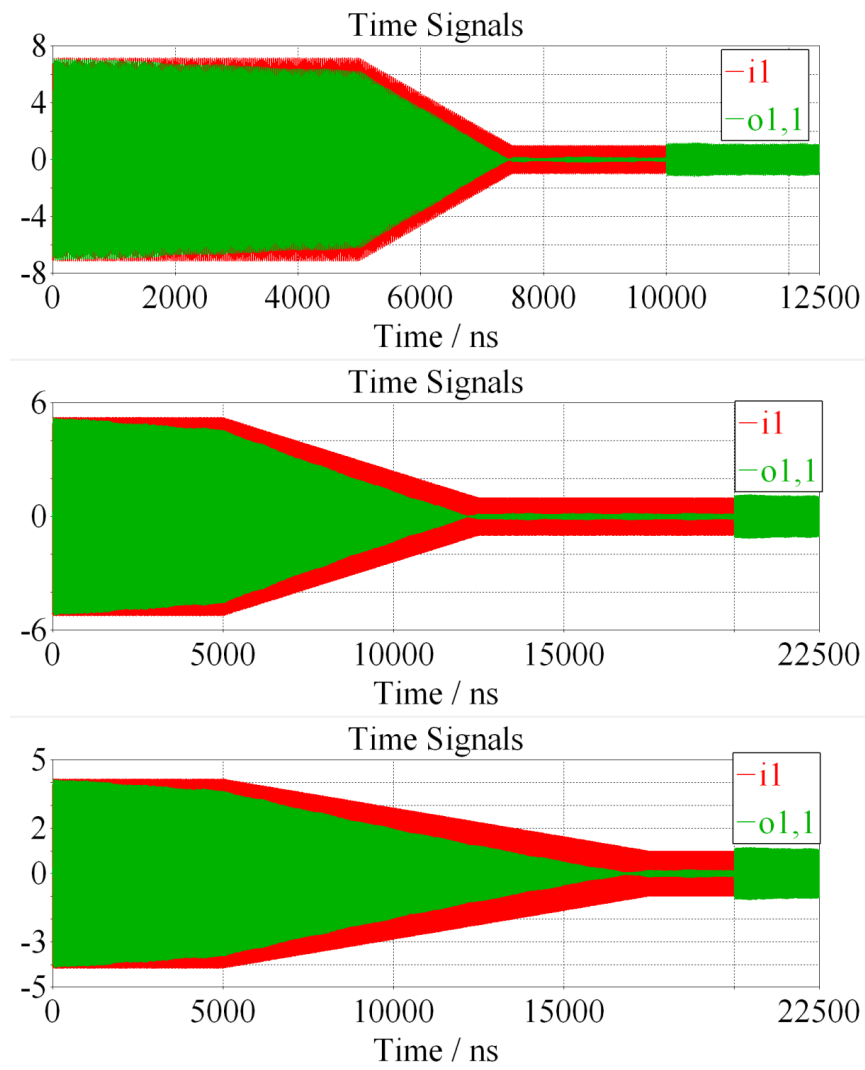


Figure 2.16: The input and output of the various times used to define the quick fill regions as given in Table 2.4.

$$\begin{cases} c_1 = \chi_r \cos(v_r) \\ c_2 = \chi_r \sin(v_r) \\ c_3 = \chi_e \cos(v_e) \\ c_4 = \chi_e \sin(v_e) \end{cases}, \text{ or } \begin{cases} \chi_r = \sqrt{c_1^2 + c_2^2} \\ v_r = \tan^{-1} \frac{c_2}{c_1} \\ \chi_e = \sqrt{c_3^2 + c_4^2} \\ v_e = \tan^{-1} \frac{c_4}{c_3} \end{cases} \quad (2.31)$$

The output signal must be modified to account for the time it takes the input to travel down the coupler then back to the input port, so the signal is shifted by $-2z_{term}/c_0$. The total length of the coupler used in the simulations is effectively 51.12 in, or 1.30 m considering the extra time required for the signal to pass through the width of the window (0.85 in) with a dielectric constant of 2.53. The input will not be shifted in time as this provides consistency with the use of the cavity response ξ as well. The c coefficients can then be found by solving

$$\begin{bmatrix} \sum_n f_1^2(t_n) & \sum_n f_1(t_n)f_2(t_n) & \sum_n f_1(t_n)f_3(t_n) & \sum_n f_1(t_n)f_4(t_n) \\ \sum_n f_1(t_n)f_2(t_n) & \sum_n f_2^2(t_n) & \sum_n f_2(t_n)f_3(t_n) & \sum_n f_2(t_n)f_4(t_n) \\ \sum_n f_1(t_n)f_3(t_n) & \sum_n f_2(t_n)f_3(t_n) & \sum_n f_3^2(t_n) & \sum_n f_3(t_n)f_4(t_n) \\ \sum_n f_1(t_n)f_4(t_n) & \sum_n f_2(t_n)f_4(t_n) & \sum_n f_3(t_n)f_4(t_n) & \sum_n f_4^2(t_n) \end{bmatrix} \begin{pmatrix} c_1 \\ c_2 \\ c_3 \\ c_4 \end{pmatrix} = \begin{pmatrix} \sum_n y(t_n)f_1(t_n) \\ \sum_n y(t_n)f_2(t_n) \\ \sum_n y(t_n)f_3(t_n) \\ \sum_n y(t_n)f_4(t_n) \end{pmatrix} \quad (2.32)$$

Before applying this least squares regression to the signals generated by CST, there are some general relationships between the signal coefficients that should hold true. First, the reflection amplitude must be less than one or there would be no power transferred to the cavity. Similarly, the amplitude of the total outgoing signal must be less than the input amplitude during the fill transient and steady state because there is no source of power coming from the cavity, and as such the cavity is absorbing some amount of incoming power to maintain the fields within it. (This can be violated briefly if there is a drop in input power, but this need not be considered at present.) This effectively limits the emitted signal values to $1 - \chi_r \leq \chi_e \leq 1 + \chi_r$. Second, and related to the first point, is the relationship between the reflection and emission phases. The system is designed to be matched when the accelerated particle beam is present during steady state, meaning that there is no outgoing signal, and this can only

happen when $\chi_r = \chi_e$ and $\nu_r - \nu_e = \pi$. Since this relationship between phases minimizes the effective amplitude, the most efficient coupling of the transmission line to the cavity will maintain this regardless of the presence or absence of the beam, and the calculated values of ν_r and ν_e should have a difference near π . The design to match the cavity to the transmission line while a particle beam is present also means that without the beam, $\chi_e > \chi_r$ since the beam absorbs some amount of power that is otherwise emitted in the absence of the beam.

The calculated values of the reflected and emitted phase and amplitude are also shown in Table 2.6. These values show that these values are generally in accord with the predicted values, and the disagreement illustrates how the quick fill affected results. The R-squared ($R^2 = \sum_n (y(t_n) - c_1 f_1(t_n) - c_2 f_2(t_n) - c_3 f_3(t_n) - c_4 f_4(t_n))^2$, see Eq. 2.30) values decreased with the initial amplitude of the quick fill signal, indicating that the application of the method does introduce some artifice. The difference between all the calculated results is largely negligible however, showing that despite some instability introduced by the quick fill, the smallest times t_1 and t_2 will provide results that are consistent with longer fill times.

These calculated amplitude and phases can be applied to predict the field conditions in the coupler, and those predictions can also be compared to the calculated results from CST. The window is set at a good position to minimize the EM stresses, as it is placed near the electric field minimum during the initial portion of the fill, but there could still be some issues with the multipactor phenomenon as discussed in chapter four. There are some slight dips in the electric field values at the window location due to the increased electric permeability of the Rexolite. The axial field values were also recorded, and there are some non-zero values near the window, with higher axial components near the changing geometry of the coupler. These are of little interest in terms of the EM stress since they are significantly less than the radial fields, but can be of interest when discussing multipactor later.

The calculated reflection and emission parameters can also be benchmarked against measured results taken from the real world cavity. Measurements of the forward power, reflected power, and

cavity fields were taken during the absence of the beam of tank M1. The use of Eq 2.29 should allow the reflected power to be found knowing only the input power, and subsequently the cavity fields, so the measurements taken at tank one can be compared to the predicted values using the parameters found using CST. The use of tank one measurements are expected to be comparable to the CST simulation of tank four because of the various tuning structures that keep all tanks operating at the same EM conditions. It should also be noted that there are variations in the simulation from the real world tank four that are acknowledged, such as the resonant frequency, and some deviations would be expected in the benchmark anyway, further negating any significance using tank one comparisons might have.

Several predictions of the reflected power were made to compare the effect of the various calculated parameters. All benchmarks normalized the input power, reflected power, and cavity fields to unity because this allows results to be more readily calculated and compared, and this is sufficient for the targeted qualitative comparison. The reflected power and emitted power phases were assumed to be correct from CST since it has already been shown theoretically that they should be approximately 180° apart, and the measured reflection magnitude without the beam also has a zero value during the fill to confirm this. The cavity response to the input and the reflection magnitude were then modified to compare the reflected power to the measurement, and these are shown with the measured reflection power in Fig 2.17.

The measured cavity response was first used with an emitted power magnitude of $\chi_e = 1.08$ (case A) set so that the calculated reflection magnitude matches the measured during steady state. This provides a basis to understand how well the calculated reflection magnitude could possibly match the measured when considering the artifice of the quick fill method in the CST simulations, and the steady state magnitude has been set specifically to match. Then the reflection magnitude was found using a calculated cavity response to the measured input power from tank 1 using the same Q-factor that was calculated from CST results. This was done using both the calculated emission magnitude (case B) and the matched emission magnitude of $\chi_e = 1.08$ used earlier (case C), then the cavity response was

calculated using a Q-factor that is adjusted slightly to 28,790 in order to better match the measurements (case D). These various calculated reflection magnitudes are meant to better understand how the cavity fields affect the overall signal that is reflected.

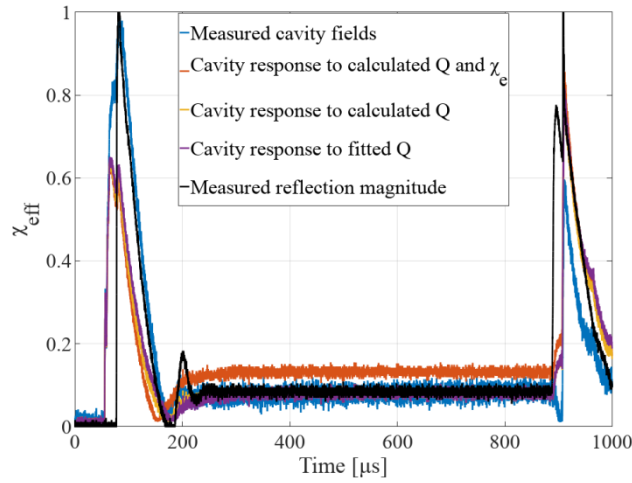


Figure 2.17: Comparison of the calculated reflection magnitude to the measured power reflected in tank 1 of the DTL. The reflection magnitudes were calculated with the values of χ_e calculated from I/O signals and using a cavity response that was predicted using both the calculated value of Q and a fitted value of Q. The reflected power was also calculated for that value of χ_e with the measured cavity response.

The qualitative comparison of the calculated reflection magnitudes with the measured show the use of the reflection and emission phases and amplitudes to be sufficient, albeit imperfect, to calculate the signals generated by an input power. The use of the measured cavity fields with the fitted emission magnitude (case A) show the general limitations of how well the transient features of the calculated reflection magnitude can be expected to match the measured. For example, the measured reflection magnitude peaks to one (due to normalization) at around 100 μs , and the value of case A follow those of the measured closely at that time. But there is a second peak in the reflection when the input power drops near 900 μs where the values of case A are noticeably smaller. Additionally, the behavior of case A when the input power is reduced at 890 μs does not follow either the same pattern or have values approximate to those measured in that region. These show that there are incongruities in the measured

values that prevent more than a qualitative analysis from being performed.

Considering the limitations on how well the calculated values can match measurements, the values found from CST seem to be confirmed as plausible. The Q-factor and magnitude of the signal emitted from the cavity calculated from CST (Case B) do match the other cases C and D in both behavior and values at most times. The biggest deviation that Case B makes from all the other reflection magnitudes is during steady state and just after the input power was reduced at 890 μs , and this is due to the larger emission magnitude of $\chi_e = 1.13$. The calculated Q-factor from CST was found to be $Q \approx 26,000$, which is less than other calculated Q-factors of the DTL cavity ($Q > 50,000$) [19] [25], and considering the definition of the Q-factor in Eq 2.1, it can be expected that there is a greater loss of power, and thus higher χ_e for lower Q-factors, as was observed. That is why the emission magnitude that was used to fit Case A to the measured values was used in conjunction with the calculated cavity response in Case C, and then the additional step was taken to use a higher Q-factor to re-calculate the cavity response with $\chi_e = 1.08$ to get Case D. Both of these instances showed similar results with no real distinction between them. Overall, the combination of the reflection and emission phase and magnitudes to get the overall reflection of the input signal throughout the fill transient is confirmed. This allows other fill signal envelopes to be used to reduce the EM stresses on the window, and the other remaining EM analyses can also use this approach to provide a basis for the RF window design and operation.

2.3.4: Harmonics and off-resonance conditions

There are two other conditions that are commonly observed in accelerator operations that should be addressed. The first is that of harmonics in the input signal due generated by the tetrode that provides power to the system. These can add more EM stress that has thus far been unaccounted for, and if they excite modes in the accelerator, there could also be interference with the delivery of power to the beam. The second issue is that the cooling system that mitigates the thermal stresses will overcool the cavity in the absence of the RF power, thereby causing the cavity to shrink and the resonance

frequency to subsequently increase. This can also have unexpected consequences, and the discussion of off-resonance excitations will also be of interest to some other observed results.

In order to analyze the impact of signal harmonics, the resonance calculations first have to be run with an improved mesh. Since the mesh grid size is automatically calculated in CST based on the upper limit of the frequency range, previous calculations will not be accurate for harmonics since their frequency range was set to be $195 \text{ MHz} \leq f \leq 207.5 \text{ MHz}$. This maximum frequency was then increased to 610 MHz with the maximum spatial step width remaining at $\lambda_{min}/30$ to ensure the resonance frequencies of the accelerating cavity were accurately captured for up to the 3rd harmonic of the baseline 201.25 MHz frequency. The S-parameters are shown in Fig 2.18 near each harmonic frequency. The frequency corresponding to the desired accelerating mode is at 202.23 MHz, making it only slightly farther from the resonance frequency of the actual accelerator, and this is marked with a vertical line in the topmost portion of Fig 2.18. The second and third harmonics are shown in the other two parts of the figure, with vertical lines marking the frequencies of those harmonics.

The accelerating cavity does not show resonance frequencies at the harmonic frequencies, which is both expected analytically and certainly beneficial. Similar to the wavenumber of higher order modes scattered in the coupler from the window, the wavenumbers of the transverse and axial components of the cavity constitute the resonance wavenumber such that

$$f_{res} = \sqrt{f_{tran}^2 + f_{axial}^2} \quad (2.33)$$

In order for the resonance frequency of the cavity to be an integer multiple of the base frequency, the transverse and axial wavenumbers (k_ρ and k_z respectively, see Eq 2.24) would have to allow Eq 2.33 to be satisfied. The axial wavenumber is generally scalable by integer values (see Eq. 2.25), whereas the transverse wavenumber is not, and so resonances at integer multiples will not generally occur. The S-parameters in CST bore this out as there were not resonant frequencies at the integer multiples of the baseline frequency of 202.23 MHz, so any harmonics present in the input signal

will not excite additional modes in the cavity.

While this is desirable for the acceleration of the particle beam, it still does not guarantee that harmonics in the RF signal will be benign to the RF window. Regardless of the cavity response to the harmonics, there will be a reflection at the line terminus, and as such the harmonics should be considered

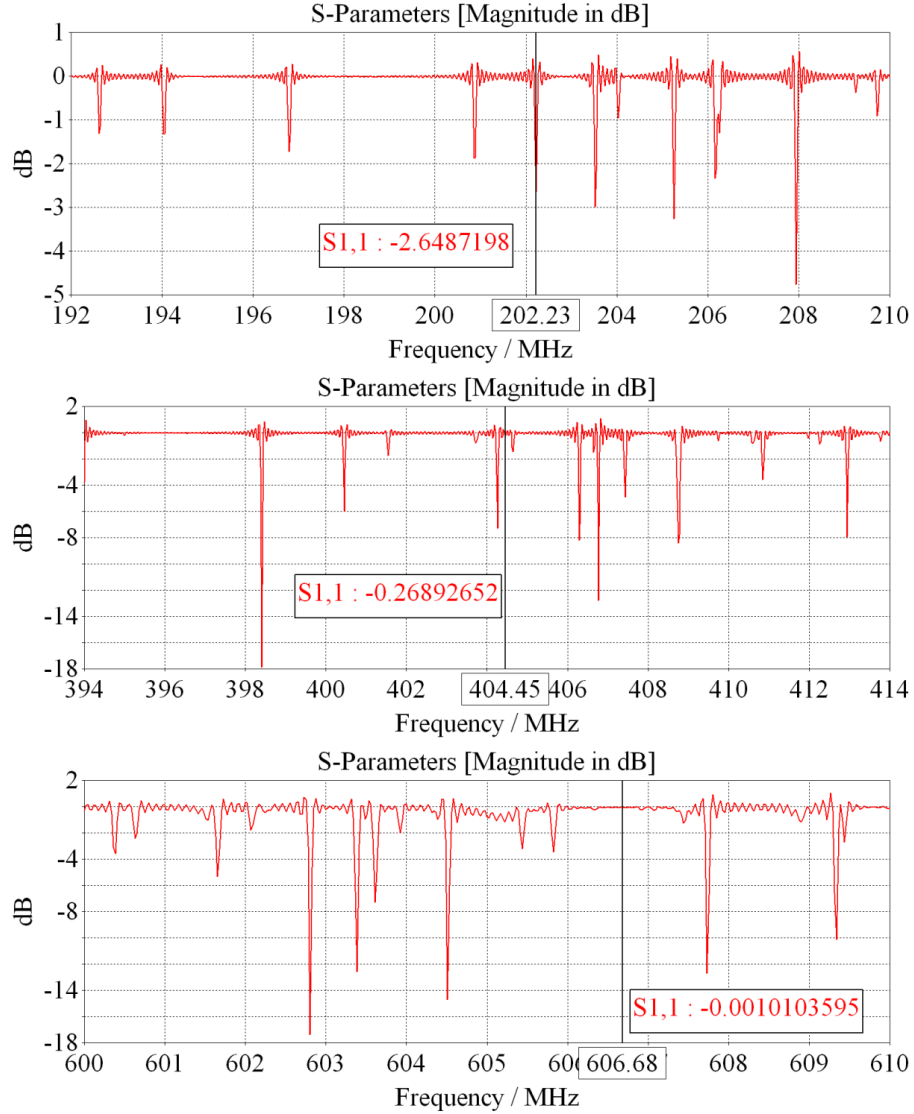


Figure 2.18: S-parameters for the DTL tank 4 with a mesh fine enough to simulate the harmonics of the 201.25 MHz input frequency. The top portion shows the S-parameter near that input frequency, and the calculated frequency corresponding to the accelerating mode of the cavity is 202.23 MHz. The S-parameters near the second harmonic (middle part) and the third harmonic (bottom part) are also shown with the harmonic frequency labeled.

in regards to window placement. The quick fill signal was used with the second and third harmonics added at a tenth of the amplitude of the baseline frequency, and the energy of the filling signal is shown in Fig 2.19. The energy is as expected with no change to the system energy throughout steady state, indicating that the harmonics will not significantly affect the fields stored in the cavity as expected. However, this does not correspond to expectations for signal reflections as the I/O signals in Fig 2.20 show.

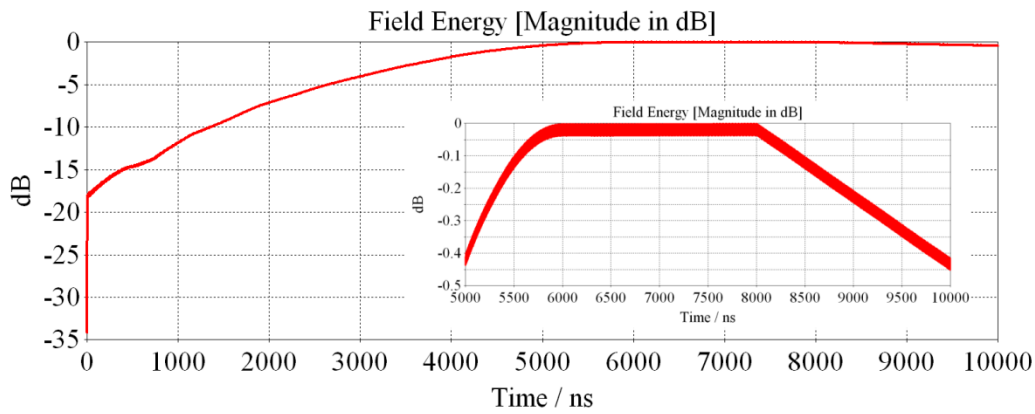


Figure 2.19: Field energy of tank 4 and the power coupler for the quick fill signal with the second and third harmonics added to the quick fill signal. The harmonics only affect the system energy early in the simulation (i.e. before ~2000 ns) when cavity fields are low and fields in the coupler are significant to the overall system energy. The detailed energy in the steady state and cut-off regions is shown in the inset.

The output of the signal with second and third harmonics added shows a significant deviation from what would be expected based on previous results without the harmonics. Those previous results, such as found in Fig 2.16, had signals that were balanced in regards to their polarity, i.e. the maximum values were approximately the same magnitude as the minimum values for a particular time range, but this was not the case for the beginning portion of the signal with added harmonics. Instead, this signal had minimum values of a noticeably higher magnitude than those of the maximum values, so it can be inferred that the interaction of the signal with the coupler terminus and the accelerating cavity does have some effect on the reflected signal. The imbalance in the signal polarity does fade however as the

cavity fills. The signals of the second and third harmonics with the same quick fill amplitudes were also run in isolation from both the baseline frequency and each other to ensure that these signals did not have any appreciable accumulation of cavity fields that could contribute to this interaction, and the energy of these simulations were consistent with minimal excitation of additional modes in the cavity. This means that the change in the balance of the output signal is due largely to the change in the relative phases between the baseline and harmonic frequencies.

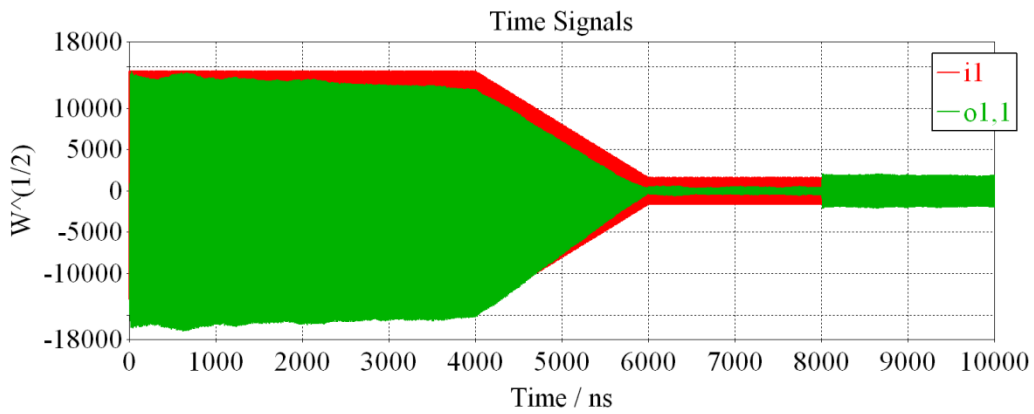


Figure 2.20: Input and output signals of the quick fill with harmonics added.

The previous analysis on the output signal using a least squares fit was also performed for these signals to examine how the change to the total reflection of the baseline frequency might interact with the harmonics. To that end, the least squares method was first applied only to the steady state region between 6050 ns and 7950 ns similar to how it was applied in Eq 2.30, but with the subscripts representing the harmonics of a signal with a constant amplitude. This gives the relative magnitudes and phases of the baseline and harmonics over steady state. This same approach was also taken to analyze the phase and magnitudes of the pure reflection at the beginning of the transient fill signal from 50 to 500 ns. The constant amplitude was applied to this relatively short time frame so that the filling of the cavity would not have a significant effect, which was necessary because some excitation of modes

by the harmonics was observed previously that was not significant enough to warrant the additional calculations necessary to have a thorough analysis of the signals. The results of these least squares fits are shown in Table 2.7. The phases of the harmonics would be expected to be consistent between the transient and steady state regions, and there was a decrease of 10° for the second harmonic and 20° for the third harmonic between the transient and steady state results. These differences are slightly higher than what might be expected due to noise in the signal and the error in least squares approximations, but again indicating that some interaction between the pure reflection of the harmonics and small emissions from the cavity at the harmonic frequencies. The ratio of magnitudes between the baseline and harmonic frequencies decreased from the transient to steady state regions as the total reflection of the baseline frequency decreased. The quick fill signal used a value of $P_0 = 8.786$, so multiplying the values for steady state magnitudes shown in Table 2.7 by this value are consistent with the signals remaining unchanged for the harmonics ($1425.4 \text{ W}^{-1/2}$ and $1524.6 \text{ W}^{-1/2}$). These overall reflections of the harmonics are significant alterations the expected fields, and their minimization is crucial to proper window function.

Table 2.7: Magnitude and phases for all harmonics of the output signal for the transient fill from 50 to 500 ns and for the steady state portion of the signal between 6050 and 7950 ns.

Harmonic	Transient Magnitude ($\text{W}^{-1/2}$)	Steady state Magnitude ($\text{W}^{-1/2}$)	Transient Phase ($^\circ$)	Steady state Phase ($^\circ$)
Baseline	15054	262.24	113.2	-78.07
2 nd Harmonic	1484.4	162.24	10.74	0.5253
3 rd Harmonic	1312.9	173.53	-100.5	-120.0

The inclusion of harmonics in the simulations also led to the increased excitation of HOMs. The first two HOMs seen in Fig 2.21 have cut-off frequencies of 379.5 MHz, so these two modes can propagate down the line should they be excited by the harmonics at 404.5 MHz and 606.7 MHz. These modes are the degenerate TE_{11} modes, and a visual inspection of the fields at the port shows the axial component of the magnetic field being maximized at just a few degrees off of the location of the

coupling loop that magnetically couples the accelerating cavity to the transmission line, while the other TE_{11} mode is rotated $\sim 90^\circ$ from the first as expected. In order to analyze the HOMs excited by the harmonics, the simulations used a modified geometry with the port again placed only 1.5 in. from the air surface of the window similar to what was done in the coupler only subsection. This allows the excitation of HOM's to be recorded during simulations, and a few voltage monitors were also used to record the overall effect that harmonics and any scattered HOMs might have on the window.

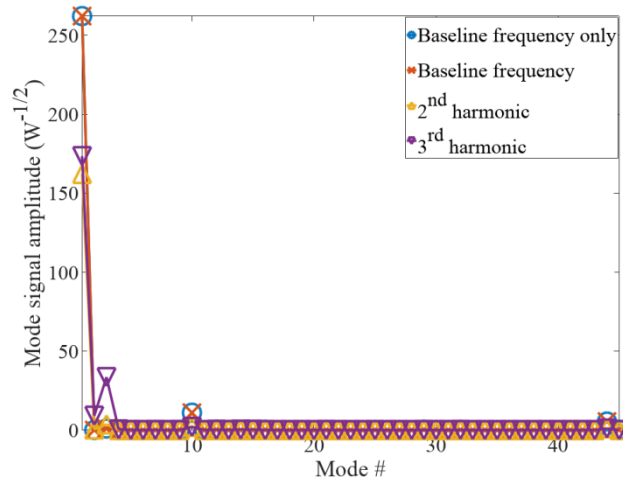


Figure 2.21: Calculated mode amplitudes during steady state for the quick fill both with and without harmonics. The amplitudes of the baseline frequency and the harmonics are individually displayed.

There were significant changes to the observed scattered HOMs due to the addition of harmonics in the input signal. The modes that were analyzed included the TM_{0n} modes, and the excitation of HOMs was also recorded for the signal without any harmonics as well. The amplitudes were found from the recorded port signals during steady state using a least squares fit as was done previously for only the TEM signal, and those non-negligible amplitudes are shown in Fig 2.21. The amplitudes for the baseline frequency are indistinguishable between the signals with and without the harmonics added, which is a good indication of consistent results from both the simulations and the

least squares fit, and the TEM modes are the same as those shown in Table 2.2. The TM_{0n} modes had similar results as those of the coupler only for the baseline frequencies as well, but both harmonics had decreased amplitudes of these modes. The most interesting results are the non-zero amplitudes resulting from the TE_{11} modes because they show that the inclusion of the harmonics has an effect on window performance. The relative peaks between mode numbers 2 and 3 indicate that the axial component of the magnetic field is strongest at the azimuthal locations on either side of the coupler foot as would be expected. Other TE modes are likely scattered by the coupler loop, but the cut-off frequency prevents them from propagating back to the window, and the decrease in coupler size nearer the coupler assists in this by increasing the cut-off frequency to 586.4 MHz.

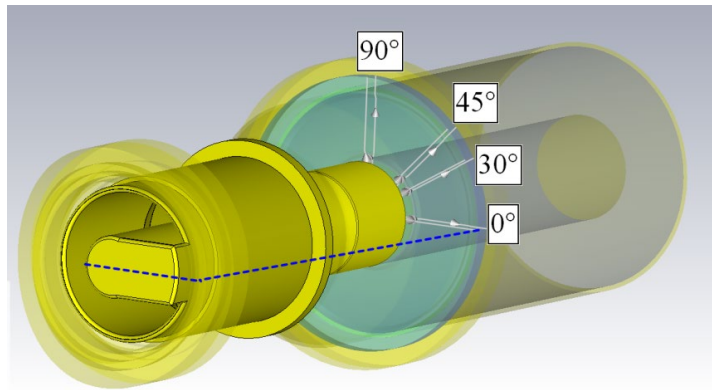


Figure 2.22: Locations of voltage monitors used for simulation with harmonics added to the input signal. The centerline of the coupling foot is marked by a dashed line that is carried back to the voltage monitor at 0° for visualization.

The analysis of fields in the isolated coupler showed that the use of harmonics can be insufficient for properly describing the fields, so to analyze the stresses on the window, voltage monitors were also utilized. The first voltage that was recorded went across the air surface of the window from the inner to outer conductors, and the second was set across the window thickness at the same radius as the inner conductor, both of which were also used in the coupler only subsection. An

immediate consequence of the modes that were observed during steady state is that the fields will change with azimuthal position on the window, so the voltage monitors were defined for angles of 0° , 30° , 45° , and 90° offset from the centerline of the coupling loop, as illustrated in Fig 2.22. The voltages shown in Fig 2.23 were then normalized by the changing amplitude used for the quick fill signal to better illustrate the change in voltages over time.

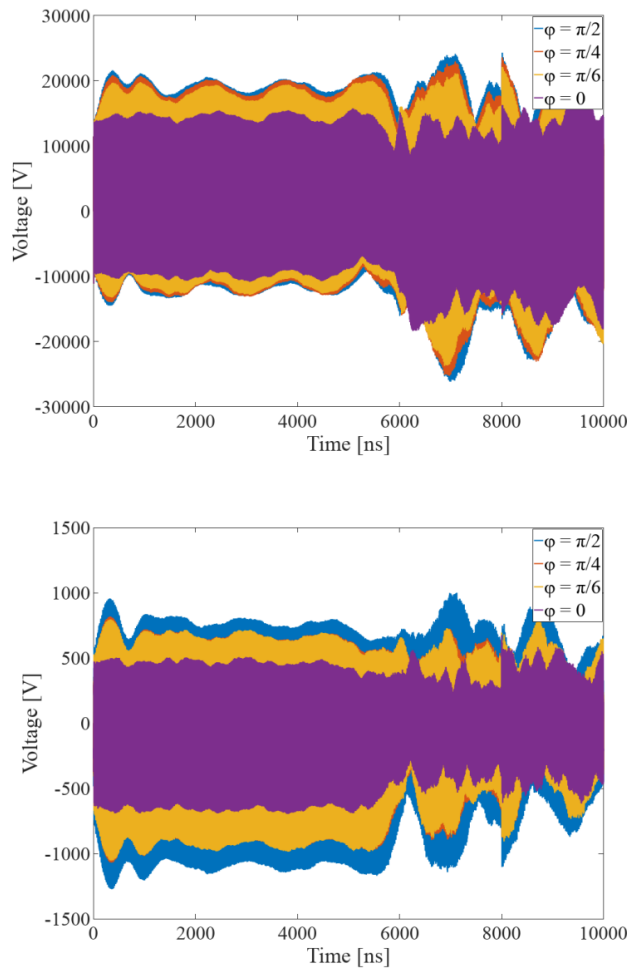


Figure 2.23: Voltages across window at various azimuthal locations relative to the coupler foot. The voltage across the air surface of the window (top) and the voltage across the window thickness (bottom) both are measured at a number of angles as measured clockwise from the centerline of the coupling loop.

There is a slight dependence of voltages on the azimuthal locations. Those monitors that are

farther from the angle of the coupling foot have the highest voltages, and these are the locations that the scattered HOMs would indicate strong changes to the fields to be. These voltages are typically higher than what is observed without the harmonics in spite of the peak power of the input signal being slightly lowered by the addition of the harmonics because the phase of the harmonics as they are reflected allows the electric fields to be enhanced, which is detrimental to window performance. The magnitude of the voltages also changes little with time, even after the input has been cut-off, indicating that there are some fields that accumulated in the cavity due to the harmonics. This can be explained heuristically as being due to the harmonics being able to excite the nearest modes (in terms of frequency) a marginal amount while the time that the simulation was run without an input signal (2 μ s) was short compared to the decay time of the modes excited by harmonics. The beginning of the voltage signals also display a pattern that is consistent with the excitation of modes by a signal that is slightly off-resonance, as will be discussed shortly.

The implication of the voltages in Fig. 2.23 is that the presence of unavoidable harmonics in the input signal will increase EM stress on the RF. The voltage across the window surface is increased for even the angle of 0° from the signal without the harmonics, and the other angles have an even more significant change as there was no difference between voltages at different angles in the signal without harmonics. The voltage measured through the bulk of the window was approximately the same as measured without the harmonics, but the other angles again saw an increase in voltage when the harmonics were added. Neither measure of voltage is desirable, indicating how parasitic the harmonics are. This could partially account for the occurrence of wormholes at approximately 30° from either side of the foot, with multipactor also being both a potentially important contributor to those failures and effected by the change in fields due to harmonics.

While it will be shown later that a case can be made that those azimuthally-dependent failures are due to multipactor, the best practice is to also eliminate the stress caused by the higher order modes as their effect on window performance is uncertain. This is ideally done by completely eliminating the

harmonics at the source, but as this is not possible, another solution is to simply decrease the line radii to increase the attenuation of the higher order modes. The size of the transmission line at the window does allow for the TE₁₁ modes to propagate without attenuation, but the coaxial diameters are smaller nearer to the cavity, and those dimensions have some attenuation of potentially harmonic scattered HOMs. Table 2.8 shows the relevant information for HOM attenuation in the three segments of the transmission line, including the attenuation of the HOMs for ten inch segments of both the smallest mid-size diameters—roughly equivalent to the current geometry. While there is good attenuation of the second harmonic, the third harmonic is still reduced by only a third by the decreased diameter, so the segment of smallest diameter should be lengthened as allowed by the other factors (e.g. physical space for expansion). Of course, should this require physically moving the window farther from the cavity, there will also be effects on the window position relative to the standing wave, and so any window movement should be by a multiple of $\lambda/2 = 29.3 \text{ in.}$

Table 2.8: Properties relevant to the excited TE₁₁ mode in the coupler between the RF window and accelerator cavity.

Property		Near window	Mid-coupler	Near cavity
Inner radius		3.0625	1.98	1.8125
Outer radius		7.0435	4.56	4.1705
Cut-off frequency of TE ₁₁ (MHz)		379.47	586.40	640.97
Strength of attenuated second harmonic (% of signal emitted at cavity)	Per segment	—	10.4	7.1
	At window	0.7		
Strength of attenuated third harmonic (% of signal emitted at cavity)	Per segment	—	—	33.3
	At window	33.3		

The last detail that could affect window performance is changes to the cavity resonance that can occur if the cavity is overcooled. The high fields present in the accelerator system cause a lot of heat to be dissipated in the walls, necessitating a cooling system to keep the system operational. But in the case of the cooling system being imbalanced with the heat dissipated, as might happen if there are not RF pulses for an extended period of time, then the cavity will be cooled too much, leading to the

cavity shrinking. Subsequently, the resonance frequency of the cavity will increase, leading to issues when attempts are made to fill the cavity at the set 201.25 MHz.

There are numerous difficulties in attempting to accurately simulate this off-resonance behavior, and because it is of less interest than what has thus far been discussed, the analysis of this phenomenon will be limited to a qualitative discussion. A major difficulty in simulating the cavity response when the cooling has rendered it off resonance is the transient nature of the cavity being gradually heated and brought back to resonance as RF power is applied. As the signal is applied, even if off of the resonant frequency of the cavity, there will be more heat dissipated and the cavity will slowly return to the resonant frequency of 201.25 MHz. While CST has the ability to perform the multiphysics simulations pertinent to this, ensuring accurate results would not be worth the added effort. Additionally, extra effort would be required to not only apply the quick fill to the EM fields, but also to those thermal and mechanic considerations, which again is beyond the scope of what is necessary for this analysis.

The generic behavior of off-resonant signals will be discussed in terms of an example response to changing resonance frequencies. The cavity response ξ to a constant amplitude, constant frequency signal was applied to a changing resonance frequency. The resonance frequency was set to a constant value of ω_{off} for the first 50 μs , then the resonance frequency was decreased linearly from ω_{off} to the goal frequency from 50 μs to 250 μs and held constant from there to the end. Several values of ω_{off} were set so that the ratio to the baseline frequency ω_0/ω_{off} was 0.99, 0.999, 0.9995, or 0.9999. The resonance frequencies of 200.875 MHz and 202.23 MHz and their respective Q-factors calculated from CST (see Fig 2.18) were used because some of their respective ω_{off} values will be higher than the driving frequency (202.23 MHz) at the beginning of the calculation. This is comparable to what occurs in an off-resonance cavity, and both resonance frequencies were adjusted by the same factor during the initial 50 μs period of off-resonance.

The results of the various transient resonance frequencies are shown in Fig 2.24. The time when

steady state is reached is shifted by a few hundred μs for the shifted resonance signals as expected due to the lack of the mode being driven at the proper frequency throughout the pulse. Off-resonance excitations of the modes result in oscillating amplitudes about some non-zero value, with the oscillations occurring at larger intervals the closer the driving signal is to the resonance frequency of the system. This is a consequence of the solution to the resonance equation (Eq 2.16), and this same behavior has been observed in the scattering of HOMs by the RF window and in the voltages due to the harmonics added in Fig 2.20. The greatest shift in resonance frequencies does have a spike in ξ near 150 μs due to the excitation of the shifted 200.875 MHz mode.

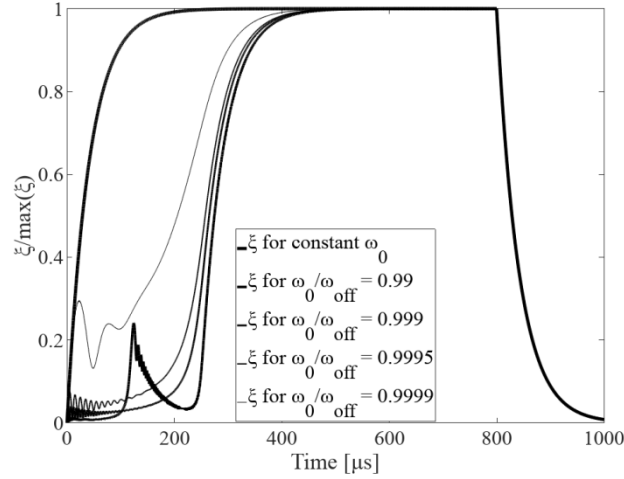


Figure 2.24: Response of cavity to a constant input frequency when the cavity shifts in its resonant frequency. The initial resonance frequency was set to be ω_{off} for 50 ns, before being decreased in a linear manner over time to the resonance frequency calculated for the as is tank in CST.

The response of the signal to changing resonance frequencies implies some minor effects that could impact the stress on the RF window. First, the delay in the fill of the cavity will lead to changes to the total reflection as the signal emitted from the cavity will in turn be delayed. While this is insignificant, or perhaps even preferable, when the change to the resonant frequency is larger, the smaller resonance shifts will result in the signal emitted from the cavity being larger, thus affecting the anticipated EM stress on the window. However, should the shift in resonance frequencies be too great,

the input signal can start to excite other modes within the cavity, which could lead to many unpredicted consequences, particularly in the presence of a beam. In general however these changes to the cavity responses are not altogether unknown to the standard operation of the accelerator as they still are within the range experienced by a constant resonance frequency, so the changes to the EM fields (and to multipactor discussed in chapter 4) caused by the off-resonance are only important in the times at which they occur.

This chapter, in part, is a reprint of material as it appears in T.W. Hall, P.R. Bandaru, D.E. Rees, Progress in Electromagnetics Research **44**, 149-160 (2015) , courtesy of The Electromagnetics Academy. The dissertation author was the primary investigator and author of the paper.

Chapter 3

Multipactor—Principles and Simulation

3.1: The multipactor phenomenon

In addition to the analysis of the EM stresses on the RF window, the consideration of the multipactor (MP) phenomenon must also be made. MP is a well-known issue that has plagued the design of vacuum RF systems since their inception [13] [15] [16] [17] [28] [29] [30] [31] [32] [33] [34] [35] [36] [37]. The phenomenon of MP arises from a complex interaction of electrons with surfaces, whereby some electron collisions can cause multiple electrons to be emitted from the surface, which in turn—for certain EM conditions—will lead to an exponential growth of the electron population. The specific conditions when this occurs—and by extension when it does not—are difficult to find, and can generally only be found numerically. This has led to a number of publications on this phenomenon, and the specifics of MP near the RF window also require their own consideration.

The complexity of the phenomenon and its simulation will be discussed in this chapter, while the application of these principles to the RF window will be discussed in the next chapter. First, the foundational principles of secondary electron emission and the resonant collisions of electrons with rudimentary structures are discussed in order to illuminate the considerations that will need to be made when analyzing the RF window. Next, the simulation of MP will be discussed. This is a significant topic to be addressed and has many factors that complicate how MP can successfully be simulated, including emission models and the analysis of MP from calculated electron trajectories. The accuracy of the MP simulations is then verified via several benchmarks, including comparisons to analytical approximations, experimental observations and other computational methods whose accuracy is well established. In the next chapter, these simulations are then applied to the general case of an RF window in a coaxial line, and then to the specific case of the DTL.

The generation of MP in a system is a complicated process that requires two interrelated criteria

to be met for it to occur [33]. The first criterion is that the EM conditions in the device being considered allow for electron trajectories that regularly repeat themselves [38] [39]. This will be referred to as the resonance criterion, as the electron trajectories form an interaction with the EM fields that allows each collision to build off all previous collisions. The second criterion requires that the collision of electrons with surfaces leads to more than one electron being subsequently emitted from that surface, and this will be referred to as the emission criterion. The exact physics of meeting either of these criteria will affect the other, but first each of these criteria must be carefully analyzed.

3.1.1: Emission criterion of multipactor

The emission criterion is difficult to quantify, but its application to the analysis of MP is straightforward. Ideally, for any given material, the number of electrons generated by a collision would be able to be calculated directly from the electron velocity and angle of collision with the surface, but the interactions between impacting electrons and the atoms of the surface material are dominated by quantum effects that make a deterministic approach impossible. Rather, the secondary electron emission yield (δ) has been studied extensively for different material types [40] [41] [42] [43] and collision considerations empirically. The empirical data does exhibit a general behavior, however, with a peak value at some given energy E_0 and values greater than one between two “cross-over” energies E_1 and E_2 . This general behavior has led to the development of two major models that are typically used in the field of MP: the Vaughan Model and the Furman Model.

The Vaughan Model [44] was derived as a purely empirical fit to available data and is useful in its ease of employment. A more detailed approach to describing the secondary emission phenomenon was carried out by Furman [45]. This model was based on a detailed analysis of probabilities of the constituent electron-atom interactions that can occur for a given collision. This allows for a more precise tuning to experimental data, but it also requires more parameters to adjust for any given material, making it more difficult to both calculate those parameters and apply the model to simulations.

The three constituent electron-atom interactions that can occur are backscattering, rediffusion,

and true secondary emission, and these exhibit an additive relationship to the overall secondary electron emission yield such that $\delta = \delta_b + \delta_r + \delta_{ts}$, where δ_b , δ_r , and δ_{ts} are the secondary emission yield of each of the phenomenon. The backscattering and rediffusion interactions can only occur with the impinging electron, so the values of these secondary emission yields must theoretically be $\delta_b + \delta_r \leq 1$. The backscattering of the electron occurs when there is an elastic collision with the atoms of the surface material, and δ_b generally is highest for lower collision energies. The impinging electron can also be rediffused by experiencing one or more inelastic collisions with the atoms, and the value of δ_r is then appropriately related to the collision energy in a manner inverse to that of the backscattered electrons. The true secondary emission, then, is the emission component whereby electrons are imparted with energy from the impinging electron such that they are emitted from the atom and into the vacuum. This is the process by which the electron population grows and makes the MP phenomenon parasitic to standard operation.

An additional advantage that this model offers though is that it also allows for a more detailed analysis of the electron emissions. Whereas the Vaughan Model gives a value for the secondary emission yield, the probabilistic approach of Furman also allows for stochastic emission velocities of the secondary electrons to be calculated [46]. The values of δ_b , δ_r , and δ_{ts} are calculated for the collision energy, but these values can also be represented in a differential form with respect to emission energy $d\delta/dE$ such that the integration of this term from zero to the collision energy E_c gives the total emission yield

$$\delta_{type} = \int_0^{E_c} \frac{d\delta_{type}}{dE} dE \quad (3.1)$$

where the subscript type is a generic term for any of the emission mechanisms. The spectrum of $d\delta_{type}/dE$ can then be applied to find generate information about the electrons generated, as detailed later.

3.1.2: Resonance criterion of multipactor

In contrast to the emission criterion, the resonance criterion is not subject to tenuous, material-dependent data, but it instead applies to the geometries of the devices in which it occurs. The justification for the resonance criterion is that the electron trajectory between collisions should occur in regularly repeating patterns in order for the emission criterion to continue to be met upon subsequent collisions. This might not happen in all conditions where MP occurs [47] [48] [49], but it is an ideal that will allow for the prediction of MP by simply calculating electron trajectories. For some simple systems, these trajectories can be calculated analytically, but generally numerical methods are required. Even if the trajectories of a more complex geometry can be approximated, such as with the coaxial geometry of the DTL power coupler [38], there will still be factors that can complicate whether or not the resonance condition is met. One complication is the presence of multiple MP modes where multiple trajectories can allow for repeating collisions with the emission criterion being met. Another complication arises from the stochastic nature of the electron emissions as discussed above, in that the emission velocity will not be the same for all emissions, and therefore the repetition of trajectories between collisions will be impossible to predict. In general analyses though, the resonance criterion provides an important basis to consider whether or not MP occurs.

3.2: Multipactor in infinite parallel plates

To illustrate how these criteria work together to generate MP, the simple case of parallel plates is considered. This theoretical geometry is useful because for plates of infinite size the electric field between them is uniform, thereby allowing an exact calculation of the trajectory given a constant emission velocity. The trajectory can be found by considering the Lorentz force

$$\frac{d^2x}{dt^2} = \frac{q_e E_0}{m_e} \sin(\omega t + \phi) \quad (3.2)$$

where x is the position between the two plates, q_e and m_e the electron charge and mass respectively, E_0 is the electric field amplitude, ω is the angular frequency, and ϕ is a phase modifier. The solution

of Eq 3.2 assumes that all emissions are normal to the plate surface with a speed of v_0 such that the trajectory is one dimensional, resulting in

$$x(t) = -\frac{E_0}{\omega^2} \sin(\omega t + \phi) + \frac{v_0 \omega + E_0 \cos(\phi)}{\omega} t + \frac{E_0}{\omega^2} \sin(\phi) + x_0 \quad (3.3)$$

where x_0 is the initial position of the electron.

3.2.1: Frequency-gap width product

The electron trajectory can then be applied to the MP criteria. First, the emission velocity will be assumed to be zero to allow for an analytic solution, and the impact of this will be discussed later. In order for the resonance criterion to be met, the electron must travel from one plate, which will be assumed to be the lower plate at $x = 0$, to the other plate located at $x = d$ within a half-integer multiple of the RF period ($\frac{n\pi}{\omega}$) so that the subsequent emission will be accelerated back to the original plate. Applying these values and the relationship to the voltage $E_0 = V/d$ to Eq 3.3 and rearranging yields

$$fd = \frac{1}{2\pi} \sqrt{\frac{q_e V (2 \sin \phi + n\pi \cos \phi)}{m_e}}, n = 1, 3, 5, \dots \quad (3.4)$$

This is the expression for the frequency-gap width product, and it is a good indicator of the satisfaction of the resonance criterion. A similar factor will be used in the later when analyzing the coaxial power coupler to describe its ability to experience MP. The introduction of the integer n leads to various MP modes that are related to the transit time of electrons between electrodes. This will also be directly relevant to multipactor near the RP window, but that analysis will have additional complications to the modes as well. Three examples of trajectories that satisfy Eq 3.4 are shown in Fig 3.1 and represent three different modes of multipactor where there are one, three, or five half cycles between each collision.

The frequency-gap width product is useful in analyzing MP since it serves as a reduction of terms that more readily express when MP occurs. This is an exact solution to a purely hypothetical form of the phenomenon, but its application can be generalized to other cases of MP. Since the actual process of MP takes in many more factors than those considered to get Eq 3.4, the use of fd in predicting MP

will be mostly limited to predicting what variables can be used in the simulations. This will prevent excessive numbers of simulations from needing to be made to predict MP over a multitude of possible coaxial sizes, power levels, frequencies, etc., and a discussion of the usefulness of the related parameter ζ that is used later will be discussed after detailing the simulation process.

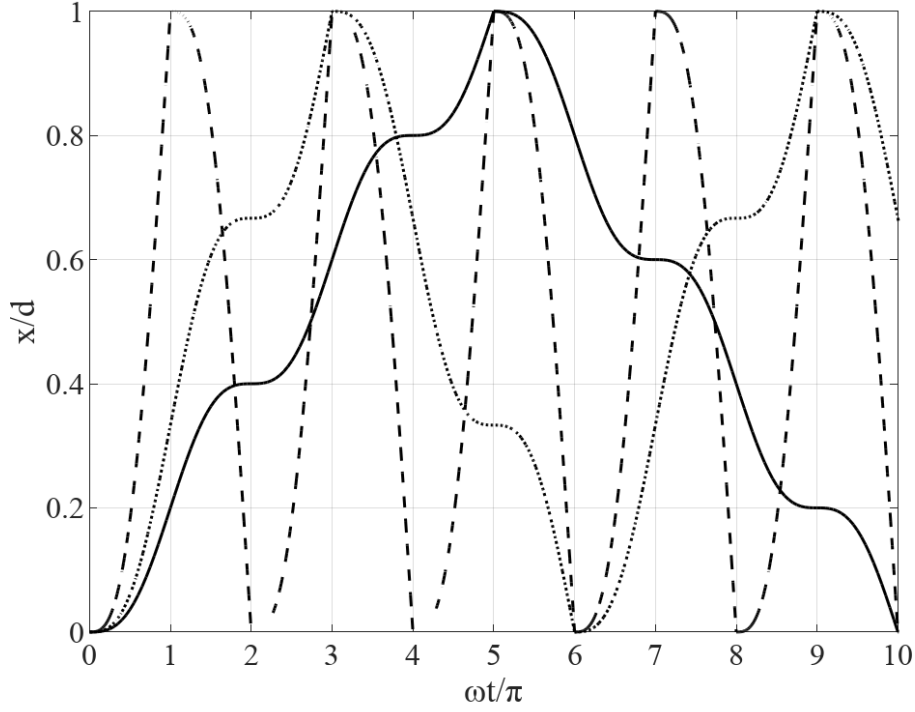


Figure 3.1: Sample trajectories for an electron in a parallel plate geometry emitted with zero velocity both initially and upon each impact. The abscissa denotes the number of RF periods, and the ordinate is the location between plate 1 ($x/d = 0$) and plate 2 ($x/d = 1$). The various trajectories are various multipactor modes that can occur.

3.2.2: Satisfaction of emission criterion

Using the same assumptions from the analysis of the resonance criterion, the emission criterion can also be discussed. In order for the emission criterion to be met, the energy of the electron must be between the cutoff energies, which correspond to the velocities v_1 and v_2 . The values of $v_0 = 0$ and $t = \frac{n\pi}{\omega}$ that were applied to meet the resonance criterion can then also be applied to the first derivative of Eq 3.3 to get the velocity of the electron upon collision. Once this has been done, the voltage can

then be solved for the cutoff velocities to reach the inequality

$$\frac{\omega dm_e v_1}{2q_e \cos \phi} \leq V \leq \frac{\omega dm_e v_2}{2q_e \cos \phi} \quad (3.5)$$

The emission criterion is met if that inequality holds true.

3.2.3: Non-ideal factors

The exact mechanisms of MP are generally more complicated than this, but these criteria serve as good examples to illustrate the MP process and its complexities. The possible resonance of the electron trajectories was illustrated by Eq 3.4, but this equation only holds true if $0 \leq \phi < \frac{\pi}{2}$ because above this value, the trajectory will reach the other electrode earlier in the phase than the predicted π/ω . This completely interrupts the repeatability of the trajectory and makes the completion of the resonance criterion unknown. This is further complicated by non-zero emission velocities. Whereas electrons emitted with zero velocity will not leave a surface if the fields oppose it, electrons emitted with a non-zero energy will leave the surface. This makes it possible for the trajectories with phases outside of the range $[0, \pi/2]$ to still have repeatable trajectories, although they become more complex with the initial conditions. Additionally, secondary electron emissions do not uniformly emit at the same velocity, so calculation of the frequency-gap width product to not experience MP is only truly valid if a range of velocities has been considered.

An example of the effect of varying velocities on resonance is shown in Fig 3.2. Three different emission velocities are shown with varying effects on the electron trajectory. It is possible that the slight change to the emission velocity will completely change the predicted trajectory, as happened with the lowest speed shown in Fig 3.2 by the dashed line. That trajectory is not repeated beyond the time shown, but instead is erratic and highly unpredictable. The other two emission velocities are more stable, with the median velocity (dotted line) repeating nearly exactly, and the highest velocity experiencing small changes to a mostly consistent trajectory. An important observation is made for the two higher velocities: Emissions can happen while the field is still accelerating the electron back toward the

surface, resulting in multiple collisions with the same surface before the polarity of the field changes. These electrons are termed to be “surface-bound” and will impact not only the stability criterion as displayed by the trajectories, but also the emission criterion as those collisions occurring in rapid succession will have low collision velocities that are likely to be below v_1 . The ramifications and treatment of surface-bound collisions will be discussed more in the numerical approach.

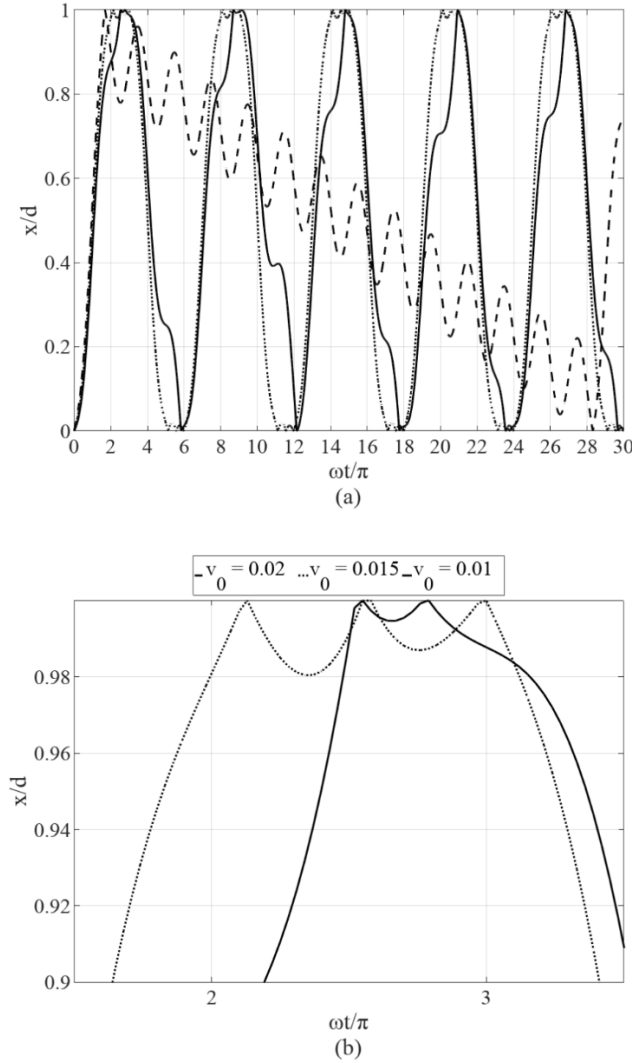


Figure 3.2: Sample trajectories for non-zero emission velocities. (a) the trajectory over 15 RF periods shows the broad and unpredictable effects that emission velocity can have on multipactor, and (b) a zoomed-in view of the trajectories of $v_0 = 0.02$ and $v_0 = 0.01$ shows how non-zero emission velocities can lead to multiple electron collisions while the electron is “bound” to the surface.

These irregularities do not necessarily preclude MP, however. Since the phenomenon is reliant on collisions producing multiple electrons being emitted back into space, if these collisions satisfy the emission criteria, the rapid growth of the electron population characteristic of MP can result, albeit not necessarily in an exponential form. This phenomenon has been recognized in both new forms of resonance [47] and as non-resonant modes [48] [49]. The presence of multipactor in spite of non-resonant trajectories demonstrates the difficulty in both identifying its presence, as well as its avoidance in RF systems. This is complicated even further by the introduction of non-zero emission velocities, which render Eq 3.4 and 3.5 themselves inaccurate. Of course those equations can be solved for a non-zero emission velocity, but the same issues that were just discussed pertaining to surface-bound electrons will persist, and new issues will arise from the stochastic nature of electron emissions whereby emission velocities will not be constant. All these considerations show that while the resonance criterion is useful in determining MP, it is neither straightforward to apply nor even necessarily relevant to the presence of MP in a system. This necessitates the simulation of MP to get an accurate prediction of the phenomenon.

3.3: Multipactor on dielectric surfaces

Another type of MP relevant to the RF window should be discussed before moving on to the coaxial geometry and simulation of MP. The presence of MP in the parallel plate was discussed in terms of a two-sided multipactor event, but historically a one-sided event has also been fundamental to MP. This one-sided MP is considered in the case of a dielectric surface with fields tangent to the window surface [32] [33] [49] [50] [51] [52] [53] [54] [55], as illustrated in Fig 3.3. This is similar to the case of the RF window but without the conductors and their subsequent effect on the fields. The dielectric is assumed to carry a positive charge which attracts the emitted electrons back to the surface, and the oscillation of the field imparts the requisite energy for secondary emission, and thus MP, to occur. There have been multiple studies on dielectric MP with various EM considerations, such as the

addition of magnetic fields or perpendicular components to the EM field, but the environment of the DTL coupler is considerably different than that of a dielectric in free space, so the exact mechanisms of dielectric MP do not need to be discussed further.

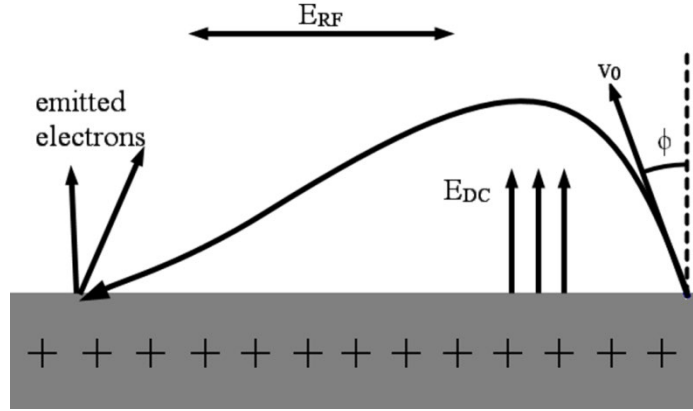


Figure 3.3: Illustration of classic single-surface MP on a dielectric. Positive charges accumulated on the dielectric (“+”) generate a DC electric field (“ E_{DC} ”) that restores electrons emitted at a speed v_0 and an angle of ϕ normal back to the surface. The RF electric field can then impart sufficient energy to the electron for subsequent emission events to occur.

3.4: Multipactor in coaxial lines

The analysis of MP near the RF window has many additional considerations from the baseline principles discussed. The simulation of MP first requires a discussion of the equations of motion with both the added complexity of the EM fields in the coaxial line. The coaxial line can also be characterized by a modification of the frequency-gap width described by Eq 3.4, and a general discussion of MP in a coaxial line without an RF window can be examined. Then the effect of the magnetic fields and their influence on electron migration along the axial direction will be discussed, with emphasis added on the influence of standing waves.

3.4.1: Equations of motion in cylindrical coordinates

The equations of motion can be discussed more generally from what was defined in Eq 3.2 to

include all of the nuances that can possibly arise in the system. First, while the effects of relativity should be negligible for the case of the DTL power coupler, this should not be generally assumed to be true for other cases which will be examined as a precursor to the RF window analysis. Relativity has been considered in some MP investigations [56] [57], so the equations of motion should be solved with it considered, and its effect discussed along with the benchmarks. The inclusion of relativity into the Lorentz equation is then

$$\frac{d\mathbf{p}}{dt} = \frac{d}{dt}(\gamma m_e \mathbf{v}) = q_e(\mathbf{E} + \mathbf{v} \times \mathbf{B}) \quad (3.6)$$

where \mathbf{p} is the four-momentum, γ is the Lorentz factor, \mathbf{v} is the three-velocity vector, and \mathbf{E} and \mathbf{B} are the electric and magnetic field vectors. While the fields in the coupler are more readily represented in cylindrical coordinates, the numerical approximation to Eq 3.6 can be found more easily in Cartesian coordinates. This conflict is resolved by converting the fields from cylindrical to Cartesian coordinates, then solving the Cartesian form of Eq 3.6, which is

$$\begin{aligned} \frac{d\gamma}{dt} v_x + \gamma \frac{dv_x}{dt} &= \frac{q_e}{m_e} (E_x + v_y B_z - v_z B_y) \\ \frac{d\gamma}{dt} v_y + \gamma \frac{dv_y}{dt} &= \frac{q_e}{m_e} (E_y + v_z B_x - v_x B_z) \\ \frac{d\gamma}{dt} v_z + \gamma \frac{dv_z}{dt} &= \frac{q_e}{m_e} (E_z + v_x B_y - v_y B_x) \end{aligned} \quad (3.7)$$

The right hand side of Eq 3.7 represents the acceleration of each respective component in the non-relativistic motion. The time derivative of the Lorentz factor γ can be applied to reach the equation that will be solved for using the numerical method discussed later, so that

$$\begin{bmatrix} \frac{\gamma^2}{c_0^2} v_x^2 + 1 & \frac{\gamma^2}{c_0^2} v_x v_y & \frac{\gamma^2}{c_0^2} v_x v_z \\ \frac{\gamma^2}{c_0^2} v_x v_y & \frac{\gamma^2}{c_0^2} v_y^2 + 1 & \frac{\gamma^2}{c_0^2} v_y v_z \\ \frac{\gamma^2}{c_0^2} v_x v_z & \frac{\gamma^2}{c_0^2} v_y v_z & \frac{\gamma^2}{c_0^2} v_z^2 + 1 \end{bmatrix} \begin{pmatrix} \frac{dv_x}{dt} \\ \frac{dv_y}{dt} \\ \frac{dv_z}{dt} \end{pmatrix} = \frac{q_e}{m_e \gamma} \begin{pmatrix} E_x + v_y B_z - v_z B_y \\ E_y + v_z B_x - v_x B_z \\ E_z + v_x B_y - v_y B_x \end{pmatrix} \quad (3.8)$$

There are some predictions about MP in a coaxial line that can be discussed before the solution to Eq 3.8 is found however. The work of Udiljak et al [38] used a number similar to the frequency-gap width product which they termed the “normalized gap width,” and found that analytic approximations

to the trajectories could be found and related to the normalized gap width. Their work was also supported by particle-in-cell simulations of MP (a method discussed in the simulation section), so the use of the normalized gap width was also used here. This can also generalize some results to various other coaxial line geometries that are beyond the specifics of the DTL. Generally, the definition of the normalized gap width is no different than the definition in Eq 3.4, but the voltage and arrangement of terms are slightly different.

3.4.2: Normalized gap width and standing waves

To find the expression for the normalized gap width, the expression for the fields must first be discussed. In general, there will be a forward propagating signal from the window toward the cavity and a backward propagating signal resulting from a reflection from the line terminus and the cavity emissions as discussed in the previous chapter. For now, only the transverse electromagnetic (TEM) mode is considered so that

$$\begin{aligned}\mathbf{E} &= \frac{E_0}{r} (\sin(\omega t - kz) + \chi \sin(\omega t + kz + \nu)) \hat{r} \\ \mathbf{B} &= \frac{E_0}{rc_0} (\sin(\omega t - kz) - \chi \sin(\omega t + kz + \nu)) \hat{\phi}\end{aligned}\tag{3.9}$$

This can then be rearranged to a single sinusoidal term with a modified amplitude and phase so that

$$E_r = \frac{E_0}{r} \chi_{eff}(z) \sin(\omega t + \nu_{eff}(z))\tag{3.10}$$

$$\begin{aligned}\chi_{eff} &= \sqrt{1 + 2\chi \cos(\nu + 2kz) + \chi^2} \\ \nu_{eff} &= \tan^{-1} \frac{\chi \sin(kz + \nu) - \sin(kz)}{\chi \cos(kz + \nu) + \cos(kz)}\end{aligned}\tag{3.11}$$

The standing wave modification of the amplitude χ_{eff} is then also a modifier of the voltage at a particular location. Expressing the voltage in terms of the power and characteristic impedance, the normalized gap is then defined to be

$$\zeta(z) = \frac{m_e(\omega d)^2}{q_e \chi_{eff}(z) \sqrt{P Z_0}}\tag{3.12}$$

It is apparent that the normalized gap width is dependent upon the electron's axial location, so this component of the trajectory must be addressed. The magnetic field will influence the axial motion

of the electron as seen in Eq 3.6, so the electron will generally not remain in the same axial location. For a traveling wave, it is apparent that the electron will move with the direction of propagation, but standing waves produce a less apparent motion. The standing wave will create a gradient in the magnetic field amplitude, thus generating a Miller-Gaponov force [38] [58] that lead to electrons accumulating in predictable axial locations, namely the magnetic field maxima. MP at the electric and magnetic field maxima have also been previously studied and compared to the results of the traveling wave, so their observations will also be used to benchmark the results of the simulations where Eq 3.12 is calculated for the locations of the field maxima.

A consequence of the migration toward the magnetic field maxima is that for conditions where the RF window is located between the electric and magnetic field maxima, the electrons can be accelerated into the window without any surface charge present on the window. This is a major deviation from the traditional mechanism of dielectric MP, so simulations are required to investigate the change to the phenomenon from what has been previously expected. Should the use of ζ prove to be a consistent parameter in standing wave conditions away from the window as described above, its use will be predicted to provide an acceptable reduction of parameters for those simulations. The specific concerns with the standing wave-RF window interactions are discussed in detail in the next chapter.

3.5: Simulation of multipactor

The simulation of MP is an arduous task requiring both the accurate simulation and interpretation of electron trajectories. There are many available software packages to analyze MP [31], but these have insufficiencies for the purpose of this work to analyze MP near the RF window, so a custom code was assembled. The first consideration to be made in creating the simulation code was to identify the numerical method to be utilized in the solution of Eq. 3.8, so these are discussed first to ensure that accurate electron trajectories are calculated. The simulation will also require a discussion

of the initialization of trajectories, both at the beginning and upon each collision with a surface. The electron trajectories must then be interpreted to determine if MP is present for the given conditions, and there are numerous possibilities to determine how the electron collisions with surfaces can produce the rapid growth of the electron population. The advantages and disadvantages of those methods will be discussed to defend the method that is utilized in the code, and the other factors that describe the mechanism of MP will also be discussed for their importance to understanding MP in the system and benchmarking the simulations.

3.5.1: Solving the equations of motion

The highly complex form of Eq. 3.8 requires a careful consideration of numerical schemes to find its solution. The equations of motion must be discretized in time so that for some time step, the position and velocity can be used to find the acceleration at the given time step i . This results in a generalization of Eq 3.8

$$M(\mathbf{v}^i)\mathbf{a}^i = \mathbf{F}(\mathbf{r}^i, \mathbf{v}^i, t^i) \quad (3.13)$$

where $M(\mathbf{v}^i)$ is the matrix of velocities and the Lorentz factor, \mathbf{a}^i is the acceleration, and $\mathbf{F}^i = q_e/m_e\gamma(\mathbf{E}(\mathbf{r}^i, t^i) + \mathbf{v}^i \times \mathbf{B}(\mathbf{r}^i, t^i))$. Because the dependence of the acceleration on the position and velocity is non-linear, an explicit time advancement method must be used. The two general classes of methods that are then available are multistep methods and predictor-corrector methods [27]. The multistep methods require the trajectory to be reinitialized upon each collision as will be discussed later, thereby introducing an additional bit of artifice to the simulation. This artificial initialization of two time steps upon collision would then have to be examined to ensure its effect is negligible. Conversely, the predictor-corrector methods use multiple iterations of the simpler Euler method at each time step to correct the errors that the constituent iterations carry. This means that the predictor-corrector methods need only the position and velocity at one time step to calculate the next times steps at the added expense of multiple calculations per time step, which is much more amenable to the

multiple collision-emission events that will occur during a simulation.

Within the broad class of predictor-corrector methods, the Runge-Kutta (RK) family of methods is well attested [27] [59]. The RK methods use a variable number of interstitial time steps to correct the time derivative values that are used to calculate the values \mathbf{r}^{i+1} and \mathbf{v}^{i+1} at a time Δt after the initial values of \mathbf{r}^i and \mathbf{v}^i . The calculation of both the interstitial and goal time steps are straightforward in that they use the first two terms of the Taylor expansion so that the function value at the time step considered ($i + s$) is found using the corrected time derivative k , i.e. $x^{i+s} = x^i + s\Delta tk$. The specific RK method will determine the number and times of interstitial time steps, as well as how the time derivatives are corrected. Three common methods use either two iterations (RK2) with the interstitial value calculated at either $\Delta t/2$ (midpoint method) or Δt (Heun's method) or four iterations (RK4), and they require less memory than some other RK alternatives, so these were considered for use in generating the simulation code.

The mathematics of these methods can be given a physical explanation. The midpoint method calculates the position and velocity at half of a time step, then recalculates the velocity and acceleration at that midpoint and applies them to the original position and velocities to find their new values at the end of the whole time step. Heun's method modifies this by using the original velocity and acceleration to advance the position and velocity by a whole time step, then using those values at the interstitial time step to find the new acceleration, and the corrected velocity and acceleration are then found to be an average of their original and interstitial values. The RK4 method builds on these same principles, advancing by the midpoint twice, then by the whole time step, and averaging all the k_1 interstitial values to calculate the final value.

The application of these RK methods to the electron trajectory requires splitting the position and velocity so that each is expressed only in terms of their time derivative so that

$$\frac{d}{dt} \begin{pmatrix} \mathbf{r} \\ \mathbf{v} \end{pmatrix} = \begin{pmatrix} \mathbf{v} \\ \mathbf{a}(\mathbf{r}, \mathbf{v}, t) \end{pmatrix} \quad (3.14)$$

where $\mathbf{a}(\mathbf{r}, \mathbf{v}, t)$ is found by solving Eq. 3.14. This is discretized for solution using RK methods by considering the interstitial time steps i_n so that

$$\begin{pmatrix} \mathbf{r} \\ \mathbf{v} \end{pmatrix}^{i_n} = \begin{pmatrix} \mathbf{r} \\ \mathbf{v} \end{pmatrix}^i + s_n \Delta t \left(\mathbf{a}(\mathbf{r}^{i_{n-1}}, \mathbf{v}^{i_{n-1}}, t^{i_{n-1}}) \right) \quad (3.15)$$

where s_n is the fraction of the time step that the interstitial values are calculated for. The position and velocity at the time step i_1 are simply their initial values. The final value of the time step is then

$$\begin{pmatrix} \mathbf{r} \\ \mathbf{v} \end{pmatrix}^{i+1} = \begin{pmatrix} \mathbf{r} \\ \mathbf{v} \end{pmatrix}^i + \Delta t \sum_n c_n \left(\mathbf{a}(\mathbf{r}^{i_n}, \mathbf{v}^{i_n}, t^{i_n}) \right) \quad (3.16)$$

where c_n is a modifier that weights the averages of the interstitials.

3.5.2: Initialization of electrons

The initialization of electron trajectories is the remaining issue to be addressed in the simulation of MP. This initialization must be done at the beginning of the simulation, as well as upon each collision-emission event. The simulation itself is initialized based on what is needed for the specific analysis and what is reasonable to expect in the physical system where MP is started by random electron emissions. The collision-emission events will have stochastically determined emission velocities based upon the Furman model to provide an accurate representation of the physical phenomenon.

In order to begin the simulation, a reasonable position, velocity, and phase of emission must be determined. The initial positions are commonly set by randomly assigning them within some region, say on a conductor surface and within one wavelength of the axial direction to ensure there is a sufficiently large number of trajectories being calculated to account for various MP initiations [13] [50] [56] [60] [61] [62] [63] [64] [65] [66]. This removes the large dependence on initial conditions that was observed in the parallel plate geometry and is sure to persist in the more complex coaxial geometry by simulating many possible emission locations and times to get an average response to the operation conditions. The position initialization can be improved on, however, by simply considering what is being investigated with the simulation and the physical implications of the initial locations.

The case being investigated in the simulation allows for the appropriate axial location to be found. For the benchmarks against the standing wave conditions, the electrons are expected to drift to specific axial locations, so these only need one initial axial location at the electric and magnetic field maxima, as long as these maxima are not in the vicinity of the RF window where unexpected window collisions might affect results. Similarly, electrons in the vicinity of the RF window will either be confined to be between the window and electric maximum, or they will somehow move past the electric maximum and still settle near either it or the magnetic maximum. Either way, these are two vastly different processes that will provide sufficient evidence of what occurs to allow accurate prediction of MP with the only necessary initial axial location being the window location. This is a different approach than what has been done by some previous studies, so the consideration of this initialization will be discussed with the benchmarks.

The physical implications of the initializations can also be utilized to strategically place the radial, and later azimuthal, positions. MP is started when some initial electrons are emitted from surfaces, so the initial placement of electrons in the simulation is on the conductor or window surface. The previously described use of randomly assigned positions does not describe this but instead represents a hypothetical spread of emission points and phases relative to the RF signal. A phase shift to the EM signal will instead be used to ensure that the response of the system to a range of instigating emission events is found. These phase shifts will range be in the range of $[0, 2\pi]$, so that even phases that would initially accelerate electrons back into the surface are accounted for as they are also capable of producing an emission event.

For the initial MP investigation away from the window, i.e. the benchmarks at the standing wave field maxima, the initial position will be at the outer conductor surface only, since this will accurately simulate both the classical two-sided and the one-sided MP mechanisms described earlier. For the window MP, a few radial positions will be evenly spaced between the conductors, with points at both window-conductor junctions included. For those conditions where MP is expected to be

confined to the region of the RF window, this will place the trajectories in the appropriate region, but if the MP does not follow predictions then this will still exemplify MP that can affect the window.

The velocities must also be initialized. A typical emission energy used throughout simulations is 2 eV [34] [38] [64], so this will be used to initialize the trajectories. The direction of the emission velocity will be directed normal to the surface, with the important caveat being that this direction is defined to be at a 45° to both surfaces at the window-conductor junctions. The radial and axial placements are illustrated in Fig 3.4 with the velocity directions also indicated. The azimuthal initialization for 3D simulations will be taken to be at zero unless otherwise necessary.

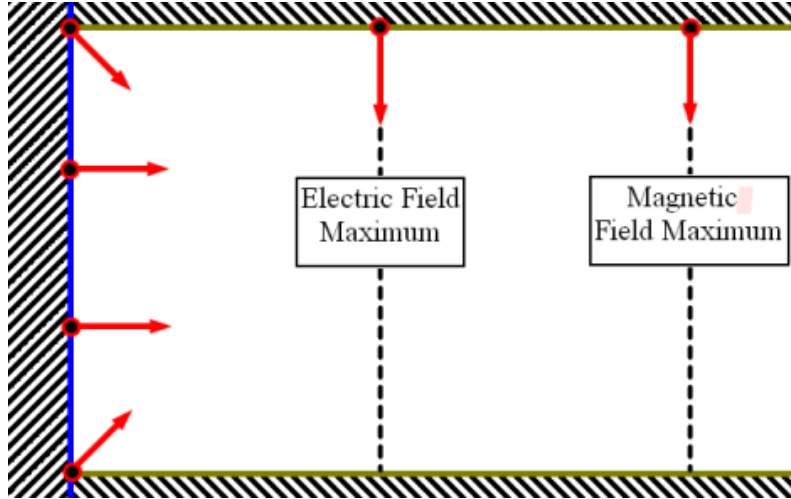


Figure 3.4: Emission points used in simulations. The left portion of the figure is the window location, and for the purposes of simulation this is set to be impenetrable. Those emission points set there are used for most simulations in this work as they are suited to investigating window MP, and a variable number of points might be used. The other points are used to investigate EMP and MMP with electrons emitted at those respective maxima. The arrows indicate the emission velocity direction, with no azimuthal component for 3D simulations.

The effect of these initializations should be minimal. While some MP software utilizes the so called “distance function” to determine if the electron drift in the axial direction affects results [31] [56], the use of the curated axial initializations negates the need for this metric. The additional effects of using the range of radial locations and phases can be investigated by considering the MP metrics for

each of these initializations to see if there is a significant difference. The initial velocities will not significantly affect results, as the subsequent collision-emission events are what will give a true response that is representative of the physical system.

3.5.3: Collision events

Adjustments must be made to accurately simulate what occurs during collision-emission events. The first consideration is the delay time between the collision and subsequent emission, which is on the order of picoseconds [45], and the time step will also be on the order of ps for the higher range of frequencies that will be simulated. This means the collision-emission event is instantaneous in the time frame of the simulation, so the position and time of the collision time step will be assumed to be the same as the emission event [67]. The emission will also be assumed to occur right on the surface, so the position of the emitted electron will be interpolated to be located at the surface as opposed to some depth into the surface as is likely to happen. This is only done for the final time step since the interstitial time step still needs to provide the correction, and additionally there is no issue in having an electron beyond the surface during the interstitials. A collision might occur where the position of the electron would indicate that a collision has occurred with both the window and a conductor, in which case the position is interpolated so that the collision occurs only on one surface. These considerations are illustrated in Fig 3.5.

The determination of the emission velocities is more complicated. First, the emission velocity is determined by the collision velocity, and the electron will likely collide with the surface sometime between time steps, meaning that the exact collision velocity is unknown. While the velocity could also be interpolated like the position was, the structure of the program would require additional calculations that are unlikely to outweigh the benefit, especially considering that the physical reality of the window surface not being as definitively located as it is in the simulation. The velocity before collision will be used instead. This velocity, in addition to the angle of collision calculated from the positions the time step before and the time step of collision, is then used to calculate both the emission velocity and an

MP metric as described later.

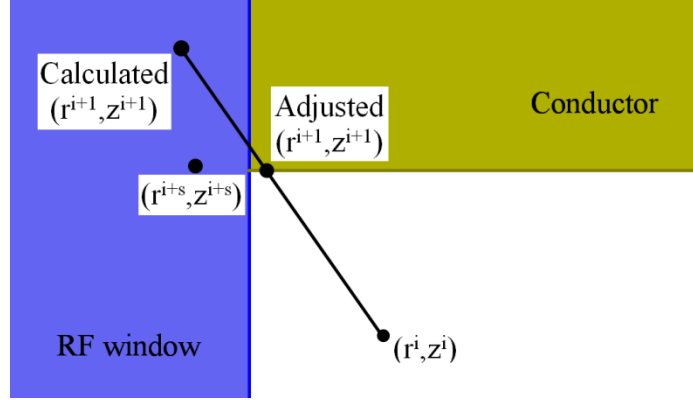


Figure 3.5: Illustration of collision event in simulation. Upon collision at time step i , the position is likely to penetrate some depth into the surface, so the position is adjusted to be on the surface by placing it in the linear path between time step i and the calculated time step $i + 1$. The interstitial time step $i + s$ remains unadjusted.

The emission velocity is then set to a stochastically determined value according to the Furman model. A random number from 0 to the total secondary yield of the collision is generated to first determine whether the emission mechanism is backscattering, rediffusion, or true secondary emission by comparing it to the emission yields of those different types (δ_{type}). The emission mechanism is set to rediffusion if the random number is less than δ_r , backscattering if the random number is less than $\delta_r + \delta_b$, and true secondary emission otherwise, and the emission energy can then be found using only one mechanism. This saves extraneous calculations, and the physical implications of this are perfectly valid for the backscattering and rediffusion mechanisms, where only one or the other will occur, if at all. Secondary emission can happen concurrently with those emission types, though, so using it exclusively is somewhat unphysical, but true secondary emissions are also dominant in systems that experience MP, so the effect of using it in isolation is not expected to be significant.

Once the emission mechanism has been determined, the emission energy that results in another randomly determined emission yield can be calculated. A new random value ranging from 0 to δ_{type}

is generated to isolate the energy calculation to the mechanism being considered. The emission energy is then calculated by considering a new form of Eq 3.1, where instead of integrating from 0 to the collision energy E_c , the integral instead goes to the emission energy E_e so that

$$\delta_{type}X = \int_0^{E_e} \frac{d\delta_{type}}{dE} dE, X \in [0,1] \quad (3.17)$$

where X is the random number. The function $d\delta_r/dE$ allows for Eq 3.17 to be solved analytically for E_e , but $d\delta_b/dE$ and $d\delta_{ts}/dE$ cannot be. Instead, these must be calculated with an iterative numerical solution. For the backscattered electrons, the emission energy is found by sweeping values of the right hand side of Eq. 3.17 by small increments of E_e starting at the collision energy until the difference between it and the left hand side of Eq 3.17 is $< 0.1\%$ of the goal value. This same approach was initially attempted to find the emission energy of true secondaries, but this was too computationally expensive, especially considering that this is the dominant mode of emission when MP occurs. Instead, the secant method was again applied with initial guesses used set to 1.25 and 15.3 eV for copper and to 5 and 50 eV for stainless steel. The results of using sample collision energies to generate a distribution of emission energies is shown in Fig 3.6, demonstrating that the concern with isolating the true secondary emission mechanism does not significantly affect the distribution of emission velocities.

The Furman model also prescribes emission angles to define the direction of the emission velocity. The angle normal to the surface θ_n is defined by a probability density of $\cos(\theta_n)$, so that the tangential component of the velocity is defined by a random number $X \in [0,1]$, and the normal component of the velocity v_n is then $v_n = \sqrt{1 - X^2}$. For 3D simulations, the tangential component of the velocity can then be broken down to two more components with a uniform distribution ranging from 0 to 2π .

3.5.4: Analyzing multipactor from trajectories

The metrics used to find MP must be defined in order to both extract information from the electron trajectories and finalize how they are calculated. The major concern is whether or not MP will occur

for given operation conditions, and there are two ways to do this in a simulation—generate and track the electron population [68] [69] or record collision information of only one representative “macroparticle” and apply MP principles to that information [31] [46] [63] [65] [66]. These each have advantages and drawbacks as will be discussed, but they also are not the only sources of pertinent information. In order to estimate how an electron population could build with time (using the latter two methods above), the time between collisions must also be known. It is known that the MP mechanism

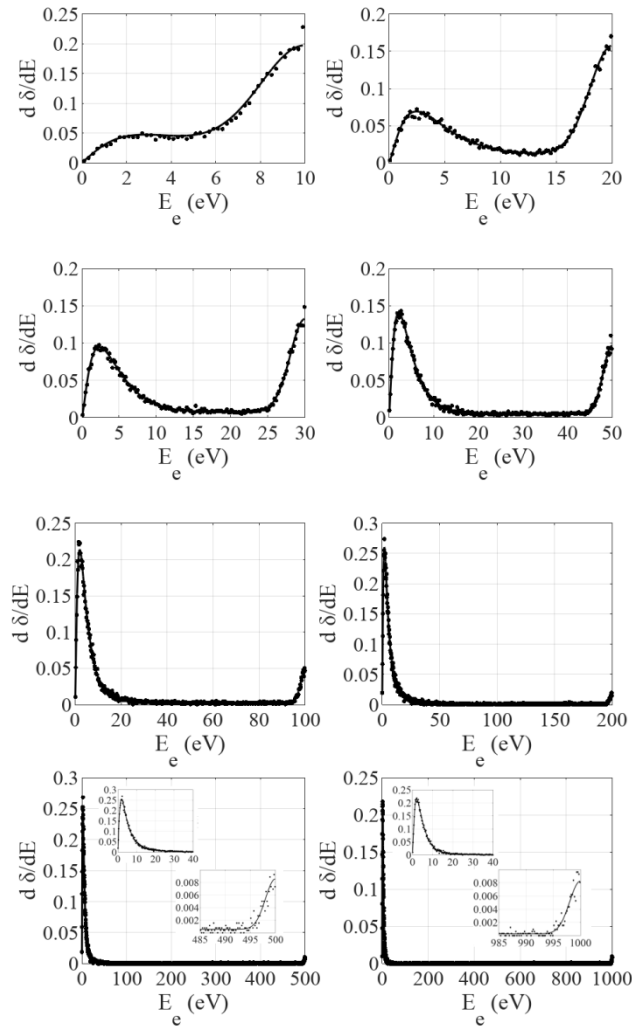


Figure 3.6: Sample emission energy distributions for various collision energies. The collision energies used are the maximum energy of each plot.

is an important consideration to understand and mitigate the phenomenon, so the locations of electron locations will be important, particularly in discussing window collisions, which is the particular concern for the DTL coupler being analyzed. Related to that is the question of where those collisions occur over time, as described by the previously mentioned distance function.

The tracking of an actual electron population over the course of the input signal has the least artifice and is therefore considered to be the best indicator of whether or not MP occurs [70]. The electron trajectories are calculated as described, but upon collision the stochastic emission of particles is modified so that a variable number of electron trajectories is initialized. The number of trajectories is calculated stochastically based on an emission model, with zero trajectories being possible. An initial electron population must be started similar to what has already been described, but the population should be in the tens to hundreds of electrons to ensure that any electrons absorbed into surface upon collision will not artificially preclude MP from being observed. The occurrence of MP is then straightforward to observe as the electron population changes, with large, exponentially growing populations being typical of the resonant MP phenomenon, and the other information relevant to MP can also be recorded with ease.

The main disadvantage of this method is the computational expense required. Each electron trajectory requires many calculations per time step to calculate first the time advanced position and velocity, then the updated EM fields, and finally the correction of position and velocity, and all this is in addition to the storage requirements of the multiple variables per electron. While this is not significant for a single electron being tracked, should multipactor occur, the population will quickly reach into the thousands and millions of electrons, and simulations become impossible to continue. This can be utilized to recognize MP, and the simulation can be stopped if this is observed, but the definition of these MP conditions can be difficult to accurately apply.

Simulation using CST Studio Suite uses this method and has been used as a reliable predictor of MP [68] [69]. The advantage of using CST for MP analysis is that the EM simulations that were

discussed in chapter 2 can also be incorporated into the trajectory calculations using the particle-in-cell (PIC) method. PIC simulations are a broad class that extend beyond CST and are commonly used in plasma physics. The same principles of a FDTD method are applied, and the fields at the fixed grid points can then be interpolated to electron positions and the trajectories thus advanced. This method also allows for the effect of the electron charge to be incorporated into both the EM calculations and the trajectories of neighboring electrons. The effect of MP can be seen in the change in the electron population, and the current and power of both colliding and emitted electrons is recorded for each component.

The limitation of the computational requirements is apparent when trying to simulate MP near the RF window, however. CST does have some parameters that can be set to detect when MP has occurred, and these relate to the expected exponential growth of the population. However, attempts to use these cut-off parameters proves difficult, with CST frequently failing to recognize MP before the computational memory is completely consumed. This is especially problematic in analyzing a wide range of operating conditions, where the specific population growth and the MP mechanisms will change, making the cut-off of MP impossible to predict, and so analysis cannot be parameterized. CST can however, provide some further benchmarks, particularly in regards to window collisions, which have not been previously considered and are especially difficult to measure experimentally.

The alternative to calculating the entire electron population is to instead use only one representative trajectory that provides information on MP indirectly. This is the method that has generally been outlined above, with only one electron being reemitted into space according to the Furman model. One interpretation of the results is to calculate the enhanced counter function [13] [31] [56]. This parameter considers when collisions occur, and should this be when the EM fields are such that the electron is accelerated back towards the surface, the enhanced counter function for that trajectory is set to zero. This is a stringent enforcement of the resonance requirement, and because MP has already been shown to occur even if there is a failure to meet that criterion, it is apparent that the

enhanced counter function can miss conditions that experience MP. This metric has been successfully used by several commercially produced codes, so it is not entirely unreliable, but it does lack nuance and the ability to more carefully consider factors that will lead to MP.

The other interpretation that is applied to the macroparticle method is to simply adjust the mass and charge of the electron based on the number of emitted electrons [13] [34] [46] [61] [63] [65] [70]. The ratio of charge to mass for this macroparticle will remain constant, so the equations of motion are still applicable, but the predicted population can be tracked throughout the simulation. Because the secondary electron emission yield δ is defined as the average number of electrons emitted per electron collision, the electron population p at collision i will be

$$p^i = p^{i-1} \delta^i \quad (3.18)$$

Alternatively, the logarithm of Eq 3.18 can be taken so as to avoid overflow errors. The value of p to start is unimportant as the growth of the population is what is relevant to MP, and so by setting $p^0 = 1$, the electron population at the end of the simulation will be directly indicative of MP.

A comparison of these three different methods is shown in Fig 3.7. The counter function, as expected, only has narrowly defined bands where MP would be expected to occur, and the detection of MP becomes more difficult for higher values of ζ that correspond to higher MP modes. The electron population however, has wide regions of ζ that experience a high population growth, and this method is generally trusted over the counter function because of its lack of artifice. The electron population was capped at 5000 electrons, since conditions reach that number through MP and exceeding that population might have been too computationally expensive. The macroparticle method that has been selected agrees fairly well with the electron population with regions of ζ experiencing MP typically agreeing. The most significant deviation from the population is the range of voltages that experience MP, but the calculation of these results were preliminary, so a more rigorous benchmarking of simulations is discussed later.

There are other metrics by which the mechanism of MP can be known as well, and related to

the population is the time between collisions. The modes of MP were described for the parallel plate and coaxial line without a window, and these are typically related to the number of cycles between collisions. That makes this parameter useful in describing the MP mode for both benchmarking simulations as well as for understanding the potentially novel modes of MP generated by the RF window. However, the issue that was introduced by non-zero emission velocities in the parallel plate geometry produces new complexities when trying to calculate this.

3.5.5: Non-zero emission velocities

When an electron is emitted with a non-zero velocity from a surface, it will leave that surface for some time no matter what the force is accelerating it back to the surface. If the initial collision-emission event occurs early enough in the portion of the RF cycle where acceleration is toward the surface, there can be several collision-emission events before the electron is ultimately accelerated from the surface, effectively binding the electron to the surface for some time. While these surface-bound collisions affected the resonance criterion, the calculation of the electron population is not dependent on that criterion being met in this macroparticle approach. As such, these collisions do not present a problem in calculating the electron population, but they do raise issues in considering the other MP metrics, the averaging of the MP metrics, and the specifications of the simulation.

The first issue that must be addressed is whether the surface bound collisions should be differentiated from initial collisions with a surface. The identification of surface-bound collisions will require more conditions to be included in the simulation, making it preferable to treat all collisions the same. However, the simulation run time is based on a goal number of collisions, so should the surface-bound collisions be counted toward that goal number, there could be significant effects on the results, because the full picture of MP, particularly for the predicted non-resonant modes, might take time to develop.

Indeed, when preliminary simulations were run, there were differences in the electron populations, time between collisions, and percentages of collisions occurring on particular components

when all collisions were counted toward the goal number of collisions. Because the exclusion of surface-bound collisions leads to longer simulation times, these results should be trusted over the inclusion of those collisions. The percentage of collisions occurring on the inner conductor for the range of frequencies examined in those preliminary simulations was expected to lead to two-surface MP. Approximately 50% of collisions should have occurred on the inner conductor, which was true of the exclusion of surface-bound collisions, but their inclusion resulted in the percentage of collisions occurring on the inner conductor being higher than 50% for low power levels, and less than 50% for higher power levels. Because of this, the surface-bound collisions should be identified and excluded from counting towards the total number of collisions.

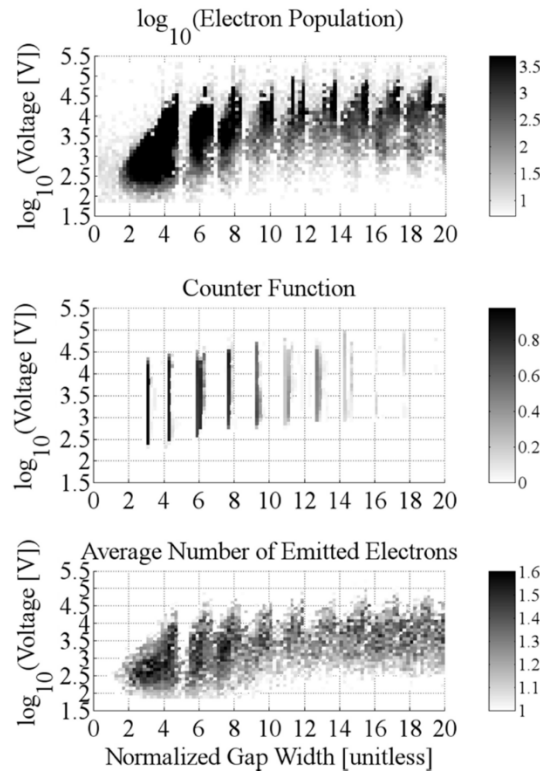


Figure 3.7: Comparison of multipactor using three different simulation techniques. The raw electron population (top), enhanced counter function (middle), and average secondary emission yield (bottom) were calculated for a coaxial line of the dimensions used in the DTL. The normalized gap width was modulated using various frequencies.

The next issue is how surface-bound collisions should be included in the calculation of MP metrics. By excluding them in the number of collisions to simulate, the electron population will not be directly affected, but it should be pointed out that they are still allowed to occur. For a metric like the enhanced counter function (ECF), conditions leading to surface-bound collisions would exclude the possibility of MP, but the macroparticle method is used because it is known that there is non-resonant MP that the enhanced counter function misses. So when surface-bound collisions occur, the population will likely decrease because those collisions will be of a similar energy to the stochastically determined emission energy, which is typically below the emission criterion energy ν_1 . Allowing the surface-bound collisions to affect the population in this natural manner will then effectively account for the resonance criterion. It will be beneficial to average the population so that a metric that does not rely on simulation specifics can be compared across many different scenarios [15] [63]. This average will be taken with the inclusive collision count, although the exclusive collision count will also be recorded in case averaging over these collisions is preferred.

A comparison of the emission energies is shown in Fig 3.8. The constant emission energy of 2 eV results in the normalized gap widths producing varying values of $\bar{\delta}$ by power level, and the range of the normalized gap width where MP occurs is also smaller than the stochastic emission velocities. This illustrates the importance of properly simulating the stochastic emission that occurs in collision-emission events. The difference between the exclusion and inclusion of the surface-bound collisions on the determination of stochastic velocity is also demonstrated in Fig 3.8. While their inclusion is more indicative of the physical events, there is not a significant difference between calculating a new emission energy upon every collision and only calculating a new emission energy only upon non-surface-bound collisions (selective stochastic emission in the figure). The most significant difference between these two methods is for the high power levels on the order of 10 to 100 MW, which is beyond what is applicable to the DTL coupler, so the surface-bound collisions will not be included in the stochastic emission calculations of emission energy.

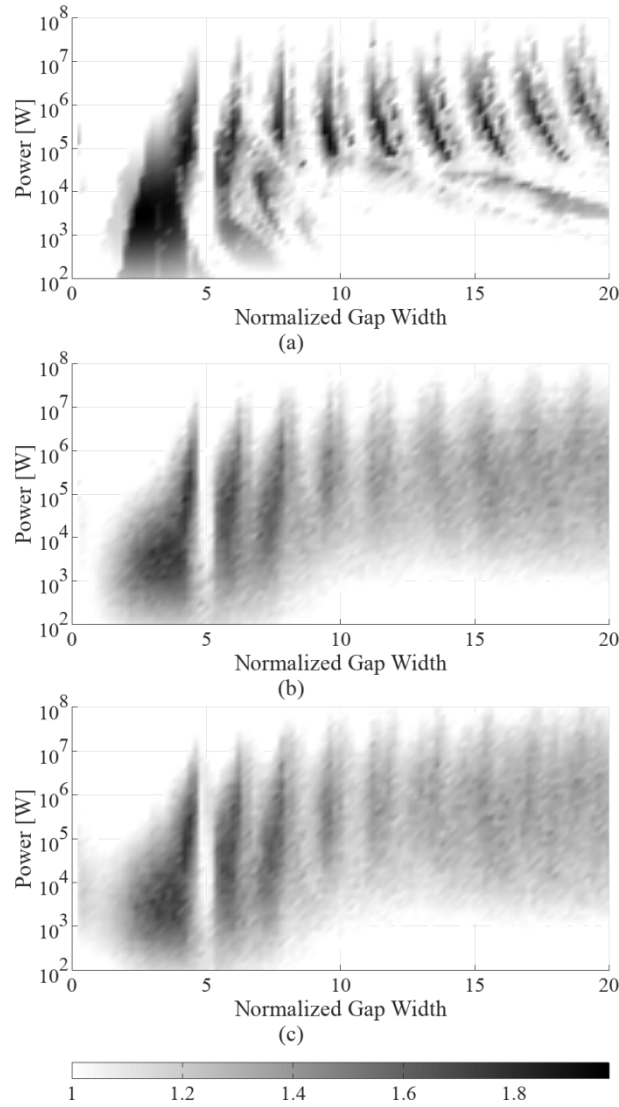


Figure 3.8: Secondary emission yield of DTL coupler using various emission velocities. The constant emission energy of 2 eV (a), emission energies stochastically calculated only for the initial collision of bound electrons or non-bound collisions (b), and stochastically determined emission energies upon every collision (c) are all shown.

Because the surface-bound collisions do play an important role in determining the electron population, the time step should be small enough so that they are included. If the time step is too large, the electric field might accelerate the electron back to the surface before it even has a chance to leave, and as a result the electron population will not be properly modified. To ensure this is the case, the time step can be found assuming that the acceleration is nearly constant between emission and the surface-

bound collision. Using the amplitude of the electric field E_0 , the time step must meet

$$\Delta t < \frac{2v_e}{FE_0} \quad (3.19)$$

where v_e is the emission velocity, and F is some factor that would set the number of time steps it would take the electron to return to the surface under these stringent conditions. This will only exceed the previously defined time step for high power levels, but it is good to ensure that any surface-bound electrons will sufficiently affect the population calculations.

Finally, the time between collisions is greatly affected by the exclusion of surface-bound collisions. The time that an electron is in flight between collisions is found by recording both the time of collision and the time that the electron is both off the surface after having collided with it and being accelerated from the surface. This time will be recorded in RF periods to be independent of the frequency being considered, and the summation of all flight times will then be divided by the exclusive collision count. This most closely matches the theory, allowing the time between collisions to represent the MP mode. The collisions on each component will also exclude the surface-bound collisions for this reason.

3.6: Simulation benchmarks

The simulations can now be benchmarked against previous work to determine their legitimacy in predicting MP. The first benchmark is to compare against previous theoretical work, such as that of Udiljak et al. [38], followed by experimental data. Then the effect of ξ on various coaxial line sizes is analyzed to ensure consistent results, and various other parameters will also be adjusted to observe the sensitivity of the simulations to them. Finally, the effect of standing waves is compared to previous studies to ensure accurate employment of ζ in those simulations.

3.6.1: Coaxial lines of varying impedances

The predicted MP mechanism will differ by characteristic impedance of the coaxial line, with

low impedances producing mostly two-sided MP and higher impedances producing mostly one-sided MP on the outer surface of the conductor. To that end, 25Ω and 50Ω lines were analyzed, and the results are shown in Fig 3.9.

These lines match the predicted results fairly well, with the regions of the normalized gap width that experience MP being significantly wider than the analytically determined regions as expected. The 25Ω line experiences only two-sided MP, and the stochastic emission velocities stretched the multipacting regions of the normalized gap width to essentially be continuous and difficult to match to the analytically predicted regions. The voltage ranges at the predicted ζ values did match fairly well however, and the upper range of the voltage that meets the cutoff of $\bar{\delta} > 1$ for MP to occur indicates that the mechanisms are roughly following the prediction. This is seen by that upper cutoff voltage only meeting the predicted voltage range at the corresponding normalized gap width values, and decreasing between those gap width values. Those decreases indicate that the MP mechanism is a result of the non-zero emission velocities, and the lower range of voltages does not experience the same fluctuation as the emission velocity is dominant over the voltage at these lower values.

The higher impedance of the 50Ω line also matches with the analytic approximations. The key difference between this and the 25Ω line is that the MP mechanism changes from being primarily a collision sequence between the two conductors to collision only occurring on the outer conductor. This disparity between the two impedances is due to the change in the electric field with the radius, which forces electrons to the outer conductor, so the larger impedance has a greater variation in the electric field from the inner to outer conductor and thus more electron collisions with the outer conductor. The two-sided MP is still seen in Fig 3.9 at around $\zeta = \pi$, but this is the only two-sided mode present. The single-surface MP mechanisms are dominant for $\zeta > \pi$, and the agreement with the analytic predictions is still good, but with more noticeable variations. The range of the normalized gap width is still broader due to the increase of non-resonant MP, and the value of $\bar{\delta}$ tends to be the highest right at the values predicted analytically, particularly for values of $\zeta < 10$.

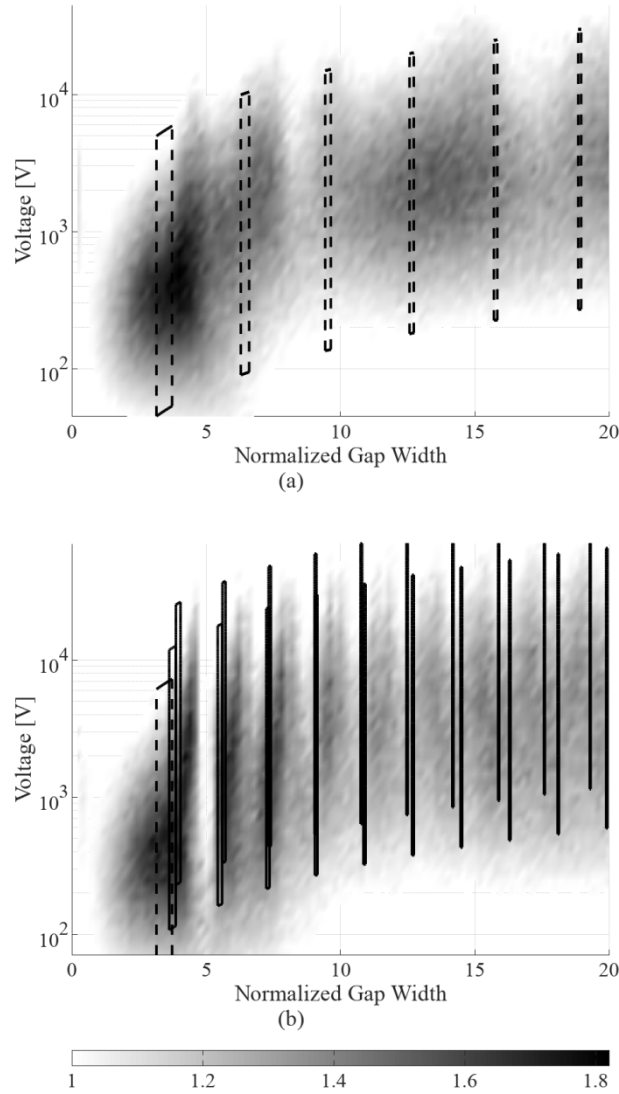


Figure 3.9: Comparison of the secondary emission yields (unitless) of the 25 Ω and 50 Ω lines with the analytic predictions. Dashed line boxes indicate regions of two-surface MP, and solid line boxes are regions of one-surface MP.

Above this, the differentiation between modes is less clear, but the presence of MP is still indicated by values of $\bar{\delta} > 1$. Similar to the 25 Ω line, the upper range of the voltage for which $\bar{\delta} > 1$ also fluctuated in accordance with the analytically predicted distinct modes, but those modes were not distinct in the simulation. The range of voltages also did not match as well as the 25 Ω line, with the upper and lower voltage cutoffs being well below the predicted threshold at the MP values of ζ . Heuristically, this is because the non-zero emission energies will make the electrons collide with

surfaces at a higher velocity shifting the voltages to lower values in order to experience MP. Additionally, the oscillations in the upper cutoff voltages that were observed in the 25Ω line also occurred for 50Ω , but the higher voltages occurred at slightly higher values than predicted. This is likely also due to the non-zero emission velocities, as it can be observed in Fig 3.8 that even the slight increase to 2 eV emission energies can shift MP to occur at higher values.

3.6.2: Experimental benchmark

The simulation can also be benchmarked against the available experimental results. The Tesla Test Facility (TTF) has a half wavelength window in a coaxial line with which to compare the simulation results. The effect of MP was measured in that line with an electron probe placed on the outer conductor near the window by Devanz, and they similarly compared their calculations to the electron probe signal. This line is 50Ω with an outer diameter of 61.6mm, and they used a 1.3 GHz signal of varying power levels to examine the power levels at which MP occurs.

The comparison with the secondary electron emission yield is shown in Fig 3.10, and generally there is good agreement between experiment and simulation. The peaks in the calculated values of $\bar{\delta}$ occur at approximately the same power levels as the experimental and numerical work of Devanz, and the relative strength of those peaks is also comparable to their results. The greatest difference is that no MP was observed below 300 kW, whereas the simulation did have elevated values of the secondary emission yield at these power levels. One contributing factor to this disagreement is that the time between simulations was not considered, and for those lower power levels, there will be more RF cycles between collisions. This means that there will be fewer collisions, and thus fewer electrons generated, in a given time period. However, this alone might not account for the lack of MP in the regions where the simulation predicts it if the pulse time is much longer than the RF period, which it almost certainly will be for a GHz range frequency. Another contributing factor then is that the electron population must be initiated for MP to be generated, and the low powers might not produce the right conditions to initiate MP at all. Still, it is also possible that the location of the electron probe used to detect MP might not be

optimal for these lower power levels, and MP might have simply been missed. Fortunately, the simulation will at least provide a conservative estimate that does not miss MP that was otherwise present experimentally, so designing the DTL window to operate with $\bar{\delta} < 1$ will likely avoid MP altogether.

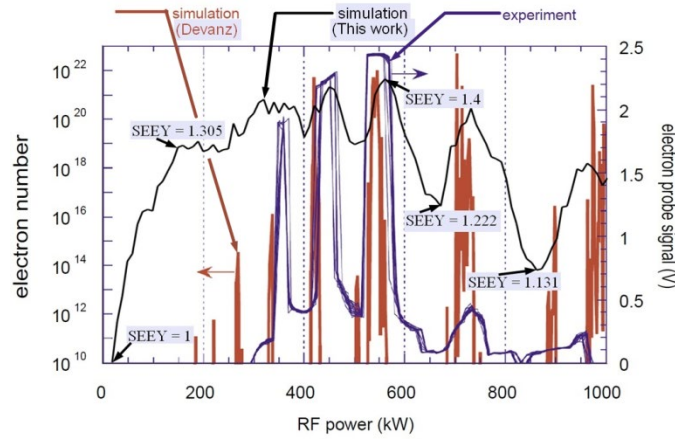


Figure 3.10: Comparison of the average secondary emission yield with experimental results and simulations by Devanz of the TTF geometry © 2019 IEEE.

3.6.3: Normalized gap width

The normalized gap width has been demonstrated to be a regular indicator of high values of $\bar{\delta}$, but the normalized gap width in the simulations was modulated by changing the frequency, which is not possible in the DTL operation. Changes can instead be made in the DTL by modulating the power or the coaxial size. As the coupler model in the previous chapter demonstrated, the coaxial line at LANSCE has various diameters which could provide useful benchmarks to see how the normalized gap width is affected by size changes. To that end, the same calculations were carried out with those other radii, and the results can be seen in Fig. 3.11. There is no discernable difference in the results that used the radii near the window, at mid-coupler, or near the accelerator cavity, meaning that the normalized gap width was very effective in reducing the number of factors that need to be considered in the calculations. The values of the normalized gap width for a set frequency of 201.25 MHz and a range of

power levels are also illustrated in Fig 3.11 as a line. The normalized gap width changes for both power levels and conductor radii, so these values can be adjusted to change the effect of MP on the system. The experimental results also showed a similar change in the normalized gap width with power level, as evidenced by the presence of peaks in Fig3.10.

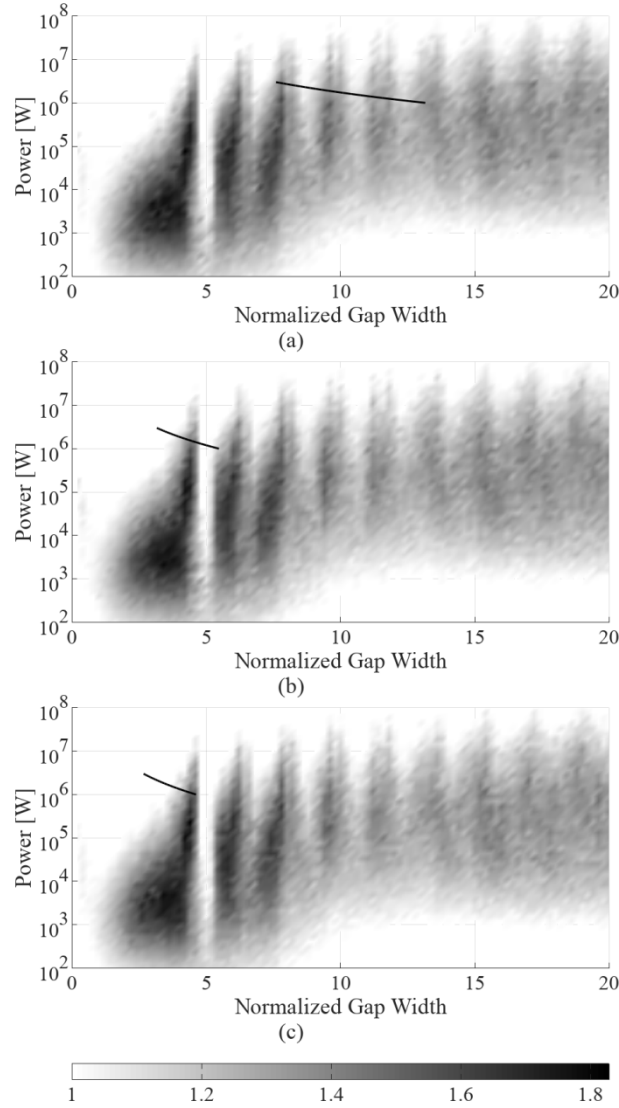


Figure 3.11: Secondary emission yields for the DTL coupler radii at the segments near the RF window (top), midway between the RF window and the accelerating cavity (middle), and near the accelerating cavity (bottom). The value of ζ for the input frequency of 201.25 MHz and power levels ranging from 1 MW to 3 MW is also shown.

3.6.4: Miscellaneous factors affecting simulations

The sensitivity of the MP metrics to several other factors should also be considered. First, it is obvious from the discussion of the time advancement scheme and the relevant numerical stability that the time step will have a significant effect on the electron trajectories and thus the metrics used to examine MP. To that end, several time steps defined in relation to the RF period were used, and the results of the secondary emission yield are shown in Fig 3.12. The smallest time step of $\Delta t = T/20$ had significantly different values of $\bar{\delta}$ than the two smaller time steps, particularly for higher power levels. This is expected for such a large time step, but it illustrates the lower limits of what can be used in the simulation. There were also differences between the time steps of $T/100$ and $T/500$, but overall these two time steps were not completely dissimilar, and the most significant effect of the increased accuracy was that some higher power levels and lower ζ values experienced MP for the $T/100$ time step but not the $T/500$ time step. Since $\Delta t = T/100$ provides accurate to conservative results, this time step will be sufficient.

Whereas the benchmarks so far have considered only the secondary electron emission yield, the other metrics should also be discussed. All of the considerations discussed so far have not have significant effects on the component impacts or the time between collisions. The percentage of collisions occurring on the inner versus outer conductors was also considered in the analysis of the 25 Ω and 50 Ω lines to confirm that the regions experiencing two-sided versus one-sided MP had the respective impact percentages of approximately 50 % and 100% on the outer conductor. This held true for the various radii examined corresponding to different axial locations along the coupler and for the various time steps discussed.

There are two other factors to consider however. The first is the effect of relativity, which did not show any appreciable differences. This is not unexpected from rough calculations corresponding to the DTL, but there were also no changes at the more extreme values of power or normalized gap width. The other effect is the simplification of the model to be two dimensional. While this is an acceptable

simplification based on the TEM mode considered in the line, there are real world factors that make the three dimensional simulation more accurate. Firstly, there can be some deviations from the ideal TEM mode fields. This can be modes scattered from the window, azimuthally varying charges on the window, or the effect of harmonics in the input signal as discussed in the previous chapter, but these effects require significant considerations and as such will be discussed later where appropriate.

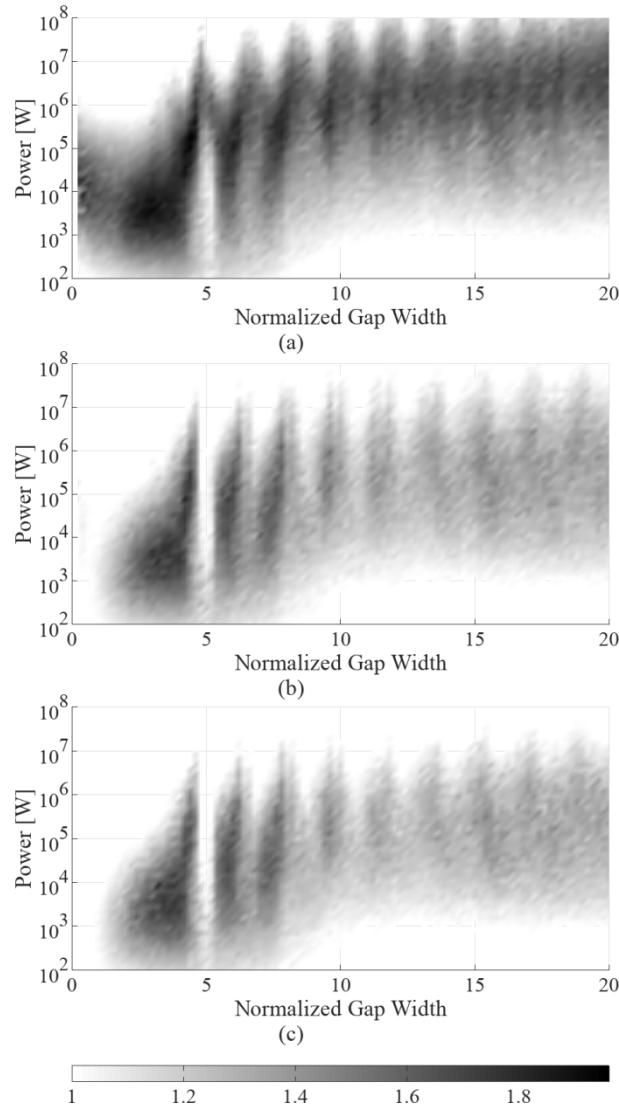


Figure 3.12: Comparison of secondary emission yield for varying numbers of time steps per RF cycle for the DTL geometry near the RF window.(a) $\Delta t = T/10$, (b) $\Delta t = T/100$, and (c) $\Delta t = T/500$

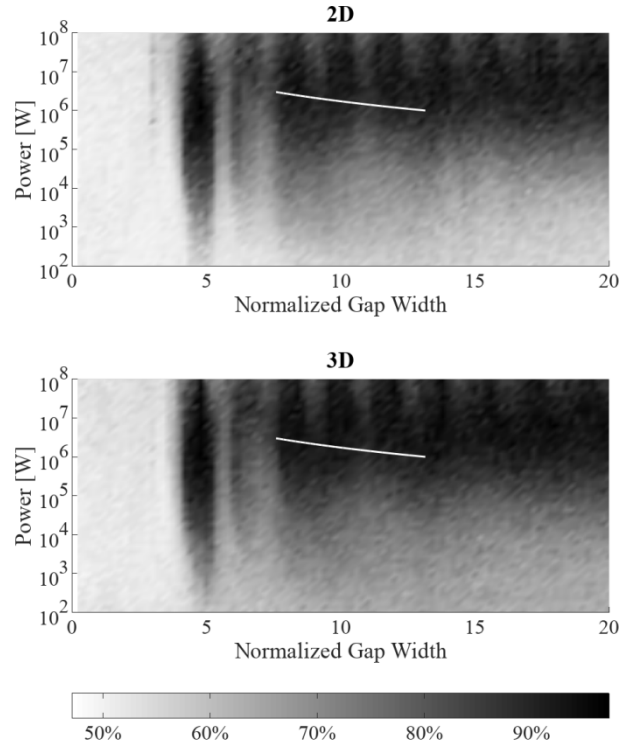


Figure 3.13: Comparison of the percentage of collisions occurring on the RF window for 2D and 3D simulations.

Even when considering the TEM mode, real world emissions can have a velocity component in the azimuthal direction, thereby changing the trajectory to a three dimensional one. The effect on the simulations is that the radial component of the emitted electrons is slightly reduced, but this was apparently compensated by the stochastic nature of the emission velocities in the two dimensional simulations as there was no discernable difference between it and the three dimensional simulation in terms of the secondary emission yield or the time between collisions. There was, however, a slight difference in the percentage of collisions occurring on the outer conductor as shown in Fig 3.13, with more collisions occurring in the three dimensional simulation for normalized gap widths above $\zeta \approx 4$. This is heuristically explained by possibility of electrons being emitted in the direction of the outer conductor by the new azimuthal component of its emission. The effect could also influence the percentage of collisions occurring on the window, and so full dimensionality is warranted in the analysis

of MP near the RF window, but two-dimensional simulations will also be instructive. Similar to Fig 3.11, the possible normalized gap width-power combinations within the DTL are indicated by a line in Fig 3.13 (this instance has a white line for clarity), and this element of the figure shows that the window collisions can increase from 2D to 3D simulations for the DTL as well.

3.6.5: Signal reflections and standing waves

Analysis of standing wave conditions is also necessary to understand the effects of the addition of a reflected signal. The Gaponov-Miller force that leads to electrons being generally confined to the electric and magnetic field maxima has already been discussed, and the effect of standing waves in a coaxial line has also been previously established [57] [69], providing an additional benchmark. Somersalo et al [56] calculated the enhanced counter function for a fixed frequency and geometry over several values of the reflection coefficient and power levels to find that MP at the electric field maximum (termed EMP) occurred at nearly constant voltages in relation to the reflection coefficient. That is to say, as the reflection coefficient got stronger, the power level where MP occurred was inversely proportional to the effective magnitude χ_{eff} . While they stated that MP at the magnetic maximum (termed MMP) did not follow this same heuristic explanation, the plot relating the enhanced counter function to the power and reflection coefficient demonstrated that this disagreement was not substantial.

So in analyzing the EMP and MMP, the use of χ_{eff} to calculate the normalized gap width should result in secondary electron emission yields that are consistent across the ranges of voltage and ζ with changing reflection coefficients. MP was analyzed with initial emissions at the electric and magnetic maxima and three sample values of the reflection coefficient, $\chi_b = 0.33$, $\chi_b = 0.66$, and $\chi_b = 0.99$. The results are shown in Fig 3.14. With the exception of MMP at $\chi_b = 0.99$, the secondary emission held consistent values across the normalized gap width but not across the voltage. Instead, the EMP showed the secondary yield to fluctuate as the reflection coefficient increased, particularly for values above 10 kV. Similarly for MMP, the upper range of voltage where $\bar{\delta} > 1$ both slightly decreases

and varies less with ζ as the reflection coefficient increases to $\chi_b = 0.66$. These deviations in the MMP case are not completely unexpected as the previous work also did not show them to match the heuristic prediction perfectly.

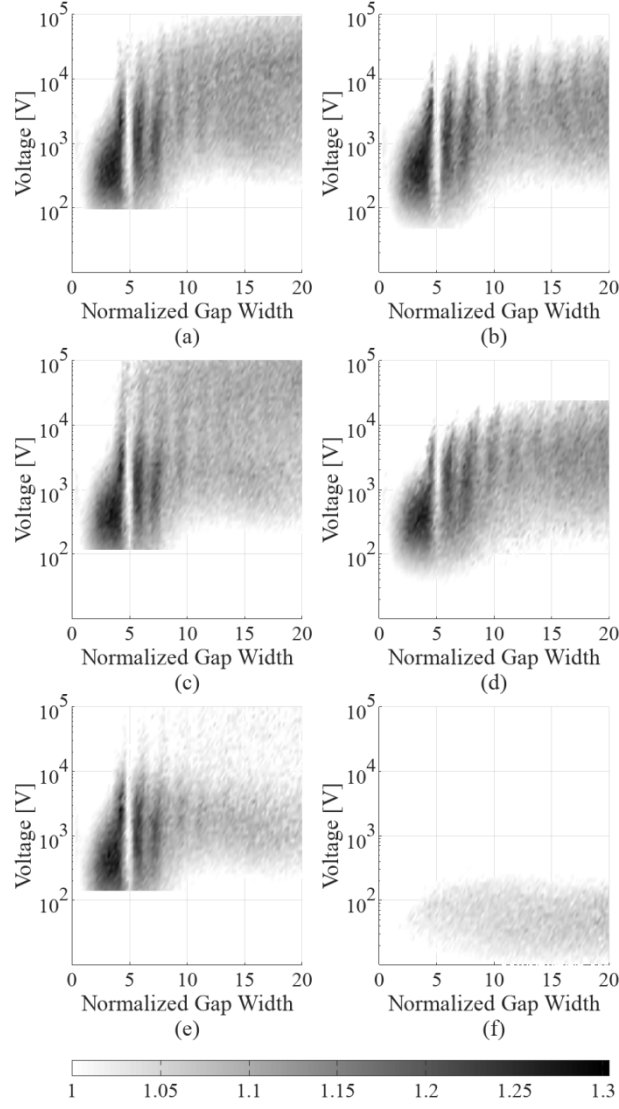


Figure 3.14: Secondary emission yields for emission points at the electric maximum (parts a, c, and e) and at the magnetic maximum (parts b, d, and f). Reflection magnitudes used are 0.33 (parts a and b), 0.66 (parts c and d), and 0.99 (parts e and f).

The most likely source of these deviations is probably the non-perfect confinement of electrons

to the axial locations of the electric and magnetic field maxima. The voltages shown in Fig 3.14 were calculated from the input power using χ_{eff} as defined in Eq. 3.11. The value of χ_{eff} depends on the axial location, so if electrons stray from the electric or magnetic field maximum too much, the calculated values of the voltage will be inaccurate. This is the case with the MMP for $\chi_b = 0.99$. This case was recalculated to record χ_{eff} throughout the trajectories, and when its average value was applied to re-evaluate the voltage and normalized gap width, the region of non-zero secondary emission was located in the 10^1 to 10^2 V range and $\zeta < 3$, consistent with the traveling wave results.

Another related source of deviation from the predicted behavior could be the magnetic field itself. To test this, the same calculations as before were made without the magnetic field, and the results are shown in Fig 3.15. This shows that the deviations observed in Fig 3.14 are eliminated by disregarding the magnetic field, but the magnetic field becomes very small at the electric field maximum as the reflection coefficient increases, so the direct effect of the magnetic field is unlikely to be the cause of the aberrations seen in Fig 3.14. Additionally, the changes to the upper voltage regions of the MMP were more pronounced when the magnetic field was removed, meaning that they also cannot be accounted for directly by the magnetic field. Instead, neglecting the magnetic field likely allowed the electrons to migrate from the magnetic field maximum, altering results. The voltage changes less with axial location near the electric field maxima and more near the magnetic field maxima, so electrons that stray a small distance from the initial axial locations at the field maxima will affect EMP only slightly and MMP more significantly as observed. This means that the deviations in the EMP secondary emission yields with the magnetic field are likely due to the electrons being accelerated away from the electric field maximum. This was further confirmed by initializing multiple trajectories spread between the electric and magnetic field maxima, with the resulting secondary yields resembling those in Fig 3.14 for EMP.

Overall, the simulations were consistent with the underlying theory and previous work on MP in coaxial lines. The theory behind MP has been shown to be vastly more complex than what is often

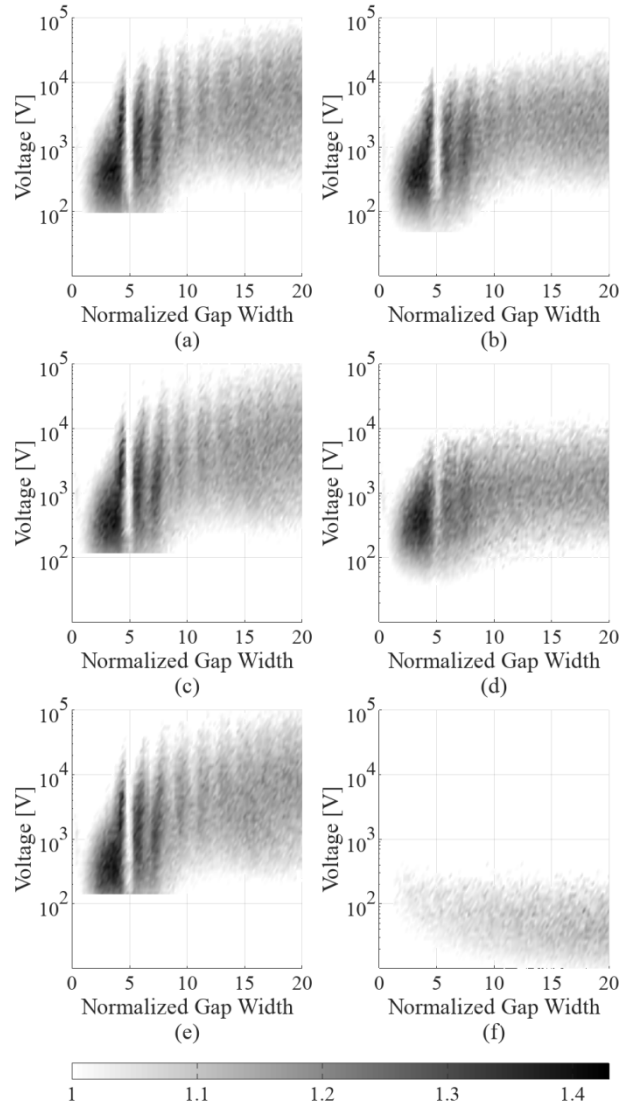


Figure 3.15: Secondary emission yields in the absence of magnetic fields for emission points at the electric maximum (parts a, c, and e) and at the magnetic maximum (parts b, d, and f). Reflection magnitudes used are 0.33 (parts a and b), 0.66 (parts c and d), and 0.99 (parts e and f).

approximated using only a parallel plate model, so a need for numerical approximations to the phenomenon exists. This requires knowledge of the phenomenon and either artifice in determining the occurrence of MP from electron trajectories or the ability to store large numbers of electron trajectories in the working memory of the computer. The former was applied, and what artifice was introduced through both trajectory approximations and calculation of MP metrics was shown to be consistent with

expectations. This was true for traveling and standing waves, both of which are relevant to the analysis of the RF window in the DTL coupler, although there are some simplifications that were made that will be addressed further in the next chapter.

This chapter, together with chapter 4, is in part a reprint of material as it appears in T.W. Hall, P.R. Bandaru, D.E. Rees, IEEE Transactions on Plasma Science **47**, 1526-1533 (2019). The dissertation author was the primary investigator and author of the paper.

Chapter 4

Multipactor near the RF window

4.1: Outline of RF window multipactor analysis

The presence of the RF window in the vicinity of possible MP activity presents a number of novel considerations that must be addressed to avoid this phenomenon and its subsequent damage to the window. The analysis of MP in a coaxial line away from an RF window already showed significant axial drift that could potentially lead to electron collisions with the window solely as a result of a partial reflection of the input signal, so this is an important aspect of MP to investigate. Once the response of MP to the RF window has been established, this then needs to be applied to the RF signals that are present during the operation of the DTL. Finally, other factors that had been neglected in the simulation outlined by the previous chapter, such as higher order modes or the effect of window charges, will be discussed.

The initial analysis of MP near the RF window will be two-dimensional simulations over a range of power levels and normalized gap widths. This will serve as an introduction to the effect of RF windows on MP, and more specifically how MP might affect window performance in the DTL. The window location in relation to the electric and magnetic field maxima resulting from standing waves will be discussed, and a further benchmark of the specialized code will be made against the commercially available CST software. This will allow all the metrics of MP in the system to be analyzed, and the effect of the window will be shown to be significant for certain conditions.

Once the general effects of the RF window on MP are established, the specific case of the DTL at LANSCE can be investigated. To ensure the accuracy of these results, three dimensions will be used as per the previous chapter, and only the frequency of the DTL (201.25 MHz) will be considered. This will greatly reduce the number of extraneous factors as well as increase the resolution of the various power level and reflection effects studied. The MP metrics will again be investigated, and their

relevance to the DTL can be more fully relayed. Additionally, the case of backward propagating signal without a forward reflection will also be studied as this can also happen when the accelerating cavity has large fields but no driving signal. Other information can also be discussed, such as the effect of RF harmonics and HOMs and window charging.

4.2: Generic RF windows

The two-dimensional analysis will first be used to more generally understand MP behavior in coaxial lines near RF windows. Initially, a large number of power levels and normalized gap widths will be investigated, and so the reduced dimensionality of ζ is used for this analysis to speed up the calculations. The previous chapter showed that there might be some inaccuracies with using only two dimensions in this analysis in regards to the percentage of collisions by component, but it will suffice for this initial study. Additionally, the percentage of collisions occurring on the RF window for a smaller sample set can be analyzed against the more computationally rigorous CST PIC software as an additional benchmark to demonstrate what level of reliability the two-dimensional simulation will give in this regard. From there, the relationship between the window placement in relation to the standing wave can be discussed, and the most relevant positions are further investigated. All of the metrics of MP can then be analyzed both in terms of the input parameters and also their relationship to each other.

The effect of the magnetic field on electron migrations is carried over from the previous chapter into the discussion on MP near the window. Since electrons experiencing stochastic emissions will migrate toward the magnetic maximum, the placement of the RF window to be in front of this location (i.e. the window is between the magnetic field maximum and the cavity) will likely lead to increased electron collisions with the window itself. The degree to which this is true, then, is of high importance, as previously developed MP models near a dielectric assume the need of a DC field emanating from charges on the dielectric surface, but this case could itself initiate those window collisions, and thus window charges.

4.2.1: Window collisions as compared against CST

The results of the simulation will first be compared to those of CST Particle Studio. The deficiency of using CST to examine MP is that it can be difficult to avoid rampant electron population growth, and so examining a range of input parameters is difficult to perform without either knowing something of the MP processes beforehand or consuming the available RAM for the simulation. The DTL power coupler dimensions were utilized for this benchmark, and a range of both the reflection magnitude and phase were also studied, with the magnitude ranging from $\chi_b = 0$ (the traveling wave) to $\chi_b = 1$ (full reflection) and the phase spanning $-\pi \leq \nu_b < \pi$. This range of reflection phases will place the magnetic maximum at the full range of distances from a quarter wavelength behind the RF window to a quarter wavelength in front of it, allowing for any potential window collisions when the magnetic maximum is behind the window, and conversely the lack of window collisions when it is in front, to be observed. The power was set to a range of $100 \text{ kW} \leq P_0 \leq 5 \text{ MW}$ for the custom MP calculations, but only one power level of $P_0 = 1 \text{ MW}$ was used in CST Particle Studio for the reasons discussed. A high number of goal collisions should be set to ensure that the results are indicative of the behavior of electrons and not the initializations or a few stochastic emissions that direct electrons to the window, so this was set to 100 collisions. The comparison of the results from CST and the custom code is shown in Fig 4.1, with the results averaged over all power levels.

The general behavior of both simulations is as expected. There are substantial percentages of collisions that occur on the window when the magnetic maximum is located behind the window, indicating that the interactions with the RF window do not substantially alter the effects of the magnetic field from what was already discussed. There is a general trend for the window collisions to increase with the reflection magnitude and the proximity of the magnetic field to the window location. The increase in window collisions as the magnetic field maximum is moved closer to the RF window is only true up to a point however, as the highest percentage of window collisions is for magnetic maximum locations some distance away from the window for most reflection magnitudes. This is a

reasonable expectation, as electrons at the magnetic maximum would not be subject to a net axial force like electrons that are offset from it are. This does change for sufficiently high reflection magnitudes, i.e. $\chi_b > 0.95$, where the window collisions are highest when the magnetic maximum is located at the window. This spike is due to the low electric field being insufficient to generate many collisions at all, and as such most to all collisions simply occur on the window.

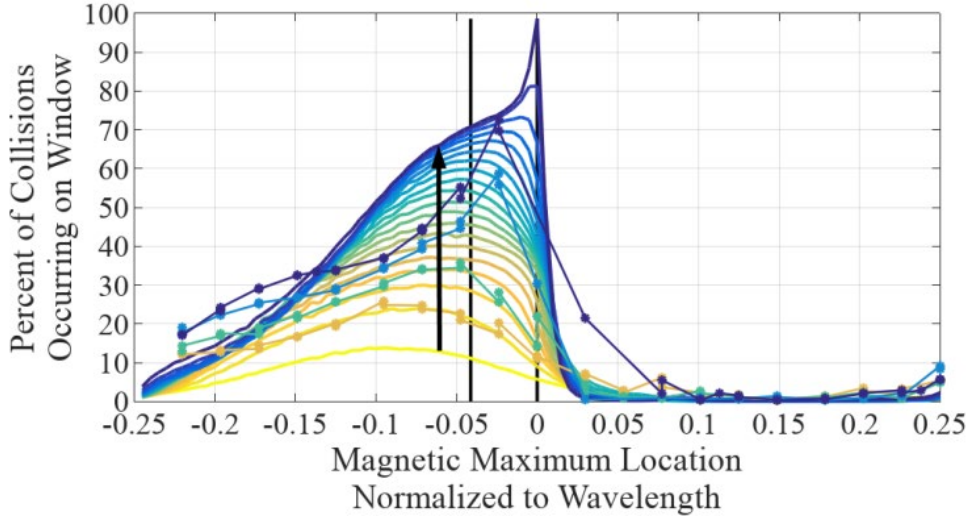


Figure 4.1: The magnetic maxima are normalized to the wavelength so they range between -0.25 and 0.25 , and the RF window is located at zero with negative values indicating that the magnetic maximum is behind the window. Each bold line is the average value of window collisions over all power levels at a particular reflection magnitude. The reflection magnitude between consecutive lines is 0.05 . The results from CST Particle Studio are represented by the lines with markers. The vertical lines correspond to the reflection phases used later in the dissertation (Fig 4.2 and Fig 4.3) © 2019 IEEE.

The window collisions are not only confined to the cases where the magnetic maximum is behind the window, however. Small percentages of window collisions were also recorded for magnetic maxima located $< 0.05\lambda$ in front of the window. The axial motion of electrons should oscillate about the magnetic maximum, since forces accelerating the electrons back to the maximum will only be sufficient to do so after the electron has moved some distance away from the maximum location. This led to the general decrease in window collisions when the magnetic maximum was located directly on the window surface, and it also leads to window collisions for these magnetic maxima a small distance

in front of the window. Additionally, stochastic emissions will exacerbate this effect as electrons can be directly emitted toward the window or emitted away from the window, allowing velocity to accumulate as it is directed back toward the magnetic maximum. A similar effect is also observed as the magnetic maximum is also moved closer to $\lambda/4$, but this is less relevant to the DTL case.

These same patterns were also observed in the CST calculations. Like the custom simulation, CST also showed increased percentages of window collisions for higher reflection magnitudes, and magnetic maximum locations behind the window experienced large window collision percentages with some window collisions even for maximum locations in front of the window. A significant deviation from the CST results, however, was in the actual values of the window collision percentages, with CST generally showing lower percentages of collisions occurring on the window than was calculated with the custom simulations. The largest difference between the two sets of results is about 15% for the values of $\chi_b = 0.6$ and $\chi_b = 0.8$ with the magnetic maximum located in the vicinity of $\lambda/10$ to $\lambda/20$ behind the window. This is likely the result of electron initializations and the dimensionality of the simulations. The electrons were emitted only from the radial position of the geometric mean of the inner and outer conductor radii with only three initial emission phases to reduce the number of simulations that had to be run in CST, as opposed to the 5 radial location and 12 initial phases used in the custom simulations. The results can be affected by the reduction of these parameters, and when those initializations were applied to the custom code, the results better matched. The increased number of initial electrons used in CST could also affect results, and this is an advantage of CST as it can better smooth out the effects of the stochastic emissions with larger numbers of emissions. Overall, the results of CST show the window collisions to also be reliably calculated in the simulations. It should also be noted that when the goal number of collisions was decreased from 100 to 30, the results were similar, indicating that these shorter simulation times are sufficient for analysis.

A significant concern that is raised by these results is the placement of the RF window relative to the field maxima. As discussed in chapter two, the window must be placed near the electric field

minimum to reduce issues like tracking that result directly from high fields, but the location of the electric field minimum is the same as the maximum magnetic field location, meaning that this position could lead to increased MP activity on the window. Even placing the window near but behind the magnetic maximum can produce a small percentage of window collisions, and these can charge the window and possibly lead to MP that is similar to conventional dielectric MP. This can be further complicated by the changing reflections over the course of the transient signal so that the window placement changes. All of these factors must be considered in the placement of the window, hence the necessity of analyzing MP over a wide range of operation parameters.

4.2.2: Calculated metrics

The initial two-dimensional analysis will consist of a wide range of power levels and normalized gap width but only a few reflection parameters. The range of power levels used is directly related to the DTL coupler as the power can be varied. The normalized gap width can be varied in the DTL somewhat if the radii were to be changed, but this would have to be shown to be of significant advantage to offset the cost of replacing the current geometry. Yet the normalized gap width is also important to vary in the initial analysis as it allows the general response of MP to the presence of the window to be recorded, and this in turn is applicable to other systems. Since only certain conditions were shown to lead to window collisions, however, these will be limited to four reflection magnitudes at intervals of 0.245 (again the full reflection is avoided due to the issues observed in MMP) and two reflection phases of $\nu_b = -\pi$ and $\nu_b = -0.835\pi$. The former phase corresponds to the magnetic maximum located at the window, and the latter has the window placed at 0.04125λ behind the window. These phases are represented by the solid black lines in Fig 4.1, and so they should result in a large percentage of window collisions as indicated in that figure.

So far, the discussion of RF window-electron interactions has been limited to the percentage of collisions that occur on the window, but these collisions will also lead to novel forms of MP. Two potential effects of the window on the MP mechanisms can be identified: Either the window is simply

acting as a barrier to restrict the electron motions, or the mechanism is significantly affected resulting in novel forms MP previously unconsidered. Should the former be the case, the position of the window can be used to find χ_{eff} and subsequently the normalized gap width, resulting in somewhat predictable MP as was observed with MMP. If this is not the case, however, then it is indicative of novel forms of MP that result from the window-electron interactions.

The generic predictions of the window collision percentages can be made to inform the veracity of the results. The more time that an electron has between collisions the longer it has to migrate toward the window, and so more window collisions should be observed for these case. The normalized gap width is directly related to the average flight time in the absence of the window, so window collisions should increase for higher normalized gap widths. The emission of electrons from the window surface will result in higher fields required to overcome the initial momentum and carry the electron back to the window, so there should also be increased window activity for higher power levels.

The window collisions for the prescribed operation parameters are illustrated in Fig 4.2, and in general they are in accord with the heuristic predictions. The percentage of window collisions increases with the power, normalized gap width, and reflection magnitude for both reflection phases, just as predicted. The dependence on the reflection magnitude is easy to recognize from the figures, with the maximum percentage of window collisions increasing with its value as predicted by Fig 4.1. The dependence on the normalized gap width, however, is simply a threshold below which there are essentially no window collisions. This threshold is approximately $\zeta = 5$ for all power levels and reflection magnitudes and phases. The values of the normalized gap width below this threshold have too short of flight times for the magnetic field to accelerate them back toward the window, and hence the low number of window collisions. Additionally, these normalized gap widths are the region of two-surface MP in the absence of the RF window, indicating that there might also be a dependence on the mechanism of MP on window collisions. Above this threshold, there is not much variation in the percentage of window collisions. Additionally, there is a strong dependence on the power level for

values of ζ above the threshold, with the percentage of window collisions increasing directly with the power level. These facts make the power level the biggest factor in determining the window-MP relationship, and avoidance of window collisions can be engineered via the power levels to the degree that the power can be modified in the accelerator operation. This dependence on power is fairly consistent across reflection magnitudes as well. It should be noted that the number of window collisions was non zero for every set of operation parameters, indicating that some background window activity will occur.

The effect of the RF window on the secondary electron emission yield is also important as this is the measure of the degree to which MP can occur, and these values are displayed in Fig 4.3. There are changes to the secondary emission yield from the traveling wave case for all the reflection parameters, and some of these changes are outside of what was observed in the EMP and MMP analyses, indicating the presence of novel MP mechanisms. For window collisions below $\approx 25\%$, the secondary emission yield changes with χ_{eff} in the same way as MMP did, meaning that for power levels below around 100 kW (corresponding to window collision percentages $< 25\%$) the secondary emission yield can be predicted to be the same as the coaxial line without the window. These operation parameters result in the window acting as a barrier that only confines the axial motion of the electron, and so the window collisions are not otherwise significant to MP here.

As the percentage of window collisions increases past $\approx 25\%$, the secondary emission yield does begin to change from the pattern of MMP. These are the beginning of novel modes that the three surfaces of the inner conductor, outer conductor, and RF window create. For the lower reflection magnitudes ($\chi_b < 0.49$), the secondary emission yield stays high for $P_0 > 100 \text{ kW}$, but the exact value does undulate over normalized gap width intervals of about 15, as opposed to intervals of up to about 3 for the traveling wave case. This could be novel interactions or simply a change to the mean axial location and thus χ_{eff} , but either way these undulations are only of minor importance. The significant change is to the parameters where window collisions are above 50%. These result in high $\bar{\delta}$ values for

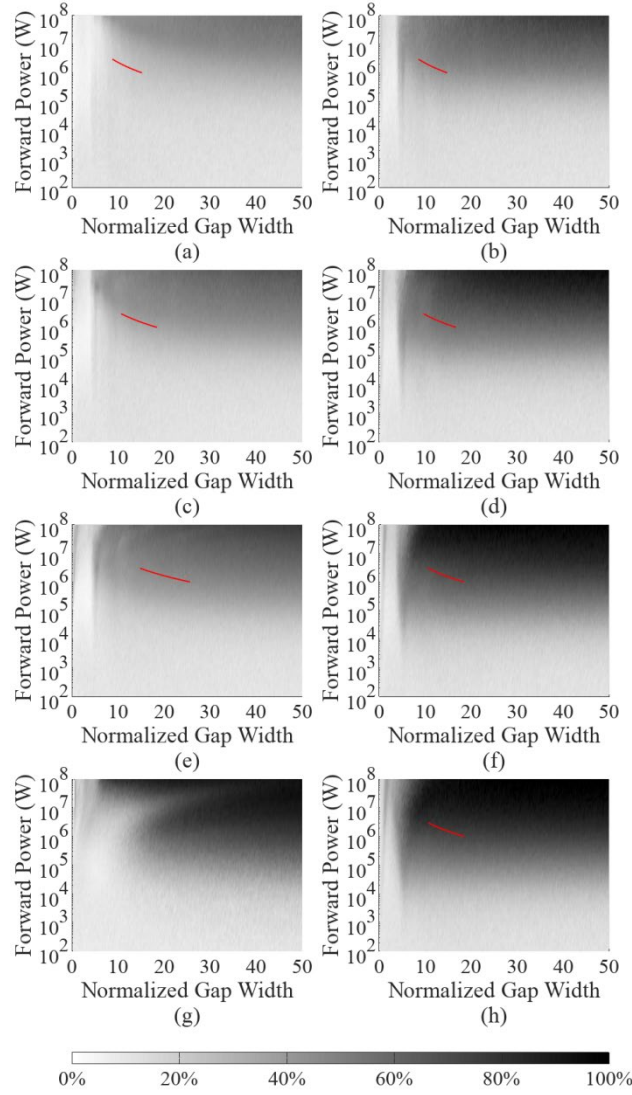


Figure 4.2: Percent of collisions occurring on the window for the reflection phase of $\nu_b = -\pi$ (parts a, c, e and g) and $\nu_b = -0.835\pi$ (parts b, d, f and g). The reflection magnitudes are 0.245 (parts a and b), 0.49 (parts c and d), 0.735 (parts e and f), and 0.98 (parts g and h). The number of window collisions is generally higher for the phase of $\nu_b = -0.835\pi$ and increases with the reflection magnitude. The range of normalized gap widths for the example coaxial line is illustrated by the red curve © 2019 IEEE.

the $\nu_b = -0.835\pi$ phase, but for the phase of $\nu_b = -\pi$ the regions where window collisions are this frequent are either for unrealistically high powers or nearly full reflections where the electric field is negligible and thus no MP occurs. The high secondary emission yields created by the magnetic maximum being located just behind the RF window are due to the novel MP modes, and these can

present a serious impediment to prevention of MP in the line.

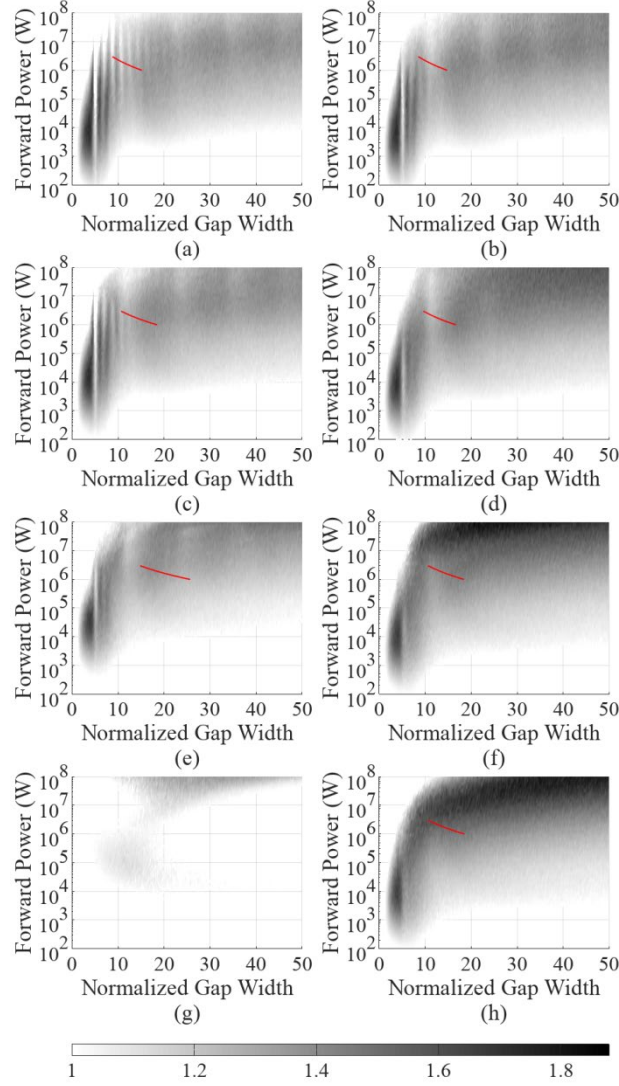


Figure 4.3: Secondary emission yield for the reflection phase of $\nu_b = -\pi$ (parts a, c, e and g) and $\nu_b = -0.835\pi$ (parts b, d, f and g). The reflection magnitudes are 0.245 (parts a and b), 0.49 (parts c and d), 0.735 (parts e and f), and 0.98 (parts g and h). The secondary emission yield maintains similar values for most power levels, normalized gap widths, and reflection magnitudes. A region of high secondary emission yield values is introduced in part (d) and becomes dominant in by part (h). Part (g) has vastly different values resulting from the nearly complete lack of the electric field. The range of normalized gap widths for the example coaxial line is illustrated by the red curve © 2019 IEEE.

It is important to consider how the DTL window is affected by these parameters, but the use of the normalized gap width somewhat obfuscates the results in terms of the fixed frequency. While this

will be analyzed in more detail shortly, a range of power and normalized gap widths for the fixed frequency of 201.25 MHz is illustrated by a line in Fig 4.2 and Fig 4.3. This curve has a power ranging from 1MW to 3 MW, and the resulting normalized frequency changes with χ_{eff} as calculated at the RF window. Some of the issues that have been discussed do fall in the range of the DTL power and normalized gap width, so the detailed analysis of these parameters is necessary.

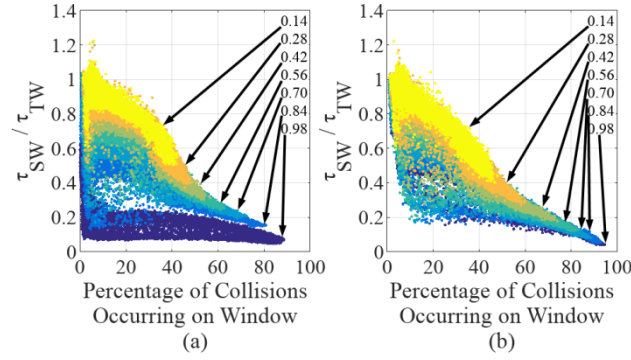


Figure 4.4: Ratio of the time between collisions (standing wave to traveling wave) for (a) magnetic maximum at the window location and (b) the magnetic maximum is behind the window. Many τ_{SW} values are reduced from τ_{TW} for $\chi_b = 0.98$ and $\nu_b = -0.835\pi$ as a result of very weak electric fields that allow electrons to traverse nearly straight paths © 2019 IEEE.

The last MP metric to be discussed is the time between collisions. While the number of window collisions was heuristically explained in terms of the time between collisions, nothing has been said of the actual change to flight time for the observed novel MP modes. The collision of electrons with the window are interruptions to the expected trajectory, and thus the time between collisions can be expected to decrease with increasing window collisions, and this is observed in Fig 4.4. This figure shows the ratio of the time between collision for the above standing wave simulations and the traveling wave simulations of the same power and normalized gap width. The strong negative correlation between the time between collisions and the percentage of window collisions exacerbates the increase in the secondary emission yield observed in these novel MP modes because the decrease in the time

between collisions will increase the number of impacts in a given time period, and thus more electrons are generated.

4.3: DTL RF windows

Next, the behavior of MP under the conditions of the DTL operation can be assessed. Since the frequency is fixed, MP will be analyzed at 201.25 MHz and using a range of power levels up to 5 MW. These calculations will use three dimensions to account for some of the previously discussed shortcomings of 2D simulations. First, the traveling wave cases will be discussed, both as a baseline when discussing the standing wave results and as important considerations in their own rights. Then the standing wave cases are analyzed, with the same emphases placed as the previous general results. Finally, additional considerations will be made to account for potential deficiencies in the simulation up to that point, such as material properties and deviations from actual fields will be discussed throughout.

4.3.1: Traveling waves

The traveling wave cases form the basis for the in depth analysis of MP in the DTL coaxial coupling line. A forward traveling signal in a coaxial line has been shown by previous work to be comparatively straightforward, and the addition of the window should not significantly alter that previous work as the forward power will carry electrons from the window surface. However, the simulation of MP for this case is important as it will show both the expected secondary emission yield and the percentage of collisions occurring on the window. In addition to the forward traveling wave, the backward traveling wave must also be considered. This case can occur in the DTL when the input signal has been shut off as the energy in the cavity begins to be emitted into the coupler, and unlike the forward traveling wave, electrons are expected to migrate toward the window. The necessity of investigating this case should be apparent, as the increased interaction of electrons with the RF window will change the secondary yield.

The results of these traveling wave cases are shown in Fig 4.5. The traveling wave case exhibits behavior that is expected due to both known MP in coaxial lines (e.g. as in Fig 3.8) and what was observed along the line indicating the DTL line in Fig 4.5. The forward traveling wave is going to experience some level of MP for nearly all power levels, with only those near zero and the upper 3 MW range having secondary emission yield less than unity. This means that MP should be an issue in a coaxial line such as this, and it might not be possible to eliminate MP but rather minimize and manage it. Practically, the traveling wave case is only of concern during the steady state of the fill transient when the particle beam being accelerated is on, as discussed in chapter 2. While MP in this system is never desirable, this time during the DTL operation is particularly bad as it directly interrupts the delivery of power to the cavity, and could ultimately alter the delivery of the beam to its targets. Since nearly all power levels experience MP though, the phenomenon cannot be fully mitigated by changing the operation power, although it can be managed.

The backward propagating wave has similar results to the forward propagating wave. The backward propagating wave again produces very few power levels where the secondary emission yield acts to reduce the electron population, so again little can be done in regards to the power level to mitigate MP. In this case, the situation is actually even worse as the occurrence of the backward propagating signal is determined by the fields present in the cavity when the input pulse stops, and those fields must be at a certain level in order to provide the proper acceleration to the beam, thus giving less control over the backward propagating signal. The management of MP due to traveling waves will be detailed further down.

The backward propagating wave does experience the increase in window collisions as expected. There was a small baseline of electron-window activity for the forward propagating signal due to the small number of collisions (i.e. 30) that were simulated, with somewhere around 5% of all collisions occurring on the window. The backward propagating wave had about 5% of collisions occurring on the window at the lowest power levels and increased nearly linearly to about 30% at 5

MW. These collisions came at the cost of the outer conductor collisions as seen in Fig 4.5. The inner conductor collisions were nearly the same for both cases, so the presence of the window again appears to interrupt the migration of electrons to the outer conductor, leading to the increased window activity. These window collisions might also account for the slight increase to the secondary emission yield from the forward propagating case, and the emission of secondary electrons from the window surface can lead to a positive charge on the surface that will act to further attract electrons. This illustrates further the difficulty in avoiding MP in the line, as the backward signal is unavoidable in the pulsed operation of the DTL, since those cases examined thus far only have unfavorable conditions that exacerbate the problems of MP.

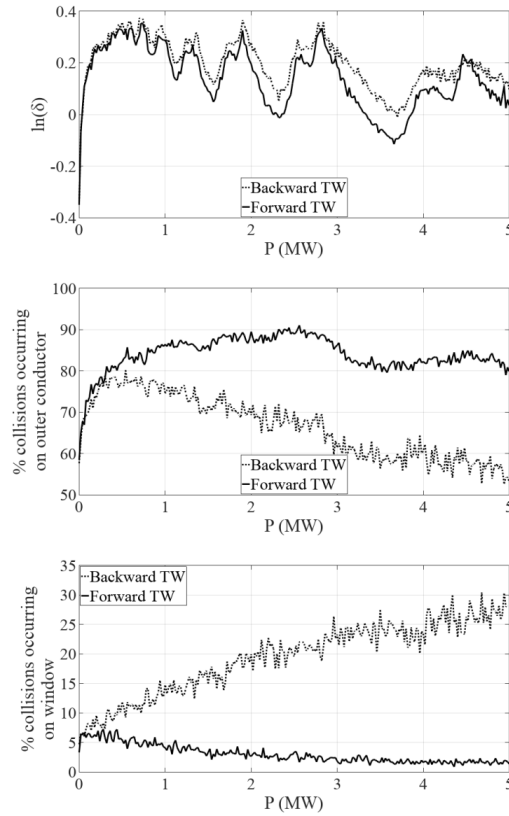


Figure 4.5: MP metrics for forward and backward propagating traveling waves. The metrics considered are the secondary emission yield (top) and the percentage of collisions occurring on the outer conductor (middle) and RF window (bottom).

4.3.2: Standing waves

The standing wave condition is considered next in order to account for potential MP during other times of the fill transient. The reflection magnitude χ_b is set to a range of values from zero to one, and the secondary emission yield is plotted versus χ_b (y-axis) and the power (x-axis) in Fig 4.6. Since a range of reflection phases may apply to the DTL operations, 20 sample phases were used in the range of $[-\pi, \pi)$, where the exclusive upper range was set due to the redundancy of $\nu_b = \pi$ with $\nu_b = -\pi$. The reflection phase in Fig 4.6 is translated to the location of the magnetic field maximum relative to the RF window surface. The behavior of the P - χ_b - $\bar{\delta}$ plots as the magnetic maximum location is changed typically reflects the EMP and/or MMP types of MP discussed in the previous chapter and observed in Fig 3.12. When the magnetic field maximum is far behind the window (i.e. $< -0.125\lambda$), the EMP type dominates due to the electrons being emitted by the window surface toward the electric field maximum. The secondary emission yield when the magnetic maximum is located a small distance behind the window more closely resembles MMP because these cases were those earlier observed to have a high number of window collisions. Their initial emissions are far enough from the electric field maximum that a similarity to MMP, along with the window collisions, is to be expected. The shift in secondary emission yield values from the EMP to MMP patterns is then maintained for positive values of the magnetic maximum location.

The percentage of collisions occurring on the window under standing wave conditions provides the baseline understanding of how MP affects the window. While a large electron population might accumulate, this will be of little interest to the window operation if there is not some appreciable interaction of the electrons with the window (though still very important to DTL operation as a whole). The percentage of collisions that occur on the window is a good indication of those electron window interactions, although there are some shortcomings of using this. For example the electron population could be confined to an axial location a small distance from the RF window, leading to few collisions being recorded at the window. This case could then result in added EM stress on the window when the

electron population is sufficiently high, or a change in standing wave conditions could subsequently move the population toward the window. Neither of these detrimental effects would themselves be recorded by window collisions alone, but both could be accounted for by other means, as will be discussed later. Furthermore, a general relationship of axial electron confinement to field maxima has already been established, so the relationship of this to window collisions must be examined.

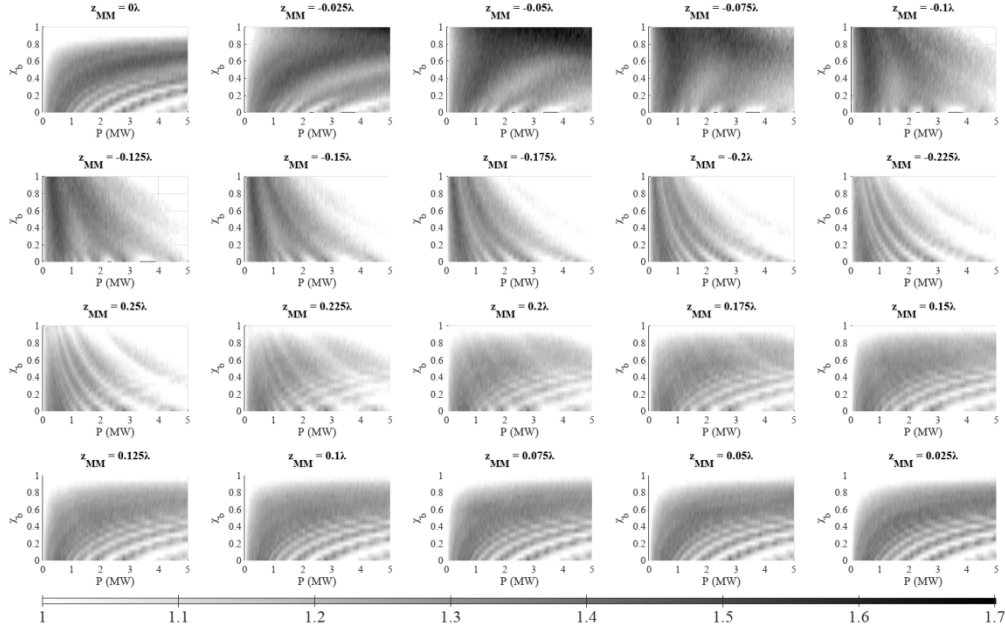


Figure 4.6: Secondary electron emission yield over varying power (P) in the abscissa and reflection magnitudes (χ_b) in the ordinate for the DTL geometry at 201.25 MHz. The various parts of the figure correspond to different reflection phases that place the magnetic maximum location (z_{MM}) at various locations relative to the window as labeled in fractions of the wavelength λ , with negative values being located away from the cavity.

Overall, the percentage of collisions occurring on the RF window is the same as what was observed for the two-dimensional analysis. The window percentages were higher the closer the magnetic maximum was to the window (while still being behind it), and the values also increased with the reflection coefficient χ_b , as shown in Fig 4.7. Despite the change in dimensionality, the reflection phase with the magnetic maximum located at the window surface ($z_{MM} = 0\lambda$ in the figure) still has the same peculiarities, namely the spike in window collisions for $\chi_b > 0.95$ with otherwise lower window

collision percentages than the next phase (i.e. such that $\chi_b = -0.025\lambda$) for other values of the reflection magnitude. The spike in window collisions for this phase places nearly all collisions occurring on the window, but those operation parameters that produce 100% window collision also have low secondary emission yields, meaning that those conditions might be more desirable. By placing the window at this point, it might actually be possible to also reduce the charges that accumulate on the window then, and the specifics of this will be discussed later in the chapter. The other phases also show much of the same behavior as the two-dimensional model did, with the only quantifiable change being that the three-dimensional results had slightly more window collisions.

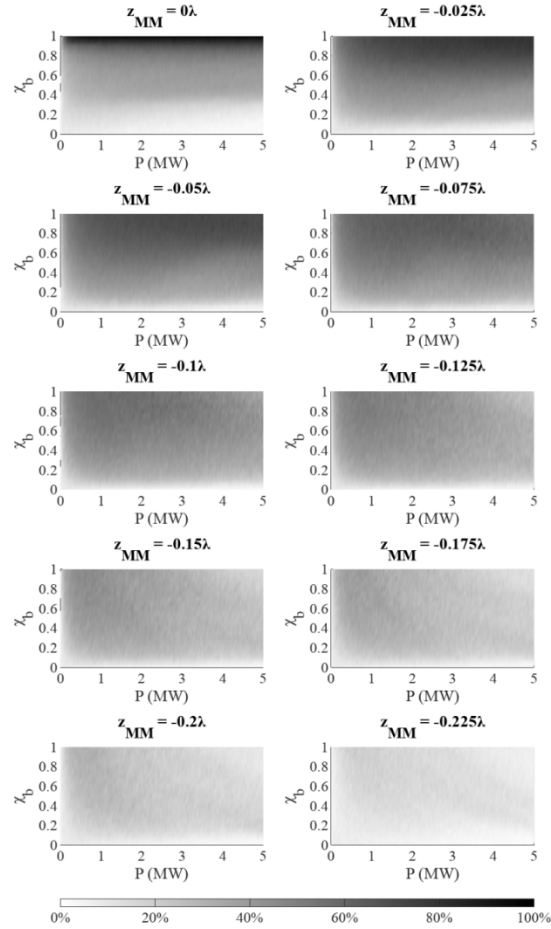


Figure 4.7: Percentage of collisions occurring on the RF window for $z_{MM} \leq 0$ for the DTL at a frequency of 201.25 MHz and a range of power levels (P) and reflection magnitudes (χ_b). Magnetic maxima are labeled as a fraction of the wavelength in the figure.

Those reflection phases where the magnetic maximum is a small distance in front of the window (between the window and accelerating cavity) are also shown in greater detail in Fig 4.8. These all typically have low percentages of electron collisions with the window, with only the phase placing the magnetic maximum at 0.025λ providing noticeably non-zero values for every $P\text{-}\chi_b$ combination. The lower power levels provide some readily observable incidents of electron-window collisions, but the unexpected result is a consistent high window collision percentage observed at a particular reflection magnitude over all power levels. The reflection magnitude at which there is an increase in window collisions does appear to shift slightly to higher values with changing magnetic maximum locations. These particular results were investigated further by changing various parameters such as dimensionality, time step, number of collisions, consideration of relativity, and initializations to ensure this was not a calculation error, but all of those changes maintained the same result. Further investigation was made by examining electron trajectories, including velocities and force exerted on the electron, but there were no outliers observed.

Since the clean, unexpected result appears to be reliable, a justification of this result is proposed. For those reflection phases that place the magnetic maximum behind the window, it has been shown that the window collisions increase with increasing reflection magnitudes due to the increase in the magnetic fields that act to accelerate the electrons in the axial direction. When the magnetic maximum is in front of the window, however, electrons are not in general being accelerated toward the window, but instead toward the magnetic maximum. As previously postulated, the electrons will oscillate about the magnetic maximum location due to the interplay between the net force toward that location and the momentum of the electron as it passes through that point, and this was confirmed in examining trajectories. As the reflection magnitude increases, the distance of this oscillation will decrease due to the increase in the magnetic fields that limit the distance the electron's momentum can carry it. This effectively makes electrons less prone to window collisions with higher reflection magnitudes, and so the window will experience less stress from MP when the reflection is high, such

as at the beginning of the RF pulse. However, until the reflection magnitude reaches some value, the magnetic field might also not be sufficient to allow electrons to oscillate about the magnetic maximum to generate window collisions by this means. Furthermore, electrons that do collide with the window are emitted with a higher distribution normal to the window surface in the axial direction, thereby requiring higher forces to be accelerated back to the window for repeat collisions.

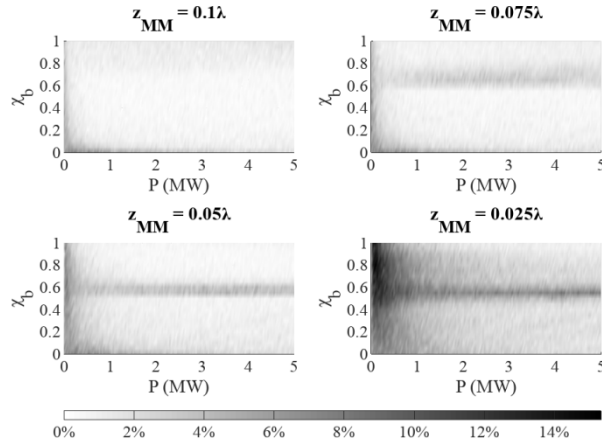


Figure 4.8: Percentage of collisions occurring on the RF window for select $z_{MM} > 0$ for the DTL at a frequency of 201.25 MHz and a range of power levels (P) and reflection magnitudes (χ_b). Magnetic maxima are labeled as a fraction of the wavelength in the figure. Other values of $z_{MM} > 0$ are not considered as they have negligible window collisions.

This heuristic explanation was then further examined using a fixed power level to compare the reflection magnitude where the window collision percentage spikes, if at all, over varying reflection phases. The power was fixed at 3 MW, and the reflection phases ranged from $\frac{\pi}{2} \leq \nu_b < \pi$ so that the magnetic maximum is less than 7.5 inches in front of the window. The percentage of collisions occurring on the window across the reflection magnitudes and phases are shown in Fig 4.9 as a fraction of the maximum percentage of window collisions for a given phase/magnetic maximum location. This normalization allows the reflection magnitude at which the window collisions peak to be more readily observed, and the maximum window collisions are also shown in the figure so it is obvious that those phases that place the magnetic maximum farther from the window do still have lower percentages of

window collisions. The peak in window collisions does occur at increasingly higher values of the reflection magnitude as the magnetic maximum shifts away from the window as predicted, with the exception of those magnetic maxima nearest the window, which behave like the phases with the magnetic maximum located behind the window. Overall, these results validate the heuristic explanation of the high dependence of the window collisions on the reflection magnitude.

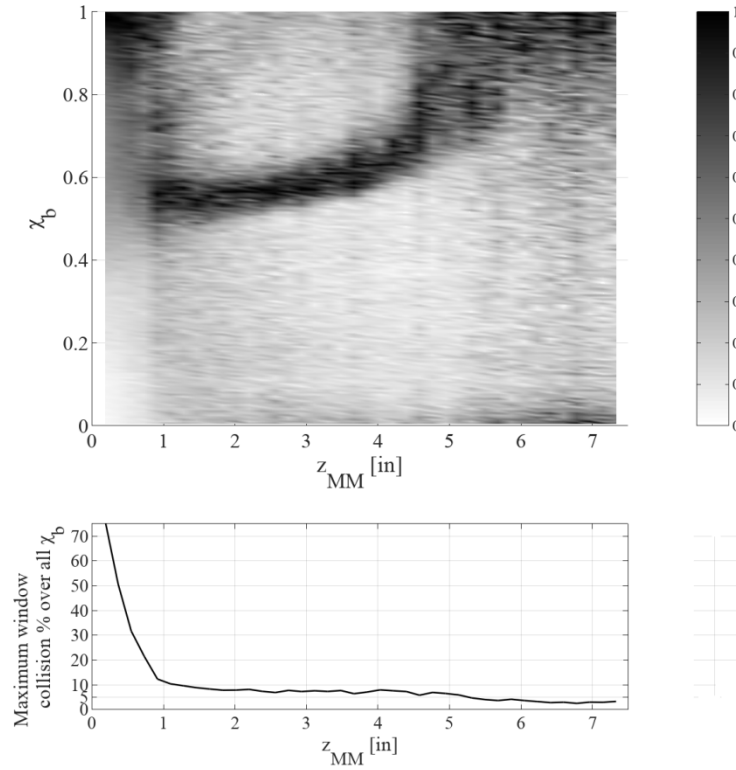


Figure 4.9: Window collisions for a magnetic maximum located less than $0.125\lambda = 7.33$ in in front of the window for a variety of reflection magnitudes. The window collisions are expressed as a fraction of the maximum percentage of collisions occurring on the RF window over all reflection magnitudes for each z_{MM} in the top part of the figure, and the bottom part of the figure shows that maximum percentage of collisions occurring on the window at each magnetic maximum location.

The mitigation and management of MP to protect the window now requires the above analyses to be aggregated for the transient properties of the DTL operation. The parameters of the forward and backward propagating signals were discussed in chapter two, and recalling that discussion it is clear

that a single result from the previous window MP analysis is sufficient in describing MP during the operation of the DTL. As the fields in the accelerator cavity are established, the backward propagating signal, and thus the standing wave conditions, changes. This means that in order to avoid MP, it must be ensured that MP and electron collisions are minimized across the RF pulse, so a means of optimizing the MP conditions must be developed. To start, the population can be expressed in terms of the secondary electron emission yield after each collision:

$$p = p_0 \prod_{n_c}^{N_c(t)} \delta_{n_c} \quad (4.1)$$

where n_c is the index of each collision of the theoretical macroparticle used in the simulations, and $N_c(t)$ is the total number of collisions experienced at time t . This is the fundamental aspect of how the electron population develops mathematically, whereby the initial population p_0 is multiplied by the secondary emission yield δ_{n_c} upon each collision. It should be noted that Eq 4.1 is a statistical representation of the real world development of electron populations since electrons can collide with surfaces at varying times and produce varying numbers of electrons. This was simplified in the simulations by the use of the macroparticle, which also allows for the simplification of the population estimations.

The parameters that were recorded in the during the simulations of MP in the DTL coupler can then be used in conjunction with Eq 4.1 to get estimations of the change in electron populations over the RF pulse. To do this, it is first recognized that the value of the secondary emission yield that was recorded from the simulations was the geometric mean of individual emission yields recorded upon each macroparticle collision. This allows the product in Eq 4.1 to be replaced by the recorded value of the secondary emission yield ($\bar{\delta}^{N_{sim}} = \prod_{n_c}^{N_{sim}} \delta_{n_c}$, where N_{sim} is the total number of collisions in the simulation) over so that

$$p = p_0 \bar{\delta}^{N_{sim}} \quad (4.2)$$

Next, the time between collisions (τ) can be used to evaluate $N_c(t)$ in Eq 4.2. The value of τ recorded

in the simulations has units of cycles per collision, so that the estimated number of collisions at any time is simply the time in RF cycles divided by τ . This can then be applied to Eq 4.2, and its logarithm taken so that

$$\ln(p) = \ln(p_0) + gt, g = \frac{\ln \bar{\delta} \omega}{2\pi\tau} \quad (4.3)$$

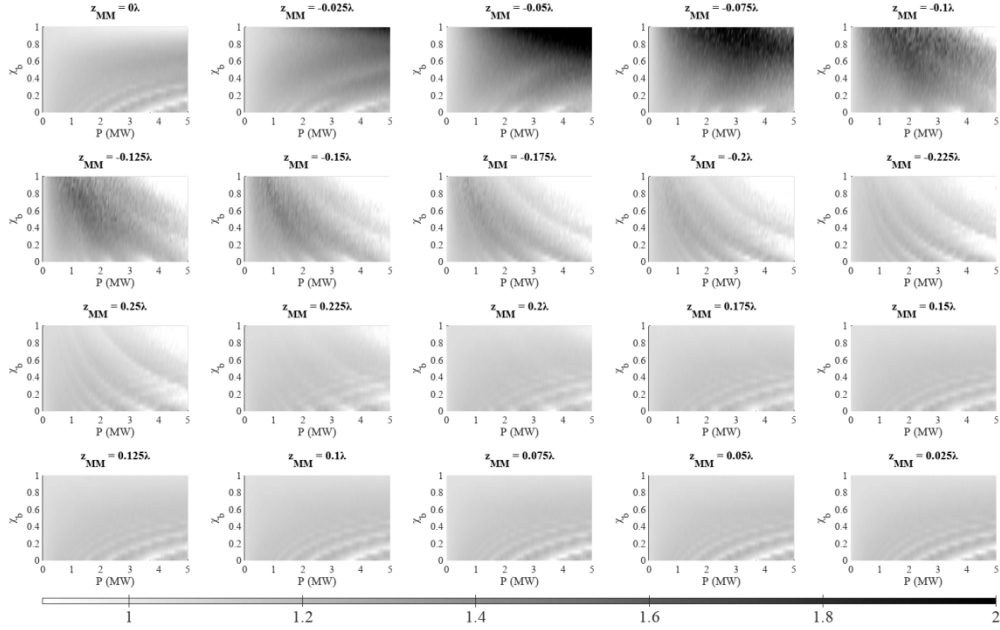


Figure 4.10: Growth parameter over varying power (P) in the abscissa and reflection magnitudes (χ_b) in the ordinate for the DTL geometry at 201.25 MHz. The various parts of the figure correspond to different reflection phases that place the magnetic maximum location (z_{MM}) at various locations relative to the window as labeled in fractions of the wavelength λ , with negative values being located away from the cavity.

This equation shows the useful parameter g that can better describe how MP can build in a system than considering the secondary emission yield alone. While the secondary emission yield was used for previous analysis, this growth parameter g will allow the aggregate MP response of the coupler over the RF pulse to be considered. The difference between using the secondary emission yield and the growth parameter is highlighted by contrasting the respective results in Fig 4.6 and Fig 4.10. The two have mostly similar results, but the time between collisions for $z_{MM} = -0.05\lambda$ and $z_{mm} = -0.075\lambda$

have values of g that are much higher than other phases whereas the secondary emission yield has a similar range across all phases. This shows how the time between collisions can significantly alter the expected accumulation of MP in a system, but it should also be noted that the patterns observed in each phase are comparable between the secondary emission yield and the growth parameter, so the previous uses of the secondary emission yield are still valid.

4.3.3: Effect of emission properties

The analysis of MP near the window has thus far been limited in its accuracy by the knowledge of the emission properties of the RF window material. While the Furman model proves useful in its ability to capture the many facets of secondary emission, the availability to apply this model is limited by the number of parameters it uses to describe emission and the difficulty in fitting those parameters to data. There are numerous articles that have analyzed the emission properties of various materials and for various conditions [40] [41] [42] [43] [71] [72] [73] [74] [75] [76], including polymers similar to the material Rexolite® that is currently employed at LANSCE. These materials typically have secondary electron emission values that range from being comparable to stainless steel or copper—the two materials with published parameters by Furman et al.—to values two or three times that high. Because Rexolite® is a cross-linked polystyrene, published values for polystyrene were investigated, but the range in secondary emission properties for the family of polystyrene materials is as large as that of polymers as a whole.

In order to have a basis for the above analysis, the emission properties of copper were applied to the RF window. The limitations of this approach are obvious, but there are also good reasons for it. First, one source found a maximum secondary emission yield of 2.07 at 200 eV for polystyrene [40] whereas copper has a peak of 2.1 at 271 eV, meaning that the differences in the secondary emission are reasonably small. Another peak value of polystyrene was found to be 3.0 at 250 eV [40], indicating that the use of copper emission properties might result in low secondary emission values for the operation parameters considered. However, even moderate numbers of window collisions were observed to

appreciably increase the emission yield, so the use of a potentially lower emission yield curve than might be expected for the window material does not appear to miss any regions of window MP that might be observed with higher secondary emission values. Because of these uncertainties in the material properties, the use of copper emission properties provides as good results as could be reasonably attained with the given information.

One additional aspect of the window material that will be considered is that of potential coating materials. Window coating treatments are applied in an attempt to mitigate MP by reducing the secondary emissions of the window, as well as preventing charge accumulation on the surface. Charge accumulation is attenuated by using a material with a non-negligible conductivity that allows any charges that created by secondary electrons leaving “holes” to be filled as currents move through the coating. This necessitates that the coating thickness be carefully selected as too thin a coating could potentially allow electrons to pass through it to the window, resulting in high secondary emission yields persisting, and too thick a coating will interfere with the transfer of the RF signal down the line.

One coating material that has been previously shown to reduce MP is titanium nitride (TiN) [52]. Secondary emission yield properties are limited for this material, so the Furman model parameters were loosely fitted to match the emission data available. The match between the available data [77] and the fitted Furman model curve is shown in Fig 4.11. The maximum emission yield of TiN is lower than that of copper, but whereas copper has values of $\delta > 1$ for a range of 34.5 eV to 2413.8 eV, this fit has a range from 109.7 eV to 3651.2 eV. Additionally, there is no information on the emission velocities of the emitted electrons, so the Furman parameters of both copper and stainless steel will be used to show how significant the effect of using those specific emission properties. The emission energies using those two sets of parameters is also shown in Fig 4.11.

The first comparison that is made using TiN as the material is for the backward propagating signal. This signal was shown to have only moderate numbers of window collisions (Fig 4.5), and so it will show how this coating can affect MP when the percentage of collisions is below about 25%. The

reduction in the growth parameter is about as expected, with values decreasing for higher window collision percentages. Interestingly though, this was not the case with the secondary emission yield itself as the changes to its value with material properties were moderate and did not appear to change with power, and thus window collisions. This indicates that the behavior of the trajectories is sufficiently modified so that the time between collisions is increased for the TiN material. This is also supported by the slight decrease in the window collisions observed for the TiN properties.

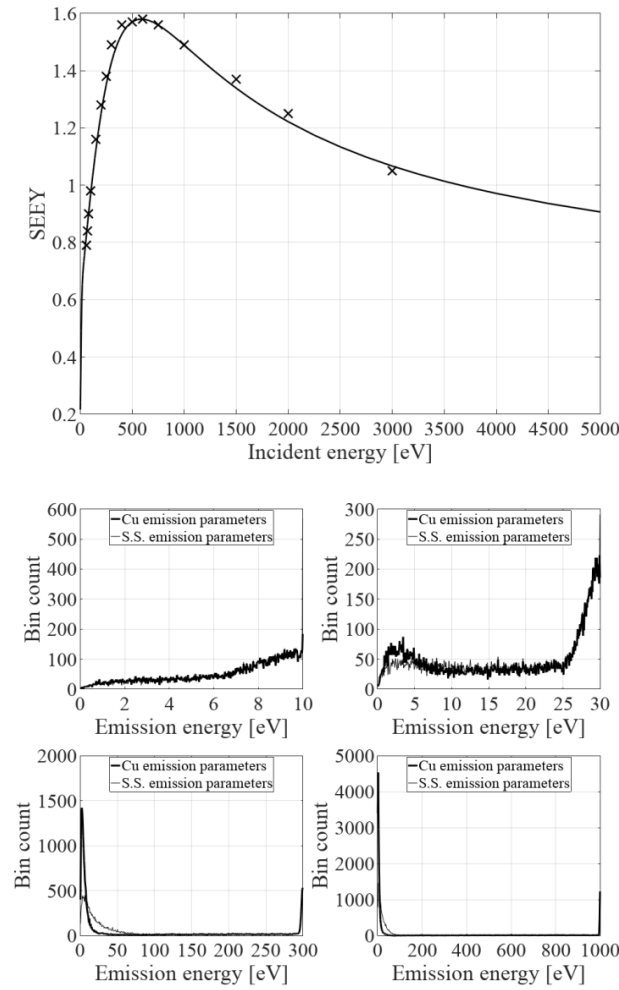


Figure 4.11: Secondary emission properties used for TiN. The secondary electron emission yield as measured by [77] is compared against the values from the Furman model using fitted parameters (top). Emission energy distributions for collision energies of 10 eV, 30 eV, 300 eV, and 1000 eV are shown in the bottom portion of the figure with the maximum emission energy corresponding to the collision energy.

The effect of the unknown emission properties does not appear to have a significant effect. The results using copper and stainless steel emission parameters did not differ from each other by a significant amount as all three results shown in Fig 4.12 are within the range of noise that is present. It is important to note however that the emission yield does affect the emission properties themselves, and this explains why there is a minor difference in the percentage of collisions occurring on the window and the time between collisions. Overall, the lack of information on the emission properties of a material similar to Rexolite® does not appear to be a detriment to evaluating MP near the RF window.

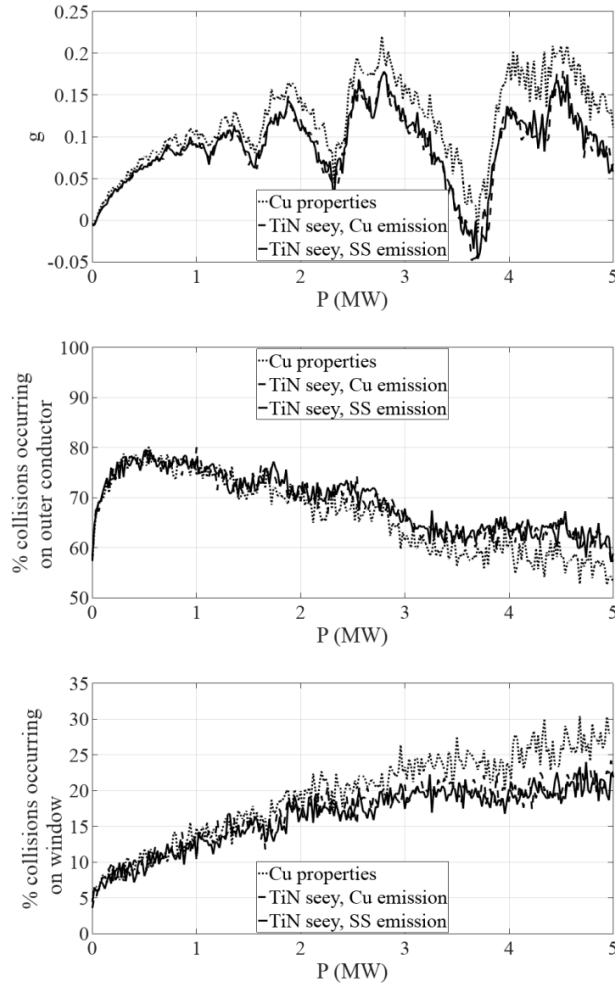


Figure 4.12: Comparison of the MP metrics for a backward propagating wave over various window

materials. The metrics considered are the secondary emission yield (top) and the percentage of collisions occurring on the outer conductor (middle) and RF window (bottom).

However, the backward propagating wave is only a specific case, and so a standing wave case with a high number of window collisions was also examined. The reflection parameters were set to $\chi_b = 0.95$ and $\nu_b = -0.8\pi$, as this showed a high number of window collisions in the earlier calculations and subsequently a secondary emission yield of $\delta > 1$ for most power levels. The growth parameter as calculated using the different emission properties as the RF window material is shown in Fig 4.13. Like the traveling wave case, the growth parameter is reduced for this standing wave condition, but the degree to which it is reduced in this case is much greater. The application of the TiN coating does not eliminate MP for the traveling wave case above, but it does for the standing wave case as all the values for the growth parameter are less than zero. Whereas the collisions with the window generally resulted in increased secondary emission yields without the coating, the properties of the TiN emission led to secondary yields decreasing with increasing numbers of window collisions. Unlike the backward propagating wave, the changes to the growth parameter considering TiN are due to the secondary emission as changes to the flight time can alter the magnitude of the growth parameter, but negative values can only be due to the secondary emission yield.

Overall, the TiN emission properties show that its use as a coating is beneficial. The growth parameter became negative for all power levels of the considered standing wave condition, and for the backward propagating traveling wave, the growth parameter became negative for more power levels. The negative growth parameter values mean that MP cannot occur as any collisions will reduce the electron population, and any events that would otherwise initiate MP will not. This means that the coating has the potential to completely eliminate MP for many standing wave conditions, whereas other conditions will have more power levels that do not lead to MP. Even for those power levels where the growth parameter was still positive with the coating, its value was reduced. Some of the conditions will be unavoidable as the accelerator cavity must be allowed to fill as discussed in chapter 2, so the reduction of the growth parameter is essential in reducing MP throughout the transient pulse. So by

simply adding a TiN coating, the generation of RF signals that minimize the potential of the coupler to experience MP is more readily possible.

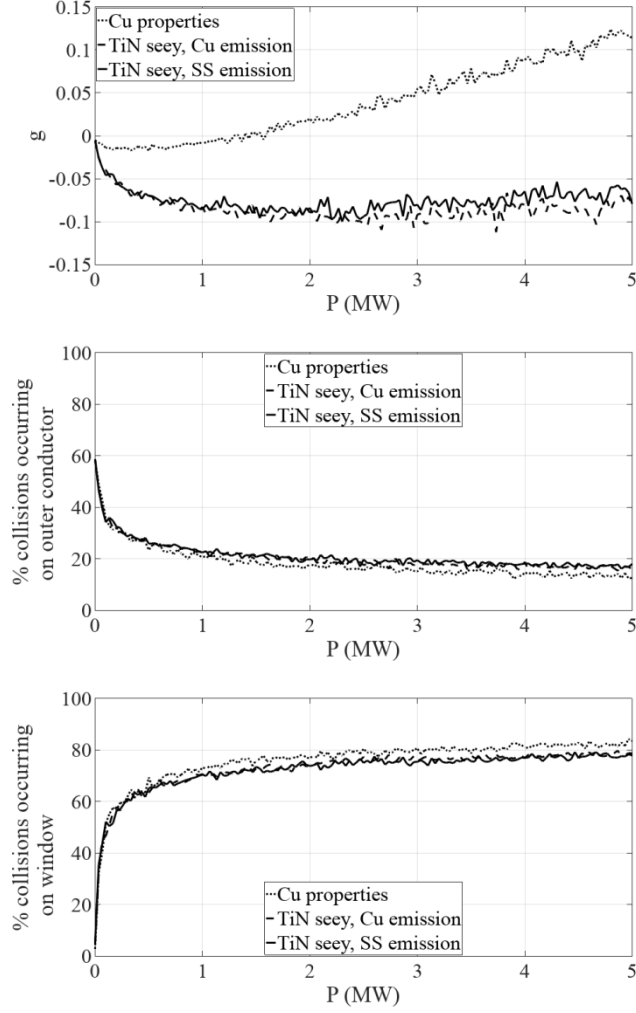


Figure 4.13: Comparison of the MP metrics for a standing wave of $\chi_b = 0.95$ and $\nu_b = -0.8\pi$ over various window materials. The metrics considered are the secondary emission yield (top) and the percentage of collisions occurring on the outer conductor (middle) and RF window (bottom).

4.3.4: Higher order modes and harmonics

There are other important factors that have been thus far assumed negligible that could affect the results. Firstly, the effects of the window geometry on the EM fields have been neglected, but as shown in chapter two there are some variations to the EM fields that are considerable near the RF

window. These can be accounted for as higher order modes (HOMs) as this magnitudes and phases of those modes were discussed in detail for the DTL coupler geometry in chapter two. Another issue is that of the harmonics discussed in chapter two. While any harmonics present will be small, their effect must still be investigated as it has the potential to alter the resonance property of the MP phenomenon.

The impact of HOMs and harmonics on the EM fields near the RF window has already been discussed, and since these have some impact on the fields it can be expected that there is potential for them to also impact MP. As discussed in chapter two, HOMs are scattered from the window geometry as the conductor surfaces change. Fortunately, few HOMs were found to have any significance, and the only modes of any appreciable magnitude were the TM_{0n} modes, with $n \leq 2$ being sufficient to provide a conservative estimate of the coupler fields. This is important as the calculation of the Bessel functions is computationally expensive, and so reducing the number of modes to be calculated is desirable. The magnitudes and phases of the HOMs are given in Table 2.1, and those values were used to simulate the HOMs in the MP calculations.

The harmonics also affected the EM fields in a few significant ways. The most substantial way in which the harmonics affected the fields was to allow some HOMs that were scattered by the line terminus to propagate back to the RF window, as shown by the magnitudes of the HOM signals in Fig 2.21. The TE_{11} modes scattered from the line terminus were still of a smaller magnitude than those scattered by the window, so the TE_{11} modes will be neglected for the time being. The TE_{11} modes excited by the harmonics could have a potentially interesting effect on where window collisions occur since these modes have an azimuthal component that could drive them to specific azimuthal locations.

The results of applying both harmonics and the HOMs to the EM fields are shown in Fig 4.14. Somewhat surprisingly, neither consideration has an appreciable effect on the results. The growth parameter only varies within the range of noise present, with a few exceptions where the presence of the harmonics does seem to alter the results slightly. This occurs near the power levels where the value of the growth parameter dips close to 1.5 MW, 2.25 MW, and 3.75 MW, and the harmonics increase

the growth parameter slightly. This contributes to the need to eliminate the harmonics but is not highly significant. The HOMs had no observable effect on the growth parameter at all because of their low amplitude relative to the TEM mode, and this is a good indication that the previous work on MP can be assumed to be valid. It should be noted that the fields found in Fig 2.5 using only the two TM_{0n} modes used in these MP calculations were larger than those recorded in CST, and so the negligible effects of the fields used in the MP simulation indicate the use of more accurate fields are unlikely to have any effect on MP as well.

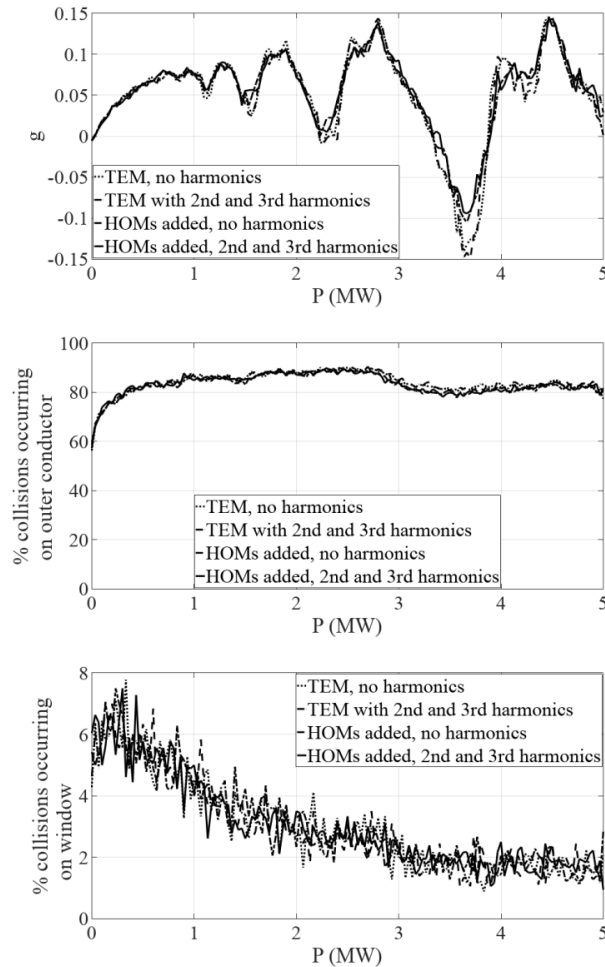


Figure 4.14: Comparison of the MP metrics for a forward propagating wave considering the inclusion of harmonics and window scattered HOMs. The metrics considered are the secondary emission yield (top) and the percentage of collisions occurring on the outer conductor (middle) and RF window (bottom).

4.3.5: Charge accumulation on window

The accumulation of window charges will occur for MP with window activity and can significantly alter the fields and thus MP in the coupler. Charge accumulation is driven by the window collisions that result in true secondary electrons being emitted from the window and leaving behind a net positive charge near the emission point [74] [78] [79]. This positive charge will then act to further accelerate the electrons back to the window surface, thus leading to higher charges on the window and exacerbating the problem. These changes to the fields have the potential to completely alter how multipactor progresses and must be considered in conjunction with previously discussed results.

In order to examine how accumulated window charges might affect MP, the accumulation of charges must first be considered. The SW example used for the materials, HOM, and harmonics analyses ($\chi_b = 0.95$, $\nu_b = -0.95\pi$) has the right conditions for charge accumulation to occur (i.e. high secondary emission yield and high numbers of window collisions), so that case will be used here to record window collisions. Only the radial and azimuthal positions and electron population of the window collisions are needed for this purpose, and the parameter set is also counted and recorded so the collisions can be sorted by power level. With this information recorded, bins can be defined over small ranges of the angles and radii to determine how many collisions occurred within a small region of the window, thus creating a two-dimensional histogram as seen in Fig 4.15. This histogram shows most collisions occurring at the initial angle of emission and dropping off away from that value, and the radial distribution is similar over all angles with more collisions occurring towards the middle radial positions. These trends are somewhat predictable as there is no acceleration in the azimuthal direction, and thus all variations are due to stochastic emissions.

In addition to the distribution of window collisions, the electron population can also be utilized to generate the charge distribution in the window. The charge distribution ρ is important as it is used in Poisson's equation to find the voltage so that

$$\nabla^2 V = -\frac{\rho}{\epsilon_0} \quad (4.4)$$

Since the charge accumulation is due to secondary emissions leaving positive charges in the window, the charge generated upon any particular collision is going to be related to the population and secondary emission yield upon that collision. The most accurate way to record the charge distribution would then be to calculate the true secondary emission yield and multiply this by the electron population before the collision to get the number of electrons emitted, and thus charges generated, by that collision. The use of the separate types of emission yields (i.e. elastic backscattering, rediffused, and true secondary) was not originally implemented, however, and due to the limitations of utilizing these charge distributions to calculate fields as discussed later, it was not deemed worth altering the existing code to do this. Instead, the charge generated is assumed to be that of the population itself, and this method will lead to larger DC fields, and thus more conservative estimates.

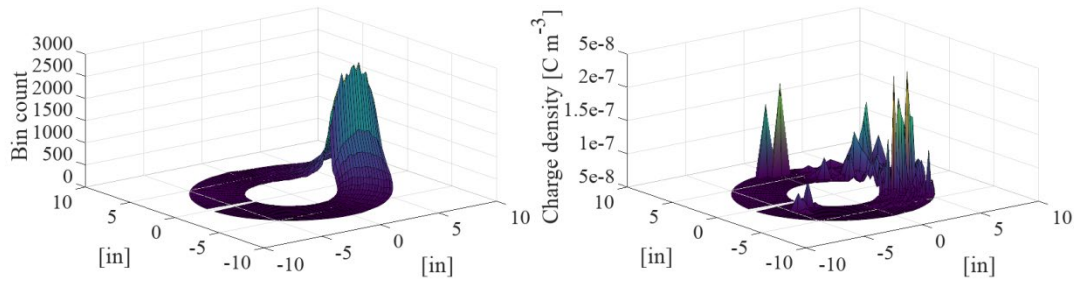


Figure 4.15: Spatial distribution of electron collisions with the RF window (left) and the corresponding charge density of those collisions (right) for all collisions under the standing wave conditions $\chi_b = 0.95$ and $\nu_b = -0.95\pi$.

To that end, the same bin definitions that were used to create the 2D histogram in Fig 4.15 were used to find the summation of all recorded charges in particular regions of the window. The charge distribution can then be calculated by dividing this summation by the area of the window region ($((\phi_{i+1} - \phi_i)(r_{i+1}^2 - r_i^2))/2$, where i is a subscript allotted to the region under consideration) and by the thickness of the charge distribution. This thickness is somewhat arbitrary as the electron trajectories only account for a two dimensional window, so the baseline thickness of the DTL RF window without any notches (0.885 in.) was used as a conservative estimate. The results are also shown in Fig 4.16, and

it is clear that these results are more erratic than the bin counts of collisions only due to some collisions occurring when the population is quite high. This is another demonstration of the difficulty of accurately calculating the charge distribution and thus fields generated by electron collisions on the window. To have both smoother charge distributions, the bin counts of either collisions or the charge distribution shown in Fig 4.16 could be used to calculate the dc fields in the simulation of MP.

It is apparent from this discussion of charge accumulation that there are limitations to its calculation. The generation of charges and the penetration depths have already been discussed, and it is apparent that an exact dynamic accounting of these factors within the simulation would require a significant overhaul to the current simulation process. In addition to these, the macroparticle approach means that the actual distribution of charges will be lost as the macroparticle represents a population of electrons that would be spread over space, and so by its nature these simulations cannot perfectly predict charge accumulation. The use of any recorded charge distribution must also account for the conditions for which they were calculated. The values shown in Fig 4.15 were aggregated for all power levels with $\chi_b = 0.95$ and $\nu_b = -0.95\pi$, so individual power levels might have different distributions. These individual power levels were individually examined, and there was not any discernable pattern in the collision or charge distributions, so the use of those found in Fig 4.15 should still be sufficient. Of course, it is also possible for charges to accumulate due to other standing wave conditions, and this might further affect the distribution. An alternative to calculating the charge distribution is to also use the point charges themselves, however the method used to calculate the fields from the charges is more sensitive to point charges, and so having a distribution is better to apply to it.

With the charge distribution established, the dc fields can then be calculated and applied to the MP simulations. There are two ways that this can be accomplished: analytically or computationally. The analytic approach has the benefit that it allows different charge distributions to be transformed into the electric field by a few simple calculations, whereas the computational approach will require a complete re-calculation including all its complexity for each charge distribution that might be

considered. The analytic approach can be readily integrated into the existing code, although the computational expense of finding the requisite Bessel functions will limit its speed. On the other hand, the computational approach would require either significant additions to the code, which would lend itself to a new host of potential problems and inaccuracies, or import of results from a program such as CST. Either one of these options would necessitate calculation of the electric field at finite points within the coupler that would then need to be interpolated to the macroparticle position, and this would increase the memory required of the program. Overall, these two options are similar in the increased requirements on the simulation and accuracy, so the analytic approach is selected for its adaptability, which could be useful for should the charge distribution become more accurate in the future.

The analytic solution to Poisson's equation in the coaxial line geometry is best accomplished using Green's function in series form. The electric fields must be normal to the conductor surfaces, and as a result the stationary charges that accumulate on the window generate complicated fields. The boundary condition whereby fields are normal to the conductor surfaces can be conceptualized as resulting from mirror charges on the other side of the conductor, and to some degree this is the physical phenomenon that occurs as any tangential components to the electric field are cancelled by their displacement of electrons within the conductor. However, since there are two conductors, this mirroring of charges in one conductor must then itself be mirrored in the other conductor, thereby setting up an infinite series that is further complicated by the cylindrical geometry. A mathematically equivalent expression of this is to use Green's functions to change the inhomogeneous Poisson's equation into the quasi-homogeneous equation [59]

$$\nabla^2 G(\mathbf{r}, \mathbf{r}_0) = \delta(\mathbf{r} - \mathbf{r}_0) \quad (4.5)$$

The Green's functions are then defined as the solution to Poisson's equation when $\rho = 0$ with a few modifications to ensure the properties of Green's functions are maintained. First, the voltage itself will be zero on the conductor surface, and as such the boundary condition of the Green's function is that it is zero at the conductor surfaces and at an infinite distance away. Secondly, the function G will consist

of multiple modes due to the solution of the Laplacian operation on it, so that $G = \sum G_n$. Finally, the Green's function must satisfy the condition of $G(\mathbf{r}, \mathbf{r}_0) = G^*(\mathbf{r}_0, \mathbf{r})$. Considering all these requirements, it can be shown that the Green's function that satisfies them is

$$G(\mathbf{r}, \mathbf{r}_0) = \sum_{n=1}^{\infty} \left(a_n J_{m(n)}(k_n r) + b_n Y_{m(n)}(k_n r) \right) \left(a_n J_{m(n)}(k_n r_0) + b_n Y_{m(n)}(k_n r_0) \right) \cos(m(n)(\phi - \phi_0)) \exp(-k_n |z - z_0|) \quad (4.6)$$

This definition is not complete however as it must be assured to satisfy Eq 4.5. Firstly, it should be noted that the left hand side of Eq 4.5 is

$$\nabla^2 G(\mathbf{r}, \mathbf{r}_0) = \sum_{n=1}^{\infty} -2k_n \delta(z - z_0) G_n \quad (4.7)$$

The summation of constituent functions G_n does approach the behavior of $\delta(r - r_0)\delta(\phi - \phi_0)$ as $n \rightarrow \infty$, so the behavior of the Green's functions as defined in Eq 4.6 is confirmed to meet the requirements. However, it should be noted that the coefficients a_n and b_n are not themselves defined solely by the boundary conditions offered, so the actual values of the Green's functions are thus far arbitrary. However, by recognizing that the integral over volume of the right hand side of Eq 4.5 is by definition equal to one, the values of the coefficients can be found by setting them to $a_n = A_n \tilde{a}_n$ and $b_n = A_n \tilde{b}_n$ and solving

$$\sum_{\substack{n=1 \\ m(n)=0}}^{\infty} 2\pi A_n^2 \left(\tilde{a}_n J_{m(n)}(k_n r) + \tilde{b}_n Y_{m(n)}(k_n r) \right) \int_{r_i}^{r_o} r_0 \left(\tilde{a}_n J_{m(n)}(k_n r_0) + \tilde{b}_n Y_{m(n)}(k_n r_0) \right) dr_0 = 1 \quad (4.8)$$

for each value of r between r_i and r_o . It should be noted that this only offers solutions to the modes with $m(n) = 0$, but the other modes can be readily found by recognizing that the behavior of $\lim_{n \rightarrow \infty} G = \delta(r - r_0)\delta(\phi - \phi_0)$ is true only when the portion $\cos(m(n)(\phi - \phi_0))$ is multiplied by the same value for every value of m . This means that the condition $m(n) = 0$ in Eq 4.8 can be generalized to $m(n) = \text{constant}$.

With the Green's functions defined, there is little more to do to apply them to the simulation of MP. First, the voltage can be found from the established charge density by:

$$V = \int_{r_i}^{r_o} \int_0^{2\pi} \int_{-\infty}^{\infty} G(\mathbf{r}, \mathbf{r}_0) \left(-\frac{\rho(r_0)}{\epsilon_0} \right) r_0 dz_0 d\phi_0 dr_0 \quad (4.9)$$

With the voltage established, the fields are then defined by the relationship $E = -\nabla V$. It is apparent that the number of modes of the Green's function must be limited, but there should be sufficient modes to approximate the fields to avoid overly burdening the simulation with their calculation. The number of modes to use was difficult to judge using point sources as they did not have voltages that converged even for very many (>84000) modes at the point source location. Considering the established charge densities however, they did converge for all locations with only 60 modes needed to sufficiently approximate those voltages found with 84000 modes for individual point sources. Those 60 modes consisted of $0 \leq m \leq 4$, with each value of m having the 12 modes with the lowest value of k_n .

These values for the dc electric field generated by the RF window were again applied to the forward traveling wave and the standing wave used for the other extra considerations. First, the collision distribution found in Fig 4.15a was applied to Eq 4.9 with varying multiplication factors applied to account for the arbitrary nature of using collision distributions instead of the more physically accurate charge densities shown in part (b) of the figure. Again, this was done because the collision distribution was smoother, so any issues in the field calculations and their subsequent effect on the MP simulations that might arise from the sharp peaks of the charge density could be avoided. Additionally, the charge distributions had peaks at azimuthal locations away from MP initialization, whereas developing MP would generate fields that might prevent these peaks from forming in the first place.

The results of these simulations are shown in Fig 4.16. Obviously, the percentage of collisions occurring on the window should increase as the dc field multiplication factor, and thus the restorative forces to the window, increases. This is what is observed for both the traveling wave and standing waves. Since there is already some acceleration toward the window in the standing wave case, even the weakest fields increase the window collisions to nearly 100%. This can quickly compound the issue

that is of concern with the window charges in that they can direct electron trajectories back toward the window surface and thus create more charges more quickly. The traveling wave case also experiences a rapid increase in window collisions with even weak fields. As can be expected, the percentage of collisions occurring on the window for the traveling wave case does decrease with power as the magnetic field that would carry away electrons becomes stronger and can counter-act the dc fields. The magnetic field is comparatively weak in its ability to accelerate electrons toward the window near the window, but as the electron moves farther from the window they will balance each other out.

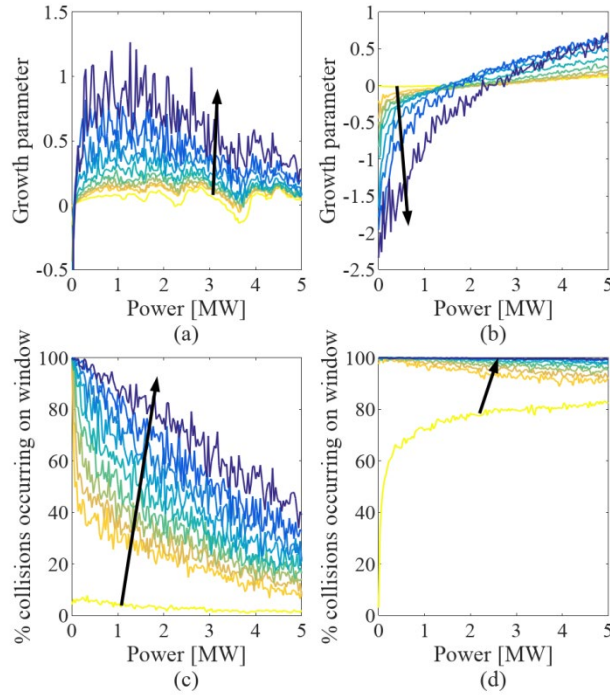


Figure 4.16: Change in growth parameters (top parts) and window collisions (bottom parts) for the backward propagating traveling wave (left parts) and the standing wave conditions of $\chi_b = 0.95$ and $\nu_b = -0.8\pi$ (right parts) for varying strengths of the DC field on the window. The factor by which the DC field varies is zero (no field) or powers of 10 ranging from 2 to 6 by 0.5, and the arrow in each part points from the lowest to highest factor.

The growth parameter is also shown in Fig 4.16. The increase in window collisions and the change in the velocity of those impacts greatly changes how MP can grow in the system for both the

traveling and standing waves. The consideration of the dc field on the traveling wave results in the growth parameter shifting from having some negative values to having all positive values for power levels exceeding those on the order of 10 kW. This is very significant as the growth parameter is an expression of the logarithm of electrons generated per cycle, so that even for very weak charge accumulations the traveling wave generates far more electrons than would be accounted for without consideration of the window or window charges. Even more significantly, the regions where MP is excluded by negative values of the growth parameter quickly diminish and disappear with growing dc fields, so that if a sufficient charge is accumulated on the window, the operation of the system at those power levels to avoid MP would experience unpredicted failures. Furthermore, even for those weak dc fields, the traveling wave is producing more charges on the window as a result of both the window collisions and growth parameter increasing, so that the window charge, and thus window collisions and growth parameter increase. This is the loop that can rapidly result in a parasitic and damaging electron population that has been otherwise unpredicted.

The growth parameter of the standing wave does offer some redeeming qualities however. This case does not experience increasing growth parameter with increasing dc fields, but rather the growth parameter becomes negative for the lowest power levels as the dc field increases. This is related to the traditional dielectric MP where the balance between the dc field normal to the dielectric surface must balance the RF field with an electric field tangential to the dielectric surface so that the restorative force of the dc field allows the RF field enough time to accelerate the electron to an energy capable of generating secondary electrons. As the dc field strength increases, the power level at which the growth parameter becomes positive also increases, and it would be expected that at some dc field strength all the power levels would have negative growth parameters. These negative growth parameters would conceivably lead to the dc field weakening as the charges are cancelled by the absorption of electrons into the material, and so the net result is that the charges on the window eventually balance out and the electron population will remain stable.

For very large dc field strengths, it was observed that electrons could not leave the window surface, which would completely quell any MP from occurring. This does not mean that these conditions are then inert to window performance, but rather that the electron population can only build to a certain point. This limit could still be well beyond what is needed for the window to fail, but the above analysis shows that it is possible for the dc fields to greatly influence MP. This is another argument for the use of the TiN coating, as its conductivity allows the accumulated charges to be dissipated.

This chapter, together with chapter 3, is in part a reprint of material as it appears in T.W. Hall, P.R. Bandaru, D.E. Rees, IEEE Transactions on Plasma Science **47**, 1526-1533 (2019). The dissertation author was the primary investigator and author of the paper.

Chapter 5

Summary and Conclusions

The continuous operation of the drift-tube linear accelerator depends on the ability of the RF window to withstand the many complex and interdependent stresses that are placed on it. These stresses are accounted for to a large degree in the initial design of the coupling system, such as in the placement of the window to minimize the electric field stresses or selection of a durable window material, but an increase in failure frequencies showed that there are some conditions in the DTL at LANSCE that were not accounted for and required remediation. The two most obvious issues that could lead to window failures were breakdown caused by the electromagnetic fields and the multipactor phenomenon that could arise from those fields. The EM conditions under typical accelerator operation were analyzed first, with and without the effect of the accelerator considered, and then those conditions in the accelerator were used to analyze the extent of MP that could occur.

The EM conditions were analyzed by simulating the transient fields that occur in the power coupler to the DTL accelerator. First, the coupler was considered without the accelerating cavity to observe how the EM stresses can be minimized without the complexity added by the cavity. Next, the EM stresses were evaluated when the accelerating cavity was included, which required a method to be developed to analyze this highly resonant structure during the fill transient, and then this method was applied to several conditions that occur in the DTL.

The most fundamental aspect of window stresses considered was that of the EM fields on the window geometry, so this was first analyzed in isolation. The voltage across the window surface was analyzed as the dominant factor in potential window failures due to the complicated physics of interfaces and observed damage on the air side of windows, while other potential issues such as heating were neglected due to lack of evidence in window damage. Small adjustments to the window geometry were made that decreased the surface voltage from the currently employed design in the range of ~10

to $\sim 100 \text{ mV/W}^{-1/2}$, which translated to a few hundred volts in the range of accelerator operations. This still leaves that voltage well under the bulk dielectric strength of Rexolite® and most other potential window materials, but the surface-air interface could still experience intermittent flashovers.

These flashovers do not appear to lead to window failures in and of themselves, but they do affect the conditioning of the window. Because the costs of altering the window geometry in the ways analyzed are negligible, those geometries could be implemented to best identify if the geometry change does have the intended benefits. If the window proves more difficult to condition, or if the observed tracking does not lessen, those geometry changes might not be necessary. However, this has not taken into consideration the effect on multipactor, and the vacuum side geometry changes could potentially either mitigate or exacerbate the current multipactor issues. The effect on window geometry on multipactor will be discussed later with other issues on the topic.

The accelerating cavity can have a significant effect on the overall EM environment, and thus on window performance itself. The high Q-factor of the accelerating cavity results in fill times that are five orders of magnitude greater than the RF period, so significant difficulties arise in the simulation of a filled cavity. This issue was addressed by using a signal with a large initial amplitude that was brought down to the nominal amplitude at steady state. This approach was verified incrementally from analytic means to increasingly more complicated structures and ultimately to comparison with measurements taken from the DTL. This approach allowed the transient response of the accelerating cavity to be simulated in hours as opposed to days or weeks without the risk of accumulating numerical errors leading to either unphysical exponential growth or otherwise grossly inaccurate fields. This approach could be expanded to investigate other items of interest such as cavity arcing and particle simulations and is useful to not only the DTL that was of interest in this dissertation, but can be applied generally any high-Q system when the transient response will affect coupler fields.

There are also downsides to the quick fill approach. The condensed fill time resulted in reflections from the driving signal continuing to be established and subsequently there was significant

noise in the output signal through the coupling line. This noise then affected the calculation of the total reflection magnitude and phases, although these still were shown to provide reasonable approximations to the measured cavity responses taken at LANSCE. This quick fill method can be applied to other systems that have highly resonant structures to better analyze issues that could arise in them as well, and any potential changes to cavity or cavity-coupler aperture geometries could greatly benefit from this approach.

The analysis of the DTL coupler/cavity system was then performed and several key factors in the window performance noted. First, the amplitude and phase of both the reflected signal and the signal emitted from the cavity were found, as these can allow the stress on the window due to its position relative to the established standing wave to be found throughout the fill transient. This compared well to the measured reflection magnitudes measured at LANSCE indicating its usefulness in showing the EM conditions at the window to minimize RF stresses and, later, multipactor. Then the presence of harmonics in the driving signal was considered, and though simulations showed that there was not a strong resonance in the cavity of these signals, their presence was apparent in the reflected signal.

For even weak harmonics of the desired frequency, there were noticeable reflections of higher order modes that added azimuthal variations to the EM fields, and this could be a contributing factor to the window failures, particularly as there is an azimuthal variation on the observed window damage. The geometry of the line could be changed so that the HOMs emitted from the cavity are heavily attenuated, thus reducing any effect they might have.

It should also be noted that all of the EM analysis was performed in the absence of the particle beam in the cavity. The acceleration of the beam requires it to absorb some of the energy from the cavity such that with the beam on the reflected signal and emitted signal will sum to zero. This will not have a significant change to most of the analysis, but can affect the discussion of harmonics as the change to the small emissions of HOMs cannot be determined by the analysis that has been done.

Multipactor was then considered, with a discussion of the phenomenon and its simulation

preceding the analysis of the DTL system. The requirements and constraints of the simulations were discussed, and benchmarks showed the simulations to be consistent with other analytic, numerical, and experimental findings. The presence of standing waves was shown to have a great effect even without the window, as has been observed in previous works, and the presence of standing waves near the RF window can potentially result in many window collisions. While these conditions occurred for standing waves with the magnetic maximum position “behind” the window, i.e. the window is between the magnetic maximum and the accelerating cavity, it was possible for some collisions to occur with the window positioned in the current design location implemented at LANSCE.

The signal emitted from the cavity will have also have an effect on MP that changes throughout the fill transient. The current distance that the window is placed from the cavity is such that the magnetic maximum is located $\sim 0.04\lambda$ in front of the window at the beginning of the input signal, resulting in low numbers of window collisions as can be seen in Fig 4.1. At steady state, the magnetic maximum shifts by $\sim 0.25\lambda$ so that the magnetic maximum nearest the window is at $\sim -0.21\lambda$, which still had a low albeit increased number of electron collisions with the window. This shift is due to the coupler-cavity system being designed to minimize the reflected signal at steady state by having the pure reflection and emission phases shifted by about 180° (i.e. $\nu_e - \nu_r = \pi$), but unless this relationship is exact, there will be a gradual shift in the magnetic maximum that could place the window such that there is a sudden increase in window collisions. The further the reflection and emission phases are from this relationship, the more gradual this shift is, potentially allowing for significant numbers of window collisions as the standing wave changes. The parameters calculated in chapter 2 would not result in the magnetic maximum passing through the window throughout the fill, which is desirable, but the phase of the emitted signal is dependent on cavity fields so that the magnetic maximum might pass through the window for other conditions not simulated (e.g. adding post-couplers to the model or the presence of a particle beam.). This could also explain why there is a difference in window failures between the different tanks at LANSCE.

The observed failures of the RF window can be compared to these observations to conclude how the predicted MP is likely to lead to failures. First, the high incidence of window failures dropped dramatically when the TiN coating was applied. This indicates that the window was actively contributing to the MP process as predicted by simulations since the coating provides both a reduction in secondary emission and a mechanism for charges generated by secondary emissions to be drained to the conductors. Second, the worming has always been observed to occur within 30° of the centerline of the coupling loop. The simulations showed an azimuthal distribution of window collisions near the initial source of electron emissions, and so the azimuthal dependence of window failures is likely an indication of where MP is initialized as opposed to being a result of the MP process itself. Considering the damage to the coupling loop that was observed in concurrence with many of these window failures, this means that the coupling loop is likely to be a cause of the MP and, ultimately, the failures. The mitigation of MP due to the coupling loop initiations could be achieved by bending the coaxial line so that the window is no longer directly exposed to the ionizing radiation that is emitted from the coupling loop and likely causing MP.

Another mitigation technique that does not require any alterations to the current system is to simply engineer the input signal to minimize the secondary emission and window collisions. The secondary emission yield is above one for nearly all times of the RF pulse, making it possible for MP to occur at any point in the signal, and there is some potential indication of MP occurring throughout the signal in the presence of observed window arcing. The input power of the signal can be adjusted to minimize the growth parameter and window collisions for that forward power and the resulting reflected power. The movement of the input power is limited by what is necessary for the accelerator operation, but during the start and shut-off of the signal, the input power can at least reduce the production of electrons due to MP. The manipulation of the RF signal should be applied in consideration of the EM stresses as well, but based upon the observed damage and window failures, these considerations should be secondary to MP.

While the method of simulating MP was useful in determining whether MP could develop over a large number of operation parameters, there were limitations to the type of information it could provide. The calculation of the secondary electron emission yield using the macroparticle approach did provide similar results to the predicted MP by theory, experiment, and other simulation techniques, proving that it was useful in predicting MP, and the other parameters like component collision percentages and times between collisions also provided information that is consistent with what is known about MP. Those metrics of MP were of the greatest interest to the mitigation of the phenomenon in the DTL coupler, but the effect of the electron population on window performance is difficult to find with this method.

The power deposited on the window by the electron collisions would be important to determining if the phenomenon is capable of causing the type of damage that has been observed. And if it is, how could that type of heat damage best be mitigated since some source of impurity can be unintentionally reintroduced that would instigate MP and lead to failures? This is a question that can only partially be answered by considering the metrics that were used to analyze MP, but other factors such as electron population at a given instant, spatial locations of impacting electrons, impact energy, etc. would all contribute to the energy imparted to the window [29] [35] [50]. These factors could better be considered by using a raw electron population to analyze the effect of MP for a very limited number of operation parameters, but if MP is mitigated in general, the heat generated would naturally be of a lesser concern.

Similarly, the electric fields generated by the electron population have not been considered. For significant electron populations, there can be a direct effect of the electric field on the RF window that could lead to breakdown, and the electric field could again be calculated based on the macroparticle that is used in the simulation with limited accuracy. The main limitation on the accuracy would again be the lack of spatial information on how the electron population is distributed, and the change of the electron density with time also adds another complication to simply utilizing a macroparticle in the

field calculations.

Beyond the field effects on the window, the electron field effect also changes the development of MP by altering electron trajectories. This is the saturation effect and is detailed in a number of works [80] [81] [82] [83] [84]. However, this detail is of little importance to considering if MP develops for given operation parameters as there must be a significant electron population developed by MP for this effect to be of significance. An interesting consideration is that one analysis of the saturation effect utilized a simplification of the fields generated by the electron population that would put the zero-field radius at the geometric mean of the inner and outer radii, making this the point about which the electron population might oscillate. This could explain why more points of catastrophic damage were observed near that point than would otherwise be indicated by the distribution of window collisions shown in Fig 4.15, but further investigation would be required to confirm this.

Besides these difficulties in assessing the damage sustained by the window due to MP, there were other simplifications that were made in the simulations that could be sources of inaccuracies. The limitation of available secondary emission data for the window material was discussed in detail, and this could lead to significant deviations in MP behavior from what was predicted. The analysis in the previous chapter showed that within materials with similar properties to the Rexolite® window currently used, the accuracy of results is limited. In addition to limited material data, the roughness of the surface and machining of the window can also affect the emission properties [7] [50], further obfuscating the secondary emission properties used to calculate MP.

Another simplification used in the simulations was the window geometry itself. The current geometry has a notch in the vacuum side near the inner conductor, as shown in Fig 2.1, and this could affect how electrons interact with the window. The necessity of this notch was discussed in the analysis of EM fields of the isolated coupler, and the current design with the notch has only slightly lower fields than the design with no notch, so if new MP modes are introduced by the notch such that MP is increased for typical accelerator operation, then the notch should be removed.

Overall there are many conditions in the current design of the RF window and DTL system as a whole that can lead to failure. The EM stresses have not been minimized, and this is essential to ensure that any anomalous conditions will not produce failures. Moving the window farther away from the cavity could prevent some issues in anomalous higher order modes propagating from the cavity, as well as reducing potential initiation events for MP. MP will always be an issue as well, and so minimizing the potential for growth in electron population is necessary. These issues are present in all accelerator systems, so those design issues discussed such as window geometry and placement, RF signal design, and window materials should be considered in the design of any vacuum RF system.

References

- [1] B. Rusnak, *RF Power and HOM Coupler Tutorial*, United States, 2003.
- [2] I. E. Campisi, "State of the art power couplers for superconducting RF cavities," in *Proceedings of EPAC 2002*, Paris, France, 2002.
- [3] M. S. Champion, "RF input couplers and windows: performances, limitations, and recent developments," in *Proceedings of the 1995 Workshop on RF superconductivity*, Gif-sur-Yvette, France, 1995.
- [4] K. A. Cummings and S. H. Risbud, "Dielectric materials for window applications," *Journal of Physics and Chemistry of Solids*, vol. 61, no. 4, pp. 551-560, 2000.
- [5] K. A. Cummings, S. H. Risbud, D. W. Metzger and N. K. Bultman, "Experimental and Analytical Study of heating in rf accelerator Windows," *Journal of Microwave Power and Electromagnetic Energy*, vol. 32, no. 2, pp. 101-108, 1997.
- [6] D. Tommasini, "Dielectric insulation and high-voltage issues," *arXiv preprint arXiv:1104.0802*, pp. 335-355, 2011.
- [7] C. Chang, G. Liu, C. Tang, C. Chen and J. Fang, "Review of recent theories and experiments for improving high-power microwave window breakdown thresholds," *Physics of Plasmas*, vol. 18, no. 5, pp. 055702-1--055702-12, 2011.
- [8] A. Neuber, J. Dickens, D. Hemmert, H. Krompholz, L. L. Hatfield and M. Kristiansen, "Window Breakdown Caused by High-Power Microwaves," *IEEE Transactions on Plasma Science*, vol. 26, no. 3, pp. 296-303, 1998.
- [9] D. Rathi, K. Mishra, S. Goerge, A. Varia, S. V. Kulkarni and I. Team, "A Simple Coaxial Ceramic Based Vacuum Window for Vacuum Transmission Line of ICRF System," in *AIP Conference Proceedings*, 2011.
- [10] S. Chel, M. Desmons, C. Travier, T. Garvey, P. Lepercq and R. Panvier, "Coaxial Disc Windows for a high power superconducting cavity input coupler," in *Proceedings of the 1999 Particle Accelerator Conference*, New York, New York, USA, 1999.
- [11] "Los Alamos Neutron Science Center About Page, History," [Online]. Available: <https://lansce.lanl.gov/about/history.php>.
- [12] P. W. Lisowski and Schoenberg, "The Los Alamos Neutron Science Center," *Nuclear Instruments and Methods in Physics Research A*, vol. 562, no. 2, pp. 910-914, 2006.
- [13] G. Devanz, "Multipactor simulations in superconducting cavities and power couplers," *Physical Review Special Topics-Accelerators and Beams*, vol. 4, pp. 1-5, 2001.

- [14] "Rexolite by C-Lec Plastics," [Online]. Available: <http://www.rexolite.com/specifications/>.
- [15] H. Kim, J. Verboncoeur and Y. Lau, "Modeling RF Window Breakdown: from Vacuum Multipactor to RF Plasma," *IEEE Transactions on Dielectrics and Electrical Insulation*, vol. 14, no. 4, pp. 766-773, August 2007.
- [16] T. P. Wangler, *RF Linear Accelerators*, Wiley-VCH, 2008.
- [17] J. J. Song, "Multipacting study of the RF window at the advanced photon source," in *Proceedings of the 1999 Particle Accelerator Conference*, New York, New York, USA, 1999.
- [18] Dassault Systèmes, "CST Studio Suite".
- [19] S. Kurennoy, "Electromagnetic Modeling of RF Drive in the LANSCE DTL," in *Proceedings of the IPAC 2013*, Shanghai, China, 2013.
- [20] J. Shi, H. Chen, S. Zheng, D. Li, R. Rimmer and H. Wang, "Comparison of Measured and Calculated Coupling between a waveguide and an RF cavity using CST Microwave Studio," in *Proceedings of EPAC 2006*, Edinburgh, Scotland, 2006.
- [21] D. M. Pozar, *Microwave Engineering*, John Wiley & Sons, 2009.
- [22] P. Lapostolle and M. Weiss, "Formulae and procedures useful for the design of linear accelerators," Geneva, Switzerland, 2000.
- [23] H. Barkuijsen, R. de Beer, W. M. M. J. Bovée and D. van Ormondt, "Retrieval of Frequencies, Amplitudes, Damping Factors, and Phases from Time-Domain Signals Using a Linear Least-Squares Procedure," *Journal of Magnetic Resonance*, vol. 61, no. 3, pp. 465-481, 1985.
- [24] T. Rylander, P. Ingleström and A. Bondeson, *Computational Electromagnetics*, Springer Science and Business Media, 2012.
- [25] S. Kurennoy, "RF fields in LANSCE DTL tanks," LANL report AOT-HPE 15-005, Los Alamos, New Mexico, USA, 2014.
- [26] Q. H. Liu, "The PSTD Algorithm: A Time-Domain Method Requiring Only Two Cells per Wavelength," *Microwave and Optical Technology Letters*, vol. 15, no. 3, pp. 158-165, 1997.
- [27] M. B. Allen III and E. L. Isaacson, "Numerical analysis for applied science," John Wiley & Sons, 2011.
- [28] R. F. Parodi, "Multipacting," *arXiv preprint arXiv: 1112.2176*, 2011.
- [29] M. Ludovico, G. Zarba, L. Accatino and D. Raboso, "Multipaction analysis and power handling evaluation in waveguide components for satellite antenna applications," in *IEEE Antennas and Propagation Society International Symposium*, Boston, Massachusetts, USA, 2001.

- [30] S. K. Nagesh, D. Revannasiddiah and S. V. K. Shastry, "Investigation of multipactor breakdown in communication satellite microwave co-axial systems," *Pramana*, vol. 64, no. 1, pp. 95-110, 2005.
- [31] F. Krawczyk, "Status of multipacting simulation capabilities for SCRF applications," in *The 10yd Workshop on RF Superconductivity*, Tsukuba, Japan, 2001.
- [32] R. Kishek and Y. Lau, "Multipactor Discharge on a Dielectric," *Physical Review Letters*, vol. 80, no. 1, pp. 193-196, 1998.
- [33] R. Kishek, Y. Lau, L. Ang, A. Valfells and R. Gilgenbach, "Multipactor Discharge on Metals and Dielectrics: Historical review and recent theories," *Physics of Plasmas*, vol. 5, no. 5, pp. 2120-2126, 1998.
- [34] E. Chojnacki, "Simulations of a multipactor-inhibited waveguide geometry," *Physical Review Topics-Accelerators and Beams*, vol. 3, pp. 1-5, 2000.
- [35] E. Sorolla, S. Anza, B. Gimeno, A. M. Pérez, C. Vicente, J. Gil, F. J. Pérez-Soler, F. D. Quesada, A. Álvarez and V. E. Boria, "An Analytical model to evaluate the radiated power spectrum of a multipactor discharge in a parallel-plate region," *IEEE Transactions on Electron Devices*, vol. 55, no. 8, pp. 2252-2258, 2008.
- [36] P. Ylä-Oujala, "Analysis of Electron Multipacting in Coaxial Lines with Traveling and Mixed Waves," in *Dt. Elektronen-Synchrotron DESY, MHF-SL Group*, 1997.
- [37] N. Rozario, H. F. Lenzing, K. F. Reardon, M. S. Zarro and C. G. Baran, "Investigation of Telstar 4 Spacecraft Ku-Band and C-Band Antenna Components for Multipactor Breakdown," *IEEE Transactions on Microwave Theory and Techniques*, vol. 42, no. 4, pp. 558-564, 1994.
- [38] R. Udiljak, D. Anderson, M. Lisak, V. E. Semenov and J. Puech, "Multipactor in a coaxial transmission line. I. Analytical study," *Physics of Plasmas*, pp. 1-11, 2007.
- [39] M. Mostajeran, "Can accurate investigation of phase stability explain the experimental results of multipactor phenomenon?," *Journal of Instrumentation*, vol. 8, no. 4, p. P04027, 2013.
- [40] E. A. Burke, "Secondary Emission from polymers," *IEEE Transactions on Nuclear Science*, Vols. NS-27, no. 6, pp. 1760-1764, 1980.
- [41] J. Cazaux, "Calculated influence of work function on SE escape probability and Secondary electron emission yield," *Applied Surface Science*, vol. 257, no. 3, pp. 1002-1009, 2010.
- [42] J. P. Ganachaud and A. Mokrani, "Theoretical study of the secondary electron emission of insulating targets," *Surface Science*, vol. 334, no. 1-3, pp. 329-341, 1995.
- [43] A. Shih and C. Hor, "Secondary Emission Properties as a Function of the Electron Incidence Angle," *IEEE Transactions on Electron Devices*, vol. 40, no. 4, pp. 824-829, 1993.

- [44] J. R. M. Vaughan, "A New Formula for Secondary Emission Yield," *IEEE Transactions on Electron Devices*, vol. 36, no. 9, pp. 1963-1967, 1989.
- [45] M. Furman and M. Pivi, "Probabilistic model for the simulation of secondary electron emission," *Physical Review Special Topics-Accelerators and Beams*, vol. 5, no. 12, pp. 1-18, 2002.
- [46] S. A. Rice and J. P. Verboncoeur, "A comparison of multipactor predictions using two popular secondary electron models," *IEEE Transactions on Plasma Science*, vol. 42, no. 6, pp. 1484-1487, 2014.
- [47] R. A. Kishek, "Ping-pong modes: A New form of multipactor," *Physical Review Letters*, vol. 108, no. 3, p. 035003, 2012.
- [48] I. A. Kossyi, G. S. Lukyanchikov, V. E. Semenov, E. I. Rakova, D. Anderson, M. Lisak and J. Puech, "Polyphase (non-resonant) multipactor in rectangular waveguides," *Journal of Physics D: Applied Physics*, vol. 41, no. 6, p. 065203, 2008.
- [49] V. Semenov, V. Nechaev, E. Rakova, N. Zharova, D. Anderson, M. Lisak and J. Puech, "Multiphase regimes of single-surface multipactor," *Physics of Plasmas*, vol. 12, pp. 1-6, 2005.
- [50] L.-K. Ang, Y. Y. Lau, R. A. Kishek and R. M. Gilgenbach, "Power deposited on a dielectric by multipactor," *IEEE Transactions on Plasma Science*, vol. 26, no. 3, pp. 290-295, 1998.
- [51] O. A. Ivanov, M. A. Lobaev, V. A. Isaev and A. L. Vikharev, "Suppressing and initiation of multipactor discharge on a dielectric by an external dc bias," *Physical Review Special Topics--Accelerators and beams*, vol. 13, no. 2, p. 022004, 2010.
- [52] W. Kaabi, H. Jenhani, A. Variola, G. Keppel and V. Palmieri, "Titanium Nitride Coating as a Multipactor Suppressor on RF coupler ceramic windows," in *Proceedings of PAC09*, Vancouver, British Colombia, Canada, 2009.
- [53] H. C. Kim and J. P. Verboncoeur, "Time-dependent physics of a single-surface multipactor discharge," *Physics of Plasmas*, vol. 12, no. 12, p. 123504, 2005.
- [54] A. Sazontov and V. Nevchaev, "Effects of rf magnetic field and wave reflection on multipactor discharge on a dielectric," *Physics of Plasmas*, vol. 17, pp. 1-10, 2010.
- [55] F. Zhu, S. Zhang, J. Luo and S. Dai, "Multipactor on a Dielectric Surface with Longitudinal RF Electric Field Action," *Progress in Electromagnetics Research*, vol. 24, pp. 177-185, 2011.
- [56] E. Somersalo, P. Yli-Oujala, D. Proch and J. Sarvas, "Computational Methods for Analyzing Electron Multipacting in RF Structures," *Particle Accelerators*, vol. 59, pp. 107-141, January 1998.
- [57] A. M. Perez, C. Tienda, C. Vicente, S. Anza, J. Gil, B. Gimeno, V. E. Boria and D. Raboso, "Prediction of Multipactor Breakdown Thresholds in Coaxial Transmission Lines for Traveling, Standing and Mixed Waves," *IEEE Transactions on Plasma Science*, vol. 37, no. 10, pp. 2031-2040, 2009.

- [58] A. V. Gaponov and M. A. Miller, "POTENTIAL WELLS FOR CHARGED PARTICLES IN A HIGH-FREQUENCY ELECTRO-MAGNETIC FIELD," *Journal of Experimental and Theoretical Physics*, vol. 34, pp. 242-243, 1958.
- [59] K. F. Riley, M. P. Hobson and S. J. Bence, *Mathematical Methods for Physics and Engineering*, Cambridge University Press, 2006.
- [60] V. E. Semenov, N. Zharova, R. Udiljak, D. Anderson, M. Lisak and J. Puech, "Multipactor in a coaxial transmission line II: Particle-in-cell simulations," *Physics of plasmas*, vol. 14, no. 3, p. 033509, 2007.
- [61] A. Valfells, L. Ang, Y. Lau and R. Gilgenbach, "Effects of an external magnetic field, and of oblique radio-frequency electric fields on multipactor discharge on a dielectric," *Physics of Plasmas*, vol. 7, no. 2, pp. 750-757, 2000.
- [62] J. W. You, H. G. Wang, J. F. Zhang, Y. Li, W. Z. Cui and T. J. Cui, "Highly Efficient and Adaptive Numerical Scheme to Analyze Multipactor in Waveguide Devices," *IEEE Transactions on Electron Devices*, vol. 62, no. 4, pp. 1327-1333, 2015.
- [63] P. Zhang, Y. Y. Lau, M. Franzi and R. M. Gilgenbach, "Multipactor susceptibility on a dielectric with a bias dc electric field and a background gas," *Physics of Plasma*, vol. 18, no. 5, p. 053508, 2011.
- [64] G. Burt, R. G. Carter, A. C. Dexter, B. Hall, J. D. A. Smith and P. Goudket, "Benchmarking simulations of multipactor in rectangular waveguides using CST-Particle Studio," in *Proceedings of SRF2009*, Berlin, Germany, 2009.
- [65] L. Ge, C. Adolphsen, L. K. Ko, Z. Li, C. Ng, G. Schussman, F. Wang and B. Rusnak, "Multipacting Simulations of the TTF-III Power Coupler Components," in *Proceedings of the PAC07*, Albuquerque, New Mexico, USA, 2007.
- [66] I. A. Kossyi, G. S. Luk'yanchikov, V. E. Semenov, N. A. Zharova, D. Anderson, M. Lisak and J. Puech, "Experimental and numerical investigation of multipactor discharges in a coaxial waveguide," *Journal of Physics D: Applied Physics*, vol. 43, p. 345206, 2010.
- [67] S. Riyopoulos, D. Chernin and D. Dialetis, "Effect of Random Secondary Delay Times and Emission Velocities in Electron Multipactors," *IEEE Transactions on Electron Devices*, vol. 44, no. 3, pp. 489-497, 1997.
- [68] F. Hamme, U. Becker and P. Hammes, "Simulation of Secondary Electron Emission with CST Particle Studio," in *Proceedings of ICAP*, Chamonix, France, 2006.
- [69] G. Romanov, "Update on multipactor in coaxial waveguides using CST Particle Studio," in *Proceedings of 2011 Particle Accelerator Conference*, New York, New York, USA, 2011.
- [70] L. V. Kravchuk, G. V. Romanov and S. G. Tarasov, "Multipactoring code for 3D accelerating structures," *arXiv preprint physics/0008015*, 2000.

- [71] J. Cazaux, "A new model of dependence of secondary electron emission yield on primary electron energy for application to polymers," *Journal of Physics D: Applied Physics*, vol. 38, no. 14, pp. 2433-2441, 2005.
- [72] J. Cazaux, "Some considerations on the secondary electron emission from e- irradiated insulators," *Journal of Applied Physics*, vol. 85, no. 1137-1147, p. 1137, 1999.
- [73] G. Holmén, B. Svensson and A. Burén, "Ion induced electron emission from polycrystalline copper," *Nuclear Instruments and Methods*, vol. 185, no. 1-3, pp. 523-532, 1981.
- [74] K. Ohya, K. Inai, H. Kuwada, T. Hayashi and M. Saito, "Dynamic simulation of secondary electron emission and charging up of an insulating material," *Surface and Coatings Technology*, vol. 202, no. 22-23, pp. 5310-5313, 2008.
- [75] R. Renoud, F. Mady, C. Attard, J. Bigarré and J. P. Ganachaud, "Secondary electron emission of an insulating target induced by a well-focused electron beam--Monte Carlo Simulation study," *Physica Status Solidi*, vol. 201, no. 9, pp. 2119-2133, 2004.
- [76] A. M. Botelho do Rego, M. Rei Vilar, J. Lopes da Silva, M. Heyman and M. Schott, "Electronic excitation and secondary electron emission studies by low-energy electrons backscattered from thin polystyrene film surfaces," *Surface Science*, vol. 178, no. 1-3, pp. 367-374, 1986.
- [77] V. Baglin, J. Bojko, O. Gröbner, B. Henrist, N. Hilleret, C. Scheuerlein and M. Taborrelli, "The Secondary Electron Yield of Technical Materials and its Variation with Surface Treatments," in *Seventh European Particle Accelerator Conference*, Vienna, Austria, 2000.
- [78] Y.-S. Liu, G.-J. Zhang, W.-B. Zhao and Z. Yan, "Analysis on surface charging of insulator prior to flashover in vacuum," *Applied Surface Science*, vol. 230, no. 1-4, pp. 12-17, 2004.
- [79] Suharyanto, Y. Yamano, S. Kobayashi, S. Michizono and Y. Saito, "Secondary Electron Emission and Surface Charging Evaluation of alumina ceramics and sapphire," *IEEE Transactions on Dielectrics and Electrical Insulation*, vol. 13, no. 1, pp. 72-78, 2006.
- [80] C. Chang, G. Z. Liu, C. X. Tang and L. X. Yan, "The influence of space charge shielding on dielectric multipactor," *Physics of Plasmas*, vol. 16, no. 5, p. 053506, 2009.
- [81] Y. Li, X. Wang and W. Cui, "Space Charge Effects on Multipactor Discharge of Microwave Components," in *2011 4th IEEE International Symposium on Microwave, Antenna, Propagation and EMC Technologies for Wireless Communications*, Beijing, China, 2011.
- [82] S. Riyopoulos, "Multipactor saturation due to space-charge-induced debunching," *Physics of Plasmas*, vol. 4, no. 5, pp. 1448-1462, 1997.
- [83] E. Sorolla, A. Sounas and M. Mattes, "Space charge effects for multipactor in coaxial lines," *Physics of Plasmas*, vol. 22, no. 3, p. 033512, 2015.
- [84] A. Valfells, J. P. Verboncoeur and Y. Y. Lau, "Space-charge effects on multipactor on a dielectric," *IEEE Transactions on Plasma Science*, vol. 28, no. 3, pp. 529-536, 2000.